



VCU

Virginia Commonwealth University
VCU Scholars Compass

Theses and Dissertations

Graduate School

2013

Hybrid PET/MRI Nanoparticle Development and Multi-Modal Imaging

David Hoffman
Virginia Commonwealth University

Follow this and additional works at: <https://scholarscompass.vcu.edu/etd>



Part of the [Health and Medical Physics Commons](#)

© The Author

Downloaded from

<https://scholarscompass.vcu.edu/etd/3253>

This Dissertation is brought to you for free and open access by the Graduate School at VCU Scholars Compass. It has been accepted for inclusion in Theses and Dissertations by an authorized administrator of VCU Scholars Compass. For more information, please contact libcompass@vcu.edu.

HYBRID PET/MRI NANOPARTICLE PROBE DEVELOPMENT AND MULTI-MODAL IMAGING

A dissertation submitted in partial fulfillment of the requirements for the degree of Doctor of Philosophy in Medical Physics at Virginia Commonwealth University.

by
David Blair Hoffman
Bachelor of Science in Interdisciplinary Physics and German
University of Richmond, Richmond, Virginia, 2008

Director: Jamal Zweit PhD, DSc
Professor, Department of Radiology

Virginia Commonwealth University
School of Medicine
Richmond, Virginia
December 3rd, 2013

Abstract

HYBRID PET/MRI NANOPARTICLE PROBE DEVELOPMENT AND MULTI-MODAL IMAGING

By David Blair Hoffman, BS

A dissertation submitted in partial fulfillment of the requirements for the degree of Doctor of Philosophy in Medical Physics at Virginia Commonwealth University.

Virginia Commonwealth University, 2013

Director: Jamal Zweit PhD, DSc

Professor, Department of Radiology

The development of hybrid PET/MRI imaging systems needs to be paralleled with the development of a hybrid intrinsic PET/MRI probes. The aim of this work was to develop and validate a novel radio-superparamagnetic nanoparticle (r-SPNP) for hybrid PET/MRI imaging. This was achieved with the synthesis of superparamagnetic iron oxide nanoparticles (SPIONs) that intrinsically incorporated ^{59}Fe and manganese iron oxide nanoparticles (MIONs) that intrinsically incorporated ^{52}Mn . Both [^{59}Fe]-SPIONs and [^{52}Mn]-MIONs were produced through thermal decomposition synthesis. The physiochemical characteristics of the r-SPNPs were assessed with TEM, DLS, and zeta-potential measurements, as well as in imaging phantom studies. The [^{59}Fe]-SPIONs were evaluated *in vivo* with biodistribution and MR imaging studies. The biodistribution studies of [^{59}Fe]-SPIONs showed uptake in the liver. This corresponded with major MR signal contrast measured in the liver. ^{52}Mn was produced on natural chromium through the $^{52}\text{Cr}(p,n)^{52}\text{Mn}$ reaction. The manganese radionuclides were separated from the target material through a liquid-liquid extraction. The $\alpha_v\beta_3$ integrin binding of [^{52}Mn]-MION-cRGDs was evaluated with $\alpha_v\beta_3$ integrin solid phase assays, and the expression of $\alpha_v\beta_3$ integrin in U87MG xenograft tumors was characterized with fluorescence flow cytometry. [^{52}Mn]-MION-

cRGDs were used for *in vivo* PET and MR imaging of U87MG xenograft tumor bearing mice. PET data showed increased [^{52}Mn]-MION-cRGD uptake compared with untargeted [^{52}Mn]-MIONs. ROI analysis of PET and MRI data showed that MR contrasted corresponded with PET signal. Future work will utilize [^{52}Mn]-MION-cRGDs in other tumor models and with hybrid PET/MRI imaging systems.

Acknowledgement

The first acknowledgement is traditionally, and in this case correctly, made to one's mentor. Jamal Zweit has been a tremendous supervisor for me these past four year and I am grateful for his guidance and criticism. Dr. Zweit has given me opportunities to develop as a scholar that surpass the norm and even my own expectations. I am truly thankful to have Dr. Zweit as my mentor.

My colleagues at the CMI have made my graduate education possible. Sundaresan Gobalakrishnan instructed me in countless experiments and helped me develop nearly every protocol in this work. He has taught me so much ranging from molecular imaging to tail-vein injections. To this day, the voice in my head that lists off the tissues collected during dissection has a mild Indian accent. Minghao Sun has taught me the majority of the chemistry that I currently understand. His assistance with this work cannot be understated. Thank you for the work, teaching, and productive discussions from the last years. I only hope that I was able to help him one twentieth as much as he has helped me. Likun Yang also contributed greatly to this project. Thank you for all of your insight into nano-chemistry and physiochemical characterization. Sorry about always making Minghao late for lunch. I just really wanted to hear his perspective on the Korean War, or make one last point about European history. Purnima Jose has had the un-enviable task of instructing me on numerous molecular biology methods. I am greatly appreciative of her work, spirit, and aid during this project. Li Wang and Rennie Berry have helped and trained me for this entire process. Any ability I have in cell culture should be attributed to their instruction. I am thankful for assistance from Celina Thadigiri and Gajanan Dewkar, especially Dr. Dewkar's insight developing the radio-chemical extraction method. To everyone in medical physics and the CMI, you have made my graduate education rich.

Another acknowledgement must be made to my classmates in here at VCU. Narottam Lamichhane helped with many aspects of this work and has been a personal Sherpa and companion on the entire journey. Chris Bass has been invaluable in developing many of the computational methods used to analysis the data collected, and as a constant reminder that complaining can make you feel better. Philip McDonagh assisted in much of the data collection and was always great to pass the long experimental hours. Rabten Datsang, Scott Robertson, and many other classmates contributed to my graduate education as a whole. Thanks, guys.

And an additional thank you to the others that assisted this project. Frank Corwin and Gang Zhu instructed me in MRI and helped develop the imaging sequence used in this project. Bob Ylimaki supported with the ^{52}Mn production and cyclotron irradiation.

Finally, I would like to show my appreciation to my friends and family in Virginia, California, and elsewhere. Mom, you inspire me to be a scientist. Dad, you inspire me to be intellectual and moral. To my friends, you inspire me to love and honor me with your friendships.

I dedicate my dissertation to Warren Dexter.

Vita

David Blair Hoffman was born on May 14th, 1986, in Berkeley, California, and is an American citizen. He graduated from Campolindo High School, Moraga, California in 2004. He received his Bachelor of Science in Interdisciplinary Physics from University of Richmond, Richmond, Virginia in 2008. He subsequently worked as an acoustical consultant in Sacramento, California. In August, 2009, he entered graduate school at Virginia Commonwealth University.

Table of Contents

Abstract.....	iii
Acknowledgement	v
Vita.....	vi
Table of Contents.....	vii
List of Tables	x
List of Figures.....	xi
List of Abbreviations	xx
Chapter 1.....	1
1. Introduction.....	1
1.1. Objectives.....	1
1.2. Strategy.....	2
1.2.1. Extrinsically vs. Intrinsically Radio-labeled Nanoparticles.....	2
1.2.2. Radio-intrinsic Superparamagnetic Nanoparticle.....	3
Chapter 2.....	5
2. Background.....	5
2.1. Medical Imaging of Cancer.....	5
2.2. Molecular Imaging of Cancer	6
2.3. Positron Emission Tomography.....	8
2.3.1. Decay, Annihilation, and Coincidence Detection.....	10
2.3.2. PET Radionuclides.....	12
2.4. Magnetic Resonance Imaging	14
2.4.1. Relaxation Parameters	17
2.4.2. Contrast Agents.....	17
2.5. Hybrid Imaging	18
2.5.1. PET/CT.....	19
2.5.2. PET/MRI.....	19
2.6. Superparamagnetic Iron Oxides.....	20
2.6.1. Applications	21
2.6.2. Mono-Crystalline Superparamagnetic Nanoparticles	22
2.6.3. Synthetic Strategies.....	23
Chapter 3.....	26
3. Hybrid PET/MR Nanoparticle Synthesis.....	26
3.1. [⁵⁹ Fe]-SPION Synthesis	26
3.1.1. Natural iron-oxide nanoparticle synthesis	26
3.1.2. ⁵⁹ Fe incorporation	27
3.2. [⁵² Mn]-MION synthesis	28
3.2.1. Natural Manganese Iron Oxide Nanoparticle Synthesis.....	29
3.2.2. Core/shell synthesis of MIONs.....	29
3.2.3. ⁵² Mn cyclotron production.....	30
3.2.4. ⁵² Mn radiochemical extraction.....	33
3.2.5. ⁵² Mn incorporation.....	36
3.3. Modification of Nanoparticles with Polymer Coating	37

3.3.1.	Ligand exchange reaction	39
3.3.2.	Alternative coating strategy	39
3.3.3.	Synthesis of coating ligand for bio-conjugation	40
3.3.4.	Bio-conjugation reaction.....	41
3.4.	SPION physical and magnetic characterization	43
3.4.1.	Transmission electron microscopy	43
3.4.2.	Hydrodynamic size and zeta potential measurement.....	43
3.4.3.	Iron and manganese concentration measurement	44
3.4.4.	Relaxometry.....	44
3.4.5.	Gamma emission characterization and quantification	47
3.5.	Nano-particle characterizations.....	48
3.5.1.	Natural SPION.....	49
3.5.2.	⁵⁹ Fe SPION	51
3.5.3.	Natural MION.....	53
3.5.4.	MION core/shell	56
3.5.5.	[⁵² Mn]-MION.....	59
Chapter 4.....		64
4.	[⁵⁹ Fe]-SPION Evaluation	64
4.1.	[⁵⁹ Fe]-SPION Biodistribution	64
4.2.	MR imaging of ⁵⁹ Fe-SPION.....	65
4.3.	Signal contrast mapping	67
4.4.	[⁵⁹ Fe]-SPION in vivo evaluation results	68
4.4.1.	Biodistribution	68
4.4.2.	MR imaging	70
4.4.3.	Signal contrast mapping.....	78
Chapter 5.....		80
5.	[⁵² Mn]-MION-cRGD Evaluation.....	80
5.1.	PET characterization of imaging radionuclides	80
5.1.1.	Spatial Resolution	81
5.1.2.	Sensitivity Measurement.....	82
5.1.3.	Count Rate Linearity.....	84
5.1.4.	¹⁸ F Characterization	85
5.1.5.	⁸⁹ Zr Characterization.....	86
5.1.6.	⁵² Mn Characterization.....	88
5.2.	Hybrid PET/MR Imaging of U87-MG Tumor Bearing Mice	89
5.2.1.	Hybrid PET/MRI phantom study.....	89
5.2.2.	U87MG tumor model.....	91
5.2.3.	Assessment of $\alpha_v\beta_3$ Integrin Binding.....	95
5.2.4.	PET Results.....	98
5.2.5.	MRI Results	107
5.2.6.	Co-registered Hybrid PET/MRI Results	113
Chapter 6.....		116
6.	Summary and Conclusion.....	116
6.1.	Radio-intrinsic superparamagnetic nanoparticles	117
6.2.	Hybrid PET/MRI.....	117
Chapter 7.....		118

7. Further Work.....	118
7.1. Future direction for ^{52}Mn	118
7.2. Future direction for $[^{52}\text{Mn}]$ -MION.....	119
Appendix.....	120
Research publications from this work	120
Conferences and Presentations	121
References.....	121

List of Tables

Table 1: Characteristics of medical imaging modalities that have molecularly targeted imaging agents or non-targeted agents.....	6
Table 2: PET tracers used for the imaging of disease.....	9
Table 3: The characteristics of organic PET radionuclides.	13
Table 4: The characteristics of various inorganic generator produced PET radionuclides.	13
Table 5: The characteristics of various inorganic cyclotron produced PET radionuclides.	14
Table 6: Nanoparticle characteristics of different synthetic routs.	48
Table 7: Relaxometry results of a single MION sample over one month. Nanoparticles where coated with molecular weight 2000 PEG.....	49
Table 8: Biodistribution of intravenously injected ^{59}Fe -SPIONs in nude mice (n=3 per time point). Data are presented as %ID/g (mean \pm stdv) values determined through gamma counting. Nude mice (n=3 per time point) were injected through the tail vein with ^{59}Fe -SPIONs (0.84 \pm 0.03 μCi ; 200 μL ; 26 \pm 1 μg of Fe). Tissues were collected, weighted, and the gamma emission was measured to calculate the %ID/g.	68
Table 9: Biodistribution of tail-vein injected $^{59}\text{FeCl}_3$ (0.23 \pm .3 μCi) in nude mice (n=3 per time point). Data are presented as %ID/g (mean \pm stdv) values determined through gamma counting. Tissues were collected, weighted, and the gamma emission was measured to calculate the %ID/g.	69
Table 10: The full width at half maximum of the reconstructed ^{18}F spatial resolution phantom image at different offsets from the PET scanner isocenter.	85
Table 11: The full width at half maximum of the reconstructed ^{89}Zr spatial resolution phantom image at different offsets from the PET scanner isocenter.	87
Table 12: The full width at half maximum of the reconstructed ^{52}Mn spatial resolution phantom image at different offsets from the PET scanner isocenter.	88
Table 13: The %ID/g values of various tissues as measured with ROI analysis of PET data for ^{52}Mn -MION injected tumor bearing mice.	103

List of Figures

- Figure 1: The radioactive chelator model (A) externally labels the nanoparticle, while the radio-intrinsic model (B) internally incorporates the radioactivity. 3
- Figure 2: A positron emitting radionuclide decays and yields a positron that travels a distance through tissue and annihilates with an electron. This emits two 511 keV photons that exit the body and are detected by the array of scintillation crystal for image reconstruction. 11
- Figure 3: A) True coincidence detection occurs when the two gamma rays from an annihilation event exit the body and are detected by the scintillation crystals within the energy and time windows allowed for coincidence. B) If one or both of the photons are scattered, but are still detected within the time and energy windows, then a scattered coincidence has occurred. C) When two photons from different annihilation events are detected, a random coincidence has occurred. 12
- Figure 4: The precession, excitation, and relaxation of spins in MRI. The “laboratory frame” is the static reference frame of the MRI scanner with the z-axis oriented along the bore of the main magnetic. The rotation frame precesses about the z-axis of the laboratory frame at the Larmor frequency. A) The atoms of the imaged tissue precess around the magnetic field at the Larmor frequency. B) An excitation pulse of RF excites a slice of the tissue into the transverse plane. The net magnetization relaxes growing in the longitudinal direction, described by the parameter T1, and decaying away from the transverse plane as described by the parameter T2. 16
- Figure 5: Chemical precipitation synthesis of SPIOs. A) Ferrous and ferric salts are dissolved aqiously in the presence of carbohydrates, such as dextran. B) Iron oxide crystals form during nucleation. C) The iron oxide crystals aggregate and are coated by the carbohydrates to form SPIOs. 24
- Figure 6: As the proton beam transverses the chromium target, it loses energy based on the stopping power of the chromium. This figure depicts the kinetic energy remaining in a 12.9 MeV proton beam as it travels through chromium. 31
- Figure 7: The target assembly used to support the chromium in the cyclotron beam. The chromium foil target (center) is held to the iridium holder (outside) by a steel clip (middle) during the irradiation..... 32
- Figure 8: The gamma energy spectrum of a natural chromium foil after 12.9 MeV proton irradiation. The principle emissions of ^{52}Mn and ^{54}Mn are labeled. Additionally, the 511 keV peak associated with β^+ annihilation photons is labeled. Also visible is the 346 keV peak of ^{52}Mn 33
- Figure 9: Radiochemical extraction of ^{52}Mn . A) The chromium foil (gray) is loaded into an iridium holder (black) and irradiated with 12.9 MeV protons (red). B) ^{52}Mn atoms (pink) are produced throughout the foil, which is unloaded from the holder. C) The foil is then dissolved in 12 N hydrochloric acid and hydrogen peroxide while heating. The chromium

(green) and manganese (pink) are dispersed throughout the solution. D) The aqueous solution is mixed with the organic phase (yellow), trioctylamine diluted in n-hexane. The aqueous phase then separates from the organic phase, with the majority of the manganese in the organic phase and the chromium in the aqueous phase. E) The organic phase (yellow) is collected for re-extraction of the ^{52}Mn from the organic phase. F) The aqueous phase (green) still contains a portion of the ^{52}Mn (pink) and can be further extracted. 34

Figure 10: Re-extraction of ^{52}Mn from the organic phase produced from the extraction of manganese isotopes from the chromium isotopes. A) ^{52}Mn (pink) is dissolved in trioctylamine diluted in n-hexane (yellow) as a result of the initial extraction. B) Ammonium hydroxide aqueous solution (blue) is added to the organic phase and vortexed. The ^{52}Mn (pink) transfers to the aqueous phase. C) The aqueous phase (blue) containing the ^{52}Mn (pink) is collected for future utilization in MION synthesis. D) The aqueous phase is further re-extracted to collect any remaining ^{52}Mn 35

Figure 11: The gamma energy spectrum of the separated manganese radionuclides is similar to that of the irradiated foil. That is because the only major contributor to the spectrum aside from ^{52}Mn is ^{54}Mn , which cannot be chemically separated from the other manganese radionuclides. 36

Figure 12: Incorporation of ^{52}Mn into the MION. A) $^{52}\text{Mn}^{2+}$, natural Mn^{2+} , and $\text{Fe}^{3+/2+}$, are combined and heated to 200°C with oleic acid and oleylamine. B) Manganese iron oxide nanoparticle seeds form. C) The seeds grow into larger crystals incorporating ^{52}Mn throughout and coated with oleic acid and oleylamine..... 37

Figure 13: Multidentate poly-ethylene-glycol ligand for coating the SPIONs. It is composed of dopamine on the bottom left, which non-covalently binds to the surface of the SPION, a repeating poly-acrylic acid (PAA-1800 MW) chain on the top, which is the back bone of the molecule, and a repeating poly-ethylene glycol (PEG-2000 MW) that provides biocompatibility and water solubility. 38

Figure 14: Synthetic scheme to produce $\text{CH}_3\text{O-PEG}_{2000\text{MW}}\text{-NH}_2$. This ligand is then used to coat the nanoparticle. 40

Figure 15: Alternative coating strategy schematic. The oleylamine and oleic acid is first replaced with NDA on the surface of the nanoparticles. Then, the $\text{CH}_3\text{O-PEG}_{2000\text{MW}}\text{-NH}_2$ is added to react with the NDA and PEGylate the nanoparticles..... 40

Figure 16 Multidentateamino-PEG ligand for coating the SPIONs and bio-conjugation. It is composed of dopamine on the bottom left, which non-covalently binds to the surface of the SPION, a repeating poly-acrylic acid (PAA-1800 MW) chain on the top, which is the back bone of the molecule, and repeating poly-ethylene glycol (PEG-2000 MW), half of which include a terminal amine group for bio-conjugation reactions. 41

Figure 17 A) Schematic of the nanoparticle targeting with RGD peptide. B) The first strategy developed using the Bis(sulfosuccinimidyl) cross-linker. C) The second strategy developed using the sulfo-SMCC cross-linker..... 42

- Figure 18: The SPIONs are loaded into vials at known concentrations, including one control vial without any SPION added. These vials are incorporated into a phantom that is imaged and the T2 value of each vial is calculated. The decrease in T2 with respect to increasing SPION concentration yields the transverse relaxivity (R_2) of the SPION sample. 46
- Figure 19 Plotting the signal of a vial's ROI versus the echo time shows the transverse relaxation of the SPION suspension within each vial. Higher concentrations of SPION (and higher vial numbers in this example) result in greater signal loss with increasing TE..... 47
- Figure 20: Representative TEM image and histogram of natural SPIONs coated with oleic acid and oleylamine. Samples were prepared by spreading a dilute toluene solution of SPION onto carbon-coated copper grid. The size measured of each particle is characteristic of the size of the inorganic iron oxide core..... 50
- Figure 21: Hydrodynamic radius distribution of natural multidentate poly- ethylene-glycol coated SPIONs as measured through DLS. The left peak is SPION size and the right peak likely represents a small fraction of nanoparticle aggregation. 51
- Figure 22: TEM image and histogram of ^{59}Fe -SPIONs coated with oleic acid and oleylamine. Samples were prepared by spreading a dilute toluene solution of SPION onto carbon-coated copper grid. The size measured of each particle is characteristic of the size of the inorganic iron oxide core. 52
- Figure 23: Hydrodynamic radius (top) and zeta potential (bottom) of ^{59}Fe -SPION. 53
- Figure 24: TEM image and histogram of MIONs coated with oleic acid and oleylamine. Samples were prepared by spreading a dilute toluene solution of SPION onto carbon-coated copper grid. The size measured of each particle is characteristic of the size of the inorganic iron oxide core. The clumping of the nanoparticles seen in the TEM image may be a result of the evaporation pattern of the toluene solution. 55
- Figure 25: Hydrodynamic radius (top) and zeta potential (bottom) of MION. 56
- Figure 26: TEM image and histogram of MIONs with a core/shell structure coated with oleic acid and oleylamine. Samples were prepared by spreading a dilute toluene solution of SPION onto carbon-coated copper grid. The size measured of each particle is characteristic of the size of the inorganic iron oxide core..... 58
- Figure 27 Hydrodynamic radius (top) and zeta potential (bottom) of MIONs with a core/shell structure. The second smaller peak in the DLS figure is possibly caused by minor sample contamination..... 59
- Figure 28: Hydrodynamic radius (top) and zeta potential (bottom) of untargeted ^{52}Mn -MIONs. 61
- Figure 29: Hydrodynamic radius (top) and zeta potential (bottom) of ^{52}Mn -MION-cRGDs..... 62
- Figure 30: TEM image and histogram of ^{52}Mn -MIONs coated with oleic acid and oleylamine. Samples were prepared by spreading a dilute toluene solution of SPION onto carbon-coated

copper grid. The size measured of each particle is characteristic of the size of the inorganic manganese iron oxide core..... 63

Figure 31: Biodistribution (%ID/g) at various time points post intravenous administration. Nude mice (n=3 per time point) were injected through the tail vein with ⁵⁹Fe-SPIONs (0.84±0.03 µCi; 200 µL; 26±1 µg of Fe). Tissues were collected, weighted, and the gamma emission was measured to calculate the %ID/g. 69

Figure 32: Biodistribution (%ID/g) at various time points post tail-vein administration (0.23±.03 µCi; 200 µL) of ⁵⁹FeCl₃. Tissues were collected, weighted, and the gamma emission was measured to calculate the %ID/g. 70

Figure 33: Sagittal MR images of ⁵⁹Fe-SPION (26 ± 1 ug Fe and 840 ± 30 nCi) tail-vein injected nude mouse before (left) and 1 hour (right) after injection. The mouse was imaged with a Fast Imaging with Steady State Precession (FISP) sequence with a repeat time (TR) of 9.4 ms and echo time (TE) of 4.7 ms and number of scans averaged (NSA) of 4. A flip angle (FA) of 35° was used to achieve T2*/T1 weighted images. The blue arrows indicate the brain, the red arrows indicate the liver, and the yellows arrows indicate the bladder. 71

Figure 34: Sagittal MR images of ⁵⁹Fe-SPION (26 ± 1 ug Fe and 840 ± 30 nCi) tail-vein injected nude mouse before (left) and 4 hours (right) after injection. The mouse was imaged with a Fast Imaging with Steady State Precession (FISP) sequence with a repeat time (TR) of 9.4 ms and echo time (TE) of 4.7 ms and number of scans averaged (NSA) of 4. A flip angle (FA) of 35° was used to achieve T2*/T1 weighted images. The blue arrows indicate the brain, the red arrows indicate the liver, and the yellows arrows indicate the bladder. 72

Figure 35 Sagittal MR images of ⁵⁹Fe-SPION (26 ± 1 ug Fe and 840 ± 30 nCi) tail-vein injected nude mouse before (left) and 24 hours (right) after injection. The mouse was imaged with a Fast Imaging with Steady State Precession (FISP) sequence with a repeat time (TR) of 9.4 ms and echo time (TE) of 4.7 ms and number of scans averaged (NSA) of 4. A flip angle (FA) of 35° was used to achieve T2*/T1 weighted images. The blue arrows indicate the brain, the red arrows indicate the liver, and the yellows arrows indicate the bladder. averaged (NSA) of 4. A flip angle (FA) of 35° was used to achieve T2*/T1 weighted images. 72

Figure 36: Sagittal MR images of ⁵⁹Fe-SPION (26 ± 1 ug Fe and 840 ± 30 nCi) tail-vein injected nude mouse before (left) and 72 hours (right) after injection. The mouse was imaged with a Fast Imaging with Steady State Precession (FISP) sequence with a repeat time (TR) of 9.4 ms and echo time (TE) of 4.7 ms and number of scans averaged (NSA) of 4. A flip angle (FA) of 35° was used to achieve T2*/T1 weighted images. The blue arrows indicate the brain, the red arrows indicate the liver, and the yellows arrows indicate the bladder. 73

Figure 37: Sagittal MR images of ⁵⁹Fe-SPION (26 ± 1 ug Fe and 840 ± 30 nCi) tail-vein injected nude mouse before (left) and 144 hours (right) after injection. The mouse was imaged with a Fast Imaging with Steady State Precession (FISP) sequence with a repeat time (TR) of 9.4 ms and echo time (TE) of 4.7 ms and number of scans averaged (NSA) of 4. A flip angle

(FA) of 35° was used to achieve T2*/T1 weighted images. The blue arrows indicate the brain, the red arrows indicate the liver, and the yellow arrows indicate the bladder. 74

Figure 38: The MR contrast caused by the SPION injection as measured by ROI analysis of various tissues (top) and the %ID of those tissues from the biodistribution (below) for comparison. Mice were tail-vein injected with ⁵⁹Fe-SPION (26 ± 1 ug Fe and 840 ± 30 nCi) and imaged and sacrificed at different time points. 75

Figure 39: The standard curve of the % signal contrast versus ⁵⁹Fe-SPION iron concentration. The connecting line segments represent the linear interpolation used to evaluate values between the known concentrations. The phantom was imaged with a Fast Imaging with Steady State Precession (FISP) sequence with a repeat time (TR) of 9.4 ms and echo time (TE) of 4.7 ms and number of scans averaged (NSA) of 4. A flip angle (FA) of 35° was used to achieve T2*/T1 weighted images. 76

Figure 40: SPION iron concentration values are calculated from MRI ROI data and ⁵⁹Fe-SPION biodistribution %ID/g values for the liver (top), kidney (middle), and brain (bottom). Mice were tail-vein injected with ⁵⁹Fe-SPION (26 ± 1 ug Fe and 840 ± 30 nCi) and imaged and sacrificed at different time points. 77

Figure 41: ⁵⁹Fe-SPIONs (26 ± 1 ug Fe and 840 ± 30 nCi) tail-vein injected nude mouse before (left) and 24 hours (middle) after injection. The mouse was imaged with a Fast Imaging with Steady State Precession (FISP) sequence with a repeat time (TR) of 9.4 ms and echo time (TE) of 4.7 ms and number of scans averaged (NSA) of 4. A flip angle (FA) of 35° was used to achieve T2*/T1 weighted images. The blue arrows indicate the brain, the red arrows indicate the liver, and the yellow arrows indicate the bladder. The right image shows the % contrast map, calculated by the difference of the before and after (deformably co-registered) images, divided by the before injection image. 79

Figure 42: The acrylic glass cube functions as a phantom, holding the radionuclide loaded tube at four positions within the scanner. The cube is 5 cm in each dimension and has a density of 1.13 ± 0.05 g/cm³. The bores within the block, shown in the top right, are displaced by 0 mm × 0 mm, 0 mm × 10 mm, 15 mm × 15 mm, and 20 mm × 20 mm. The tube goes through bores, as shown (bottom). 82

Figure 43: Radionuclide filled vial, containing 16.8 mL of water. This vial serves as a phantom for sensitivity and count rate linearity measurements for ⁵²Mn, ¹⁸F, and ⁸⁹Zr. 84

Figure 44: The count rate linearity of ¹⁸F was assessed by plotting the observed counts versus the known activity in the phantom. The 16.9 mL phantom was imaged with a small animal PET scanner for 5 minutes at each activity with a 350 - 650 keV energy window. 86

Figure 45: The count rate linearity of ⁸⁹Zr was assessed by plotting the observed counts versus the known activity in the phantom. The 16.9 mL phantom was imaged with a small animal PET scanner for 5 minutes with a 350 - 650 keV energy window. 87

- Figure 46: The count rate linearity of ^{52}Mn was assessed by plotting the observed counts versus the known activity in the phantom. The 16.9 mL phantom was imaged with a small animal PET scanner for 5 minutes with a 350 - 650 keV energy window. 89
- Figure 47: [^{52}Mn]-MION loaded phantom was imaged with MRI and PET. The known probe concentrations gave MR contrast (left) and PET signal (right). Two different [^{52}Mn]-MIONs are in the phantom. Low activity (left part of the phantom) and high activity (right part of the phantom). The ringing artefact seen in the MR image is a result of the sharp discontinuity between the plastic of the vial and the water in each phantom and the finite number of harmonics used in the fourier series in image reconstruction, as known as the “Gibbs phenomenon.” It does not affect the ROI values, as long as the ROI covers a large area of the vial..... 90
- Figure 48: The MR contrast (red) and PET signal (blue) of a [^{52}Mn]-MIONs loaded phantom. The high activity [^{52}Mn]-MION vials shown in Figure 47 were quantified. The PET signal increases linearly with probe concentration, unlike the MR contrast which stops increasing at high MION concentrations..... 91
- Figure 49: The U87MG cells analyzed with flow cytometry were gated to select mainly living U87MG cells, and exclude apoptotic bodies and other cells recovered from tumor tissue.. 93
- Figure 50: Flow cytometry results of U87MG and MCF-7 cells before implantation as xenograft tumors in nude mice. U87MG cells show increased fluorescence with the $\alpha_v\beta_3$ antibody stain compared to unstained and isotype negative control stain, indicating that the $\alpha_v\beta_3$ integrin is expressed on the U87MG cells. The MCF-7 cells do not show a shift in fluorescence intensity, indicating a lack of $\alpha_v\beta_3$ integrin expression. 94
- Figure 51: Flow cytometry results of U87MG cells recovered from xenograft tumors used for the hybrid imaging study. The increased mean fluorescence intensity of the $\alpha_v\beta_3$ antibody stained cells compared to the unstained and isotype control stained cells indicates that the U87MG cells are expressing $\alpha_v\beta_3$ integrin *in vivo*..... 95
- Figure 52: The StreptavidinPE fluorescence signal from wells coated with different concentrations of integrin and different coating buffers. After coating, wells were incubated with biotinylated cRGD and then StreptavidinPE. 96
- Figure 53: Solid phase binding assay of conjugated and untargeted ^{52}Mn -MIONs with wells coated with $\alpha_v\beta_3$. The greater uptake of the cRGD targeted MIONs indicates the binding of the ^{52}Mn -MION-cRGD with the $\alpha_v\beta_3$ integrin. 97
- Figure 54: Each mouse in the imaging study had an individualized pallet that was used in both the MR and PET scanners. An outline of the mouse was drawn to increase positioning reproducibility, but because of the different shaped nose cones of the scanners, positioning was not entirely reproduced..... 99
- Figure 55: The %ID/g of ^{52}Mn -MION, quantified through ROI analysis of PET images. Contours were drawn based on co-registered CT and MR images. U87MG xenograph tumor bearing mice were tail-vein injected with untargeted [^{52}Mn]-MION ($162\pm 7 \mu\text{Ci}$,

110±5 mg of Fe), [⁵²Mn]-MION-cRGD (125±4 μCi, 86±3 mg of Fe), or [⁵²Mn]-MION-cRGD (115±3 μCi, 79±2 mg of Fe) and a blocking dose of 1.3 mg of free cRGD, and PET and MRI scanned at different time points..... 100

Figure 56: %ID/g of various tissues from ROI analysis of PET image data. Mice were injected with untargeted ⁵²Mn-MIONs (162±7 μCi, 110±5 mg of Fe) and show high uptake in the liver at both time points. Tumor and brain accumulation is low, while kidney uptake is moderate..... 101

Figure 57: %ID/g of various tissues from ROI analysis of PET image data. Mice were injected with ⁵²Mn-MION-cRGDs (125±4 μCi, 86±3 mg of Fe) and show high uptake in the liver at both time points. Brain accumulation is low, while kidney uptake is moderate. Tumor uptake is increased compared to the untargeted nanoparticles. 102

Figure 58: %ID/g of various tissues from ROI analysis of PET image data. Mice were injected with ⁵²Mn-MION-cRGDs (115±3 μCi, 79±2 mg of Fe) and a blocking dose of 1.3 mg of free cRGD and show high uptake in the liver at both time points. Brain accumulation is low, while kidney uptake is moderate. Tumor uptake is initially high, but decreases at the 24 hour time. 102

Figure 59: Selected PET/CT images of U87MG tumor bearing mouse tail vein injected with untargeted ⁵²Mn-MION (162±7 μCi, 110±5 mg of Fe) 3 hours after injection. The left coronal image shows the right shoulder tumor (arrow). The right sagittal view shows high signal from the liver (arrow)..... 103

Figure 60: Selected PET/CT images of U87MG tumor bearing mouse tail vein injected with untargeted ⁵²Mn-MION (162±7 μCi, 110±5 mg of Fe) 24 hours after injection. The left coronal image shows the right shoulder tumor (arrow). The right sagittal view shows high signal from the liver (arrow)..... 104

Figure 61: Selected PET/CT images of U87MG tumor bearing mouse tail vein injected with cRGD targeted ⁵²Mn-MION (125±4 μCi, 86±3 mg of Fe) 3 hours after injection. The left coronal image shows the right shoulder tumor (arrow). The right sagittal view shows high signal from the liver (arrow)..... 104

Figure 62: Selected PET/CT images of U87MG tumor bearing mouse tail vein injected with cRGD targeted ⁵²Mn-MION (125±4 μCi, 86±3 mg of Fe) 24 hours after injection. The left coronal image shows the right shoulder tumor (arrow). The right sagittal view shows high signal from the liver (arrow).-..... 105

Figure 63: Selected PET/CT images of U87MG tumor bearing mouse tail vein injected with cRGD targeted ⁵²Mn-MION (115±3 μCi, 79±2 mg of Fe) 3 hours after injection. The left coronal image shows the right shoulder tumor (arrow). The right sagittal view shows high signal from the liver (arrow)..... 105

Figure 64: Selected PET/CT images of U87MG tumor bearing mouse tail vein injected with cRGD targeted ⁵²Mn-MION (115±3 μCi, 79±2 mg of Fe) 24 hours after injection. The left

coronal image shows the right shoulder tumor (arrow). The right sagittal view shows high signal from the liver (arrow). 106

Figure 65: PET/CT image of $^{52}\text{MnCl}_2$ (73 μCi) injected mouse. The left coronal view shows high liver (arrow) signal, while the right sagittal view also shows considerable kidney signal. 107

Figure 66: Biodistribution of a $^{52}\text{MnCl}_2$ injected mouse 24 hours post-injection. A nude mouse was tail-vein injected with 73 μCi of $^{52}\text{MnCl}_2$ and sacrificed after 24 hours. The tissues were collected and weighed and the %ID/g was calculated for various tissue. The high uptake in the liver and kidneys parallels the PET data, shown in Figure 65. 107

Figure 67: Select images of untargeted ^{52}Mn -MION injected (162 \pm 7 μCi , 110 \pm 5 mg of Fe) mouse before (left), 3 hours after (middle), and 24 hours after (right) injection. The mouse was imaged with a Fast Imaging with Steady State Precession (FISP) sequence with a repeat time (TR) of 9.4 ms and echo time (TE) of 4.7 ms and number of scans averaged (NSA) of 4. A flip angle (FA) of 35 $^\circ$ was used to achieve T2*/T1 weighted images. The blue arrows indicate the tumor, the red arrows indicate the liver, and the yellows arrows indicate the kidneys. 108

Figure 68: Select images of cRGD targeted ^{52}Mn -MION injected (125 \pm 4 μCi , 86 \pm 3 mg of Fe) mouse before (left), 3 hours after (middle), and 24 hours after (right) injection. The mouse was imaged with a Fast Imaging with Steady State Precession (FISP) sequence with a repeat time (TR) of 9.4 ms and echo time (TE) of 4.7 ms and number of scans averaged (NSA) of 4. A flip angle (FA) of 35 $^\circ$ was used to achieve T2*/T1 weighted images. The blue arrows indicate the tumor, the green arrows indicate the brain. The liver and kidneys are not visible in this image. 109

Figure 69: Select images of cRGD targeted ^{52}Mn -MION and blocking free cRGD injected (115 \pm 3 μCi , 79 \pm 2 mg of Fe) mouse before (left), 3 hours after (middle), and 24 hours after (right) injection. The mouse was imaged with a Fast Imaging with Steady State Precession (FISP) sequence with a repeat time (TR) of 9.4 ms and echo time (TE) of 4.7 ms and number of scans averaged (NSA) of 4. A flip angle (FA) of 35 $^\circ$ was used to achieve T2*/T1 weighted images. The blue arrows indicate the tumor, the red arrows indicate the liver, and the yellows arrows indicate the bladder. The kidneys are not visible in this image. 110

Figure 70: The % contrast induced in tumor tissue by ^{52}Mn -MION injection, quantified through ROI analysis of MR images. Contours were drawn based on co-registered the MR images. U87MG xenograph tumor bearing mice were tail-vein injected with untargeted [^{52}Mn]-MION (162 \pm 7 μCi , 110 \pm 5 mg of Fe), [^{52}Mn]-MION-cRGD (125 \pm 4 μCi , 86 \pm 3 mg of Fe), or [^{52}Mn]-MION-cRGD (115 \pm 3 μCi , 79 \pm 2 mg of Fe) and a blocking dose of 1.3 mg of free cRGD. 111

Figure 71: The % contrast induced by untargeted ^{52}Mn -MION injection (162 \pm 7 μCi , 110 \pm 5 mg of Fe) in specific tissues measured with ROI analysis. The % contrast is measured as the percent signal decrease of the ROI compared with the ROI of the same tissue imaged before injection. 111

- Figure 72: The % contrast induced by cRGD- ⁵²Mn-MION injection (125±4 μCi, 86±3 mg of Fe) in specific tissues measured with ROI analysis. The % contrast is measured as the percent signal decrease of the ROI compared with the ROI of the same tissue imaged before injection..... 112
- Figure 73: The % contrast induced by cRGD- ⁵²Mn-MION (115±3 μCi, 79±2 mg of Fe) and blocking free cRGD injection in specific tissues measured with ROI analysis. The % contrast is measured as the percent signal decrease of the ROI compared with the ROI of the same tissue imaged before injection. 112
- Figure 74: Coronal images of an untargeted ⁵²Mn-MION injected (162±7 μCi, 110±5 mg of Fe) mouse 24 hours after injection. The MR image of the mouse before injection is on the far left, while the MR image of the mouse 24 hours after injection is on the left middle. The PET scan of the mouse after 24 hours is on the middle right, while the co-registered pre-injection MR image with the PET image is on the far right. 113
- Figure 75: Coronal images of a ⁵²Mn-MION-cRGD (125±4 μCi, 86±3 mg of Fe) injected mouse 24 hours after injection. The MR image of the mouse before injection is on the far left, while the MR image of the mouse 24 hours after injection is on the left middle. The PET scan of the mouse after 24 hours is on the middle right, while the co-registered pre-injection MR image with the PET image is on the far right. 114
- Figure 76: Coronal images of an ⁵²Mn-MION-cRGD (115±3 μCi, 79±2 mg of Fe) with blocking cRGD injected mouse 24 hours after injection. The MR image of the mouse before injection is on the far left, while the MR image of the mouse 24 hours after injection is on the left middle. The PET scan of the mouse after 24 hours is on the middle right, while the co-registered pre-injection MR image with the PET image is on the far right..... 114

List of Abbreviations

The reader is assumed to possess basic knowledge of measurement units and their prefixes, scientific symbols, and abbreviations in common usage. Examples are meters (m), grams (g), liters (L), kilo- (k), mega- (M), proton (p), neutron (n), Fluorine-18 (^{18}F), deoxyribonucleic acid (DNA). Where appropriate, units were chosen to be consistent with those employed by other investigators in the field. Some quantities are therefore non in SI units, such as mCi.

%ID/g	Percent injected dose per gram
%SC	Percent signal contrast
^{11}C -PIB	^{11}C -labeled Pittsburgh Compound-B
^{11}C -R116301	^{11}C labeled selective NK1 receptor antagonist
^{18}F SPARQ	^{18}F labeled substance P antagonist receptor quantifier
^{18}F -DOPA	^{18}F -dihydroxyphenylalanine
^{18}F -FDG	[^{18}F]-fludeoxyglucose
^{18}F -FDHT	16 β -[^{18}F]-Fluoro-5 α -dihydrotestosterone
^{18}F -FECNT	2 β -carbomethoxy-3 β -(4-chlorophenyl)-8-(2-[^{18}F]-fluoroethyl)nortropine
^{18}F -FES	16 α -[^{18}F]-fluoro-17 β -oestradiol
^{18}F -FHBG	9-(4- ^{18}F -fluoro-3-[hydroxymethyl]butyl)guanine
^{18}F -FLT	[^{18}F]-fluorothymidine
^{18}F -FMAU	^{18}F -1-(2'-deoxy-2'-fluoro-beta-d-arabinofuranosyl)thymine
^{18}F -FMISO	[^{18}F]-fluoromisonidazole
^{18}F -FU	[^{18}F]-fluorouracil

^{60}Cu -ATSM	$[^{64}\text{Cu}]$ -diacetyl-bis (N4 - methylthiosemicarbazone)
ACAC	Acetylacetonate
AMIDE	A medical imaging data examining software
APD	Avalanche photodiode
BSA	Bovine serum albumin
CPM	Counts per minute
cRGD	Cyclo(Arg-Gly-Asp) peptide
CT	Computed tomography
DICOM	Digital imaging and communications in medicine
DLS	Dynamic light scattering
DMSO	Dimethyl sulfoxide
DOTA	1,4,7,10-tetraazacyclododecane-1,4,7,10-tetraacetic acid
DPM	Decays per minute
DTPA	diethylene-triamine penta-acetic acid
EC	Electron capture
EDC	1-ethyl-3-(3-dimethylaminopropyl)carbodiimide
FA	Flip angle
FBP	Filtered back projection
FDA	United States Food and Drug Administration
FISP	Fast Imaging with Steady State Precession
FOV	Field of view
FSC	Forward scatter

HER2/neu	Human epidermal growth factor receptor 2
IACUC	Institutional Animal Care and Use Committee
ICP	Inductively coupled plasma
ICP-MS	Inductively coupled plasma mass spectrometry
ICP-OES	Inductively coupled plasma optical emission spectrometry
ID	Injected dose
LOR	Line of response
MCF-7	Michigan Cancer Foundation-7 breast cancer cell line
MIONs	Manganese iron oxide nanoparticle
MR	Magnetic resonance
MRA	Magnetic resonance angiography
MRI	Magnetic resonance imaging
MSME	Multiple-slice multiple-echo
MW	Molecular weight
NDA	Nitrodopamine
NHL	Non-Hodgkin lymphoma
NHS	N-hydroxysuccinimide
NSA	Number of scans averaged
OCT	Optical coherence tomography
OSEM	Ordered subsets expectation maximization
PAA	Poly(acrylic acid)
PBS	Phosphate buffered saline
PEG	Polyethylene glycol
PET	Positron emission tomography

PMT	Photomultiplier tube
PSMA	prostate specific membrane antigen
R ₁	Longitudinal relaxivity
R ₂	Transverse relaxivity
RCF	Relative centrifugal force
RES	Reticuloendothelial system
RF	Radiofrequency field
ROI	Region of interest
r-SPNP	Radio-superparamagnetic nanoparticle
SAR	Specific absorption rate
SDS	Sodium dodecyl sulfate
SMCC	4-(N-Maleimidomethyl)cyclohexane-1-carboxylic acid
SNR	Signal to noise ratio
SPECT	Single photon emission tomography
SPIO	Superparamagnetic iron oxide
SPION	Superparamagnetic iron oxide nanoparticle
SSC	Side scatter
STDV	Standard deviation
T1	Longitudinal relaxation time
T2	Transverse relaxation time
TE	Echo time
TEM	Transmission electron microscopy
TETA	1,4,8,11-tetraazacyclotetradecane-N,N',N'',N'''-tetraacetic acid
TOA	Triethylamine

TR	Repetition time
U87MG	Human glioblastoma-astrocytoma, epithelial-like cell line
USPIO	Ultra-small superparamagnetic iron oxides
UT	Ultrasound
$\alpha_v\beta_3$	Alpha(V) Beta(3)

Chapter 1

1. Introduction

Recent development of hybrid PET/MRI imaging systems has not yet been paralleled with the development of a truly hybrid intrinsic PET/MRI probe. This work has created a novel radio-intrinsic nanoparticle probe for hybrid PET/MR imaging. This was accomplished with a manganese iron oxide nanoparticle (MION) that intrinsically incorporates the PET imaging radionuclide, ^{52}Mn . This probe brings to molecular imaging a single imaging agent that is detectable with PET and MRI, in order to combine the complementary strengths of each modality.

1.1. Objectives

The aim of this research is to develop, characterize, and evaluate a hybrid PET/MR nanoparticle probe. The specific objectives of this project are:

1. Synthesize a radioactive superparamagnetic nanoparticle (r-SPNP) that intrinsically incorporates a positron emitting radionuclide for PET signal and MR imaging.
2. Investigate a surface coating appropriate for *in vivo* imaging.
3. Evaluate the nanoparticle's physicochemical characteristics for both PET and MR imaging.
4. Conjugate the r-SPNP surface coating with cyclo(Arg-Gly-Asp) targeting peptide (cRGD) and image the biological expression of $\alpha_v\beta_3$ integrin *in vivo*.
5. Quantify PET signal and relate it to the MR contrast resulting from the nanoparticle probe.

1.2. Strategy

This project exploits the radiometal, ^{52}Mn , which gives PET signal through its positron emission and can be intrinsically incorporated into MION structures to give MR contrast. In this research, monocrystalline SPIONs and MIONs were produced through high temperature thermal decomposition synthesis. Intrinsically incorporated into these nanoparticles are two radionuclides. First ^{59}Fe [$t_{1/2} = 44.5$ days, $\gamma = 1099$ keV (56%) and 1292 keV (44%)] was incorporated into a SPION, as a surrogate for ^{52}Fe . Its long half-life and gamma emission were suitable for developing the incorporation chemistry and for use in biodistribution studies. For PET imaging, ^{52}Mn ($t_{1/2} = 5.591$ days, 29.6% β^+) was incorporated into MIONs and utilized in imaging studies. ^{52}Fe was not utilized for incorporation and PET imaging studies, because to achieve the $^{55}\text{Mn}(p,4n)^{52}\text{Fe}$ reaction, 50-60 MeV protons are needed, and the cyclotron facilities needed for this energy range were not available. These r-SPNPs were coated with a multidentate catechol-based polyethylene glycol oligomersin, which can be modified and conjugated to targeting moieties. The targeting molecule chosen to for conjugation with the ^{52}Mn -MIONs was cyclo(Arg-Gly-Asp) peptide, which has been previously used to target the $\alpha_v\beta_3$ integrin with PET and MRI. The use of these cRGD conjugated ^{52}Mn -MIONs for *in vivo* targeted molecular imaging was demonstrated in U87MG xenograft tumor bearing nude mice.

1.2.1. Extrinsically vs. Intrinsically Radio-labeled Nanoparticles

There are two main approaches to incorporate a radionuclide into nanoparticles, as shown in Figure 1. The first strategy is to externally radiolabel nanoparticles using a linker, such as radio-chelate complexes. There are potential limitations of external labeling strategies. The external label changes the chemical structure of the nanoparticle probe, which may change its *in vivo* pharmacokinetics. The external label is on the surface of the nano-structure and is exposed to

chemical and enzymatic activity that may separate the radionuclide from the nanoparticle.¹ This could compromise the label's usefulness for multi-modal imaging. The second strategy, utilized in this work, intrinsically incorporates the radionuclide into the core structure of the nanoparticle. This will ensure effective shielding of the radionuclide within the nano-construct, thereby providing a pharmacokinetic profile indicative of the overall nanoparticle. Additionally, this will simplify the surface coating chemistry and offer a greater surface area for conjugation of the targeting moiety. The intrinsic incorporation of the radionuclide has limitations as well. Radio-intrinsic nanoparticles must be synthesized new for each imaging study, as opposed to an extrinsic chelator, where the imaging agent can be synthesized and stored for a time and radionuclide can then be produced and chelated as needed. Additionally, the synthesis of the rSPNPs cannot be scaled down indefinitely. This means that in order to manipulate the ratio of activity to NP mass, increasingly large activities must be utilized.

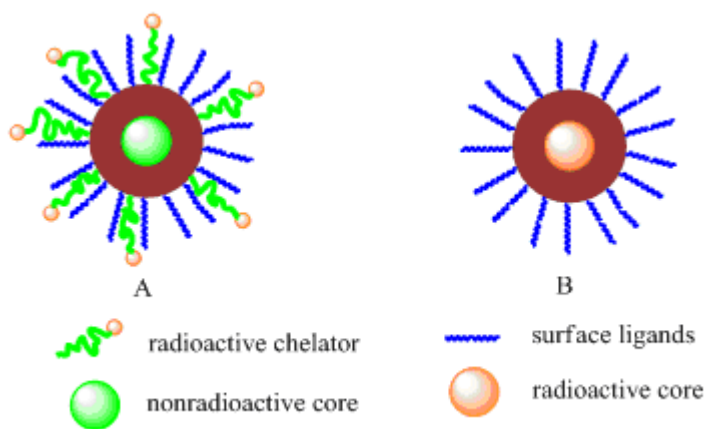


Figure 1: The radioactive chelator model (A) externally labels the nanoparticle, while the radio-intrinsic model (B) internally incorporates the radioactivity in the nanoparticle.

1.2.2. Radio-intrinsic Superparamagnetic Nanoparticle

For the intrinsic inclusion of radionuclides into the nanoparticle structure, ⁵⁹Fe and ⁵²Mn were used for incorporation. These radionuclides are chemically identical to the iron and manganese

used for the SPION and MION structures. While other imaging radionuclides, such as ^{89}Zr , ^{64}Cu , or ^{55}Co , are candidates for incorporation, the manganese and iron radionuclides utilized in this project do not change the chemical structure or physical characteristics of the nanoparticle. This strategy lessens the possibility of the radio-incorporation damaging the MR contrast characteristics. Additionally, this approach avoids the possibility of un-chelated moieties being present on the nanoparticle coating, which could increase the nanoparticles binding with plasma proteins, increase the nanoparticle's size, and change the pharmacokinetic profile.

Chapter 2

2. Background

Cancer is a family of over 200 diseases associated with the dysregulation of cellular proliferation and growth. Medically known as malignant neoplasm, cancer is the leading cause of death in economically developed countries and the second leading cause of death in developing countries, with an estimated 12.7 million cancer cases and 7.6 million cancer deaths worldwide in 2008.² Major efforts are being made to gain insights into the pathology, and treatment of these diseases. Research into the behavior of malignant tissues aids in developing disease treatment, by revealing the molecular biology and biochemistry of cancerous cells.

In order to develop into cancer, potentially malignant cells must gain a number of biological capabilities, including sustaining proliferative signaling, evading growth suppressors, resisting cell death, enabling replicative immortality, inducing angiogenesis, and activating invasion and metastasis.³ The successful treatment of cancer is greatly aided by detecting cancer cells early in this process. Additionally, anti-cancer therapy has been progressed by the implementation of personalized medicine, where a patient's treatment is tailored to the unique set of molecular aberrations driving his/her disease.⁴ Medical imaging is an important clinical tool to achieve both of these goals.

2.1. Medical Imaging of Cancer

A number of imaging modalities are used in the detection and characterization of cancer.

Anatomical imaging techniques are used for diagnosis, surgical guidance/follow-up, and

treatment monitoring. These anatomical imaging modalities include radiography, computed tomography (CT), ultrasound (UT), and MRI. One of the major challenges to anatomical imaging of cancer is low contrast. Malignant tissue often has similar physical properties to normal tissue, making the detection and delineation of small tumors or metastases difficult. Additionally, the sub-clinical disease or microscopic extent, including micro-metastases micro-extensions, often will not give sufficient contrast for detection.

2.2. Molecular Imaging of Cancer

The clinical effort for early detection of cancer and the application of personalized anticancer therapies has been aided by the development of molecular imaging. Drug discovery and development has also been assisted with the application of molecular imaging technology for characterizing novel drug pharmacokinetics.⁵ Furthermore, research into the molecular biology and biochemistry has been advanced by the application of molecular imaging.⁶ A number of imaging modalities are utilized in molecular imaging. A number of these modalities and some of their characteristics are described in Table 1. This project focuses on PET and MRI, which are detailed further in Sections 2.3 and 2.4.

Table 1: Characteristics of medical imaging modalities that have molecularly targeted imaging agents or non-targeted agents.

Modality	Advantages	Disadvantages	Imaging agent	Clinical examples
Computed tomography	<ul style="list-style-type: none"> • Unlimited depth penetration • High spatial resolution • Whole-body imaging possible • Short acquisition time (minutes) • Moderately expensive • Anatomical imaging 	<ul style="list-style-type: none"> • Radiation exposure • Poor soft-tissue contrast • Probably not used for molecular imaging; currently only 	<ul style="list-style-type: none"> • Barium • Iodine • Krypton • Xenon 	<ul style="list-style-type: none"> • Tumor perfusion

		anatomical and functional imaging		
Positron emission tomography	<ul style="list-style-type: none"> • Highly penetrating signal • Whole-body imaging possible • Quantitative molecular imaging • Can be combined with CT or MRI for anatomical information 	<ul style="list-style-type: none"> • Radiation exposure • Expensive • Low spatial resolution (1–2 mm pre-clinical, 6-7 mm clinical) • Long acquisition times (minutes to hour) 	<ul style="list-style-type: none"> • ^{11}C • ^{18}F • ^{64}Cu • See Table 2 	<ul style="list-style-type: none"> • ^{18}F-FDG-PET for cancer staging • Diagnosis of various diseases (see Table 2)
Single photon-emission computed tomography	<ul style="list-style-type: none"> • Highly penetrating signal • Whole-body imaging possible • Quantitative molecular imaging • Theranostic: can combine imaging and radiotherapy • Can be combined with CT for anatomical information 	<ul style="list-style-type: none"> • Radiation exposure • Low spatial resolution (0.3–1 mm preclinical, ~1 cm clinical) • Long acquisition time 	<ul style="list-style-type: none"> • $^{99\text{m}}\text{Tc}$ • ^{123}I • ^{111}In • ^{177}Lu 	<ul style="list-style-type: none"> • Diagnosis of various diseases • Radiotherapy for NHL: ^{90}Y-Bexxar or ^{131}I-Zevalin • Radiotherapy of thyroid carcinoma with ^{131}I-iodide
Magnetic resonance imaging	<ul style="list-style-type: none"> • Highly penetrating signal • Whole-body imaging possible • No ionizing irradiation • Excellent soft-tissue contrast • High spatial resolution 	<ul style="list-style-type: none"> • Expensive • Long acquisition time (min-hours) • Limited sensitivity for detection of molecular contrast agents 	<ul style="list-style-type: none"> • Gadolinium (Gd^{3+}) • Iron oxide particles • Manganese oxide • ^{19}F 	<ul style="list-style-type: none"> • SPIOs for detection of lymph node metastases of prostate cancer • Characterization of focal hepatic lesions • Perfusion imaging of the heart
Magnetic resonance spectroscopy	<ul style="list-style-type: none"> • Whole-body imaging possible • No ionizing irradiation 	<ul style="list-style-type: none"> • Expensive • Long acquisition time (min-hours) • Low sensitivity 	<ul style="list-style-type: none"> • Choline • Creatine • Lactate • Lipids • Polyamines • N-acetyl- 	<ul style="list-style-type: none"> • Metabolite levels in brain tumors • Treatment monitoring of

			aspartate	Alzheimer's
Ultrasound	<ul style="list-style-type: none"> • No ionizing irradiation • Real-time imaging/short acquisition time (min) • High spatial resolution • Can be applied externally or internally (endoscopy) • Inexpensive • Highly sensitive 	<ul style="list-style-type: none"> • Clinical whole-body imaging not possible • Contrast agents currently limited to vasculature • Operator dependency 	<ul style="list-style-type: none"> • Contrast micro-bubbles 	<ul style="list-style-type: none"> • Characterization of focal liver lesions • Echocardiography • Tumor perfusion of cancer
Optical	<ul style="list-style-type: none"> • No ionizing irradiation • Real-time imaging/short acquisition time (sec-min) • Relatively high spatial resolution • Can be applied externally or internally (endoscopy) • Inexpensive • Highly quantitative and sensitive • Multiplexing 	<ul style="list-style-type: none"> • Limited depth penetration (≤ 1 cm) • Clinical whole-body imaging not possible 	<ul style="list-style-type: none"> • Fluorescent molecules and dyes • Light-absorbing nanoparticles • Quantum dots 	<ul style="list-style-type: none"> • OCT imaging of arteriosclerosis • OCT imaging for colonoscopy screening • Raman imaging of skin cancer

2.3. Positron Emission Tomography

Positron emission tomography is a molecular imaging technique that has wide research and clinical management applications, particularly in cancer.⁷ PET has made large contributions to molecular imaging with the application of a variety of radiotracers. A radiotracer is a chemical structure that incorporates a positron emitting radionuclide. A number of PET imaging radionuclides are described later, in Section 2.3.2. The PET pharmaceutical is introduced to a living organism through a variety of methods, mainly through intravenous injection, and the subject is imaged during or sometime after administration. The PET image shows the spatial distribution and concentration of the probe with respect to time. The body's handling and

distribution or pharmacokinetics of the PET radiotracer depends on the chemical structure, and affect the final PET image.

PET radiotracers have been developed and utilized for studying brain and heart function, but most widely in oncology.⁸ Specifically, PET pharmaceuticals have been developed that target malignant tumors for the localization and characterization of these cancers. The tracers function principally by targeting physiological processes or conditions that are up-regulated as a consequence of malignant involvement, such as perfusion, bone deposition, glucose metabolism, cell proliferation, or antigen and receptor expression. Additionally, the kinetics anti-tumor drugs have been evaluated through molecular imaging studies.⁹ The strategy for drug pharmacokinetic evaluation has become widely utilized in novel drug development. Table 2 details a number of PET tracers used for clinical imaging of disease.

Table 2: PET tracers used for the imaging of disease.

Medical imaging	Target	Radiotracer(s)	Clinical applications
Oncological imaging	Protein synthesis	¹¹ C-methionone, ¹¹ C-tyrosine	Protein synthesis in tumors
	Glucose transporter	¹⁸ F-FDG	Glucose metabolism in tumors
	Choline transporter	¹¹ C-choline	Tumor phospholipid synthesis
	Thymidine uptake in DNA/RNA synthesis	¹⁸ F-FLT, ¹⁸ F-FMAU; ¹⁸ F-FU	Tumor cell proliferation
	Phosphatidylserine $\alpha_v\beta_3$ integrin	¹²⁴ I-annexin-V	Apoptosis
	HSV1-tk	¹⁸ F-galacto-RGD	Tumor angiogenesis
	Hypoxia	¹⁸ F-FHBG	Suicidal gene therapy
		¹⁸ F-FMISO; ⁶⁴ Cu-, ⁶⁰ Cu-ATSM	Tumor hypoxia
	Somatostatin receptor	⁶⁴ Cu-TETA-octreotide	Neuroendocrine tumors
	Oestrogen receptor	¹⁸ F-FES	Breast cancer
Androgen receptor	¹⁸ F-FDHT	Prostate cancer	
Bone deposition	¹⁸ F-	Oncology	
Perfusion	H ₂ ¹⁵ O, C ¹⁵ O ₂ , ¹³ NH ₃ ,	Oncology, Brain	

Cardiovascular imaging	Cell metabolism	$^{11}\text{CO}_2$, ^{82}Rb	Ischemia
	Fatty acid metabolism	^{11}C acetate	Cardiac metabolism
	Adrenergic neurotransmission	^{11}C palmitate	Ischaemia
	Cardiac sympathetic neurons	^{11}C methoxyephedrine	Heart failure
Neurological imaging	Cardiac sympathetic neurons	^{18}F norepinephrine	Cardiac sympathetic innervation
	Dopamine post synaptic receptors	^{11}C raclopride	Schizophrenia, addiction
	β -amyloid	^{11}C -PIB	Alzheimer's disease
	NK-1 receptor	^{18}F -SPARQ; ^{11}C -R116301	Depression, anxiety
	Dopamine transporter	^{18}F -FECNT	Schizophrenia, addiction
	Dopamine metabolism	^{18}F -DOPA	Schizophrenia, addiction

2.3.1. Decay, Annihilation, and Coincidence Detection

While inside the body, the radiotracer will undergo radioactive decay. A portion of those decays yield positrons, which have a kinetic energy spectrum that depends on the radionuclide. This kinetic energy will be lost by the positron as it interacts traveling a short distance through tissue. This distance will be discussed further in Section 2.3.2. Once the positron has lost most of its kinetic energy, it will annihilate with an electron. This annihilation produces two 511 keV gamma rays, emitted almost exactly 180° away from each other, as shown in Figure 2. The deviation from 180° is a result of the combined momentum of the annihilated electron and positron, and it is typically 0.25° . The distance traveled by the positron from the decay event to the annihilation event and the acolinearity of the annihilation gamma rays represent losses in spatial resolution that cannot be recovered during image reconstruction.

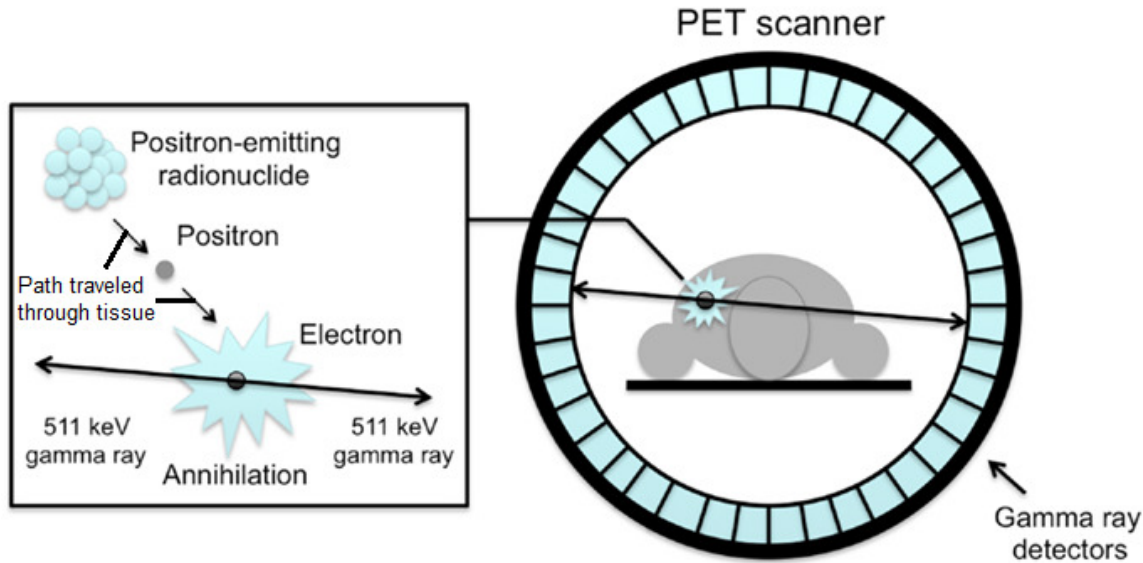


Figure 2: A positron emitting radionuclide decays and yields a positron that travels a distance through tissue and annihilates with an electron. This emits two 511 keV photons that exit the body and are detected by the array of scintillation crystal for image reconstruction.

The annihilation gamma photons pass through the body and those that emerge can be registered by a detector array of scintillation crystals arranged in opposing banks, as shown in Figure 2.

The gamma ray interactions are paired when one ray of the correct energy is detected within a short time interval (coincidence window) of another ray detection. In the case of these “true” detections, the gamma ray pairs are then designated as originating from the same annihilation that occurred on a “line of response” (LOR) between the two detectors. These LORs are stored as projections.

There is a probability that one or both of the annihilation gamma rays will interact with the tissue before exiting the body (scatter or attenuation) or exit the scanner without being detected. When this occurs, coincidence events other than “true” detections can be recorded. As shown in Figure 3, this can result in random and scattered detections. In scattered coincidence events, one or both of the gamma rays are scattered within the subject, but both are detected within the coincidence window with the appropriate energy. The non-perfect time and energy resolution of PET

scanners allow for the detection of scattered events. Random coincidence events occur when two photons from different annihilation events are detected and recorded. This is a result of the finite temporal resolution of PET scanners.

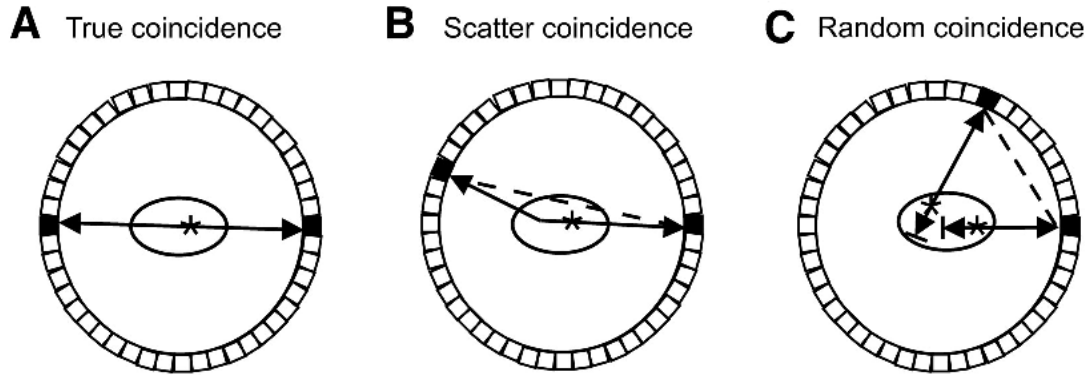


Figure 3: A) True coincidence detection occurs when the two gamma rays from an annihilation event exit the body and are detected by the scintillation crystals within the energy and time windows allowed for coincidence. B) If one or both of the photons are scattered, but are still detected within the time and energy windows, then a scattered coincidence has occurred. C) When two photons from different annihilation events are detected, a random coincidence has occurred.

Scattered and random events result in incorrectly registered annihilations events. This leads to decreased image contrast and increased noise. Corrections are applied to the LORs for the scattered and random fractions, as well as detector dead time, attenuation, and variations in detector element sensitivity. From this corrected emission data, PET images are reconstructed. Reconstruction can be accomplished with analytical approaches, such as filtered back projection (FBP) or using iterative methods, such as ordered subsets expectation maximization (OSEM).¹⁰

2.3.2. PET Radionuclides

A number of radionuclides are used for PET tracers. Among them are several biologically relevant organic radionuclides that can be incorporated into organic compounds. These organic radionuclides have relatively short half-lives that require rapid radiochemistry and onsite cyclotron production or immediate delivery. The characteristics of a variety of these organic

PET radionuclides are shown in Table 3.¹¹ Note that while ^{18}F is not organic, it is used to replace a hydrogen atom in many organic compounds.

Table 3: The characteristics of organic PET radionuclides.

Nuclide	Half-life	Decay Modes	Maximum positron energy (MeV) and yield (%)	Production
^{11}C	20.4 mins	EC, β^+	0.961 (99.8%)	$^{14}\text{N}(\text{p},\alpha)^{11}\text{C}$
^{13}N	9.96 mins	EC, β^+	1.2 (99.8%)	$^{16}\text{O}(\text{p},\alpha)^{13}\text{N}$
^{15}O	2.04 mins	EC, β^+	1.73 (99.9%)	$^{15}\text{N}(\text{p},\text{n})^{15}\text{O}$ $^{14}\text{N}(\text{d},\text{n})^{15}\text{O}$
^{18}F	109.8 mins	EC, β^+	0.634 (96.7%)	$^{18}\text{O}(\text{p},\text{n})^{18}\text{F}$ $^{20}\text{Ne}(\text{d},\alpha)^{18}\text{F}$

Another group of PET radionuclides are inorganic atoms that tend to have longer half-lives. This makes them accessible for more complex radiochemistry and applicable to use in tracers with slower pharmacokinetics, such as macromolecules, and in longitudinal studies. Some of these radionuclides are produced by generator systems and are shown in Table 4.^{12,13,14} Other cyclotron produced PET radionuclides are shown in Table 5.¹⁵ These radiometals have been widely utilized in tumor imaging, as well as therapy through α , β^- , and Auger electron emission.¹⁶

Table 4: The characteristics of various inorganic generator produced PET radionuclides.

Nuclide	Half-life	Decay Modes	Maximum positron energy (MeV) and yield (%)	Production
$^{62}\text{Zn}/^{62}\text{Cu}$	9.19 hrs / 9.74 mins	EC, β^+	2.93 (97.4%)	$^{63}\text{Cu}(\text{p},2\text{n})^{62}\text{Zn}$
$^{68}\text{Ge}/^{68}\text{Ga}$	288 days / 68 mins	EC, β^+	1.899 (87.7%) 0.821 (1.2%)	$^{68}\text{Ga}(\text{p},2\text{n})^{68}\text{Ge}$
$^{82}\text{Sr}/^{82}\text{Rb}$	25.6 days / 1.27 mins	EC, β^+	3.38 (95.5%)	$^{85}\text{Rb}(\text{p},4\text{n})^{82}\text{Sr}$

Table 5: The characteristics of various inorganic cyclotron produced PET radionuclides.

Nuclide	Half-life	Decay Modes	Maximum positron energy (MeV) and yield (%)	Production
$^{52}\text{Mn}^{(17)}$	5.6 days	EC, β^+	0.575 (29.6%)	$^{52}\text{Cr}(p,n)^{52}\text{Mn}$
$^{52}\text{Fe}^{(18)}$	8.275 hrs	EC, β^+	0.804 (55.5%)	$^{52}\text{Cr}(^3\text{He},2n)^{52}\text{Fe}$ $^{52}\text{Cr}(\alpha,3n)^{52}\text{Fe}$ $^{55}\text{Mn}(p,4n)^{52}\text{Fe}$
$^{55}\text{Co}^{(19)}$	17.54 hrs	EC, β^+	1.950(45.7%) 1.431(3.05%) 1.311(43.7%)	$^{56}\text{Fe}(p,2n)^{55}\text{Co}$
^{64}Cu	12.7 hrs	EC, β^+ , β^-	0.653 (17.4%)	$^{62}\text{Ni}(p,n)^{64}\text{Cu}$
^{67}Br	16.2 hrs	EC, β^+	3.941 (54.7%)	$^{76}\text{Se}(p,n)^{76}\text{Br}$
$^{86}\text{Y}^{(20)}$	14.74 hrs	EC, β^+	3.141 (31.9%)*	$^{86}\text{Sr}(p,n)^{86}\text{Y}$
$^{89}\text{Zr}^{(21)}$	78.41 hrs	EC, β^+	0.897 (22.3%)	$^{89}\text{Y}(p,n)^{89}\text{Zr}$
^{124}I	4.18 days	EC, β^+	2.138 (23.0%)	$^{126}\text{Te}(p,3n)^{124}\text{I}$

*Many β^+ decays are possible for ^{86}Y , with maximum energy of 3.131 MeV, average energy of 0.664 MeV, and total yield of 31.9%.

As discussed earlier in Section 2.3.1, when imaging PET radionuclides, after the decay event, the emitted positron will travel a distance, while losing kinetic energy, before annihilating with an electron. The length of the mean free path of these positrons results in a loss of spatial resolution. For all PET radionuclides, a greater the positron energy causes a longer the mean free path, and the greater loss in spatial resolution. Therefore, the maximum positron energy is an important characteristic of all PET radionuclides.

2.4. Magnetic Resonance Imaging

Magnetic Resonance Imaging (MRI) is a powerful 3-dimensional imaging technique that has become widely used for medical imaging. MRI provides good soft tissue contrast and sub-millimeter spatial resolution, while avoiding patient exposure to ionizing radiation. Its

anatomical imaging applications include cardiac imaging, neuroimaging, musculoskeletal imaging, to angiography.²²

During an MRI scan, the subject is placed in the bore of a powerful magnet with an external magnetic field, B_0 . This aligns the net magnetization of the tissues of the patient in the “z” direction, which is in the direction of the length of the bore. The aligned particles precess around the “z” direction at the Larmor frequency, shown in Equation 1, where γ is the gyromagnetic ratio of the particles of interest (42.58 MHz/T for ^1H).

$$f_0 = \gamma B_0$$

The main magnetic field strength, B_0 , commonly ranges from 0.2 to 7 T. Higher strength fields result in higher image signal to noise ratio (SNR) but also result in reduced radiofrequency field (RF) homogeneity and increased specific absorption rate (SAR).

When the patient is MR imaged, a short RF pulse, tuned to the Larmor frequency, excites the spins of the precessing atoms out of the longitudinal state into the transverse plane, as shown in Figure 4.²³ The spins eventually return to equilibrium with B_0 at a rate that is dependent on the excited molecules. The return to the longitudinal state from the transverse plane is described with the relaxation parameters, R_1 and R_2 , which are described with more detail in Section 2.4.1. R_1 and R_2 are the reciprocals of T1 and T2 respectively.

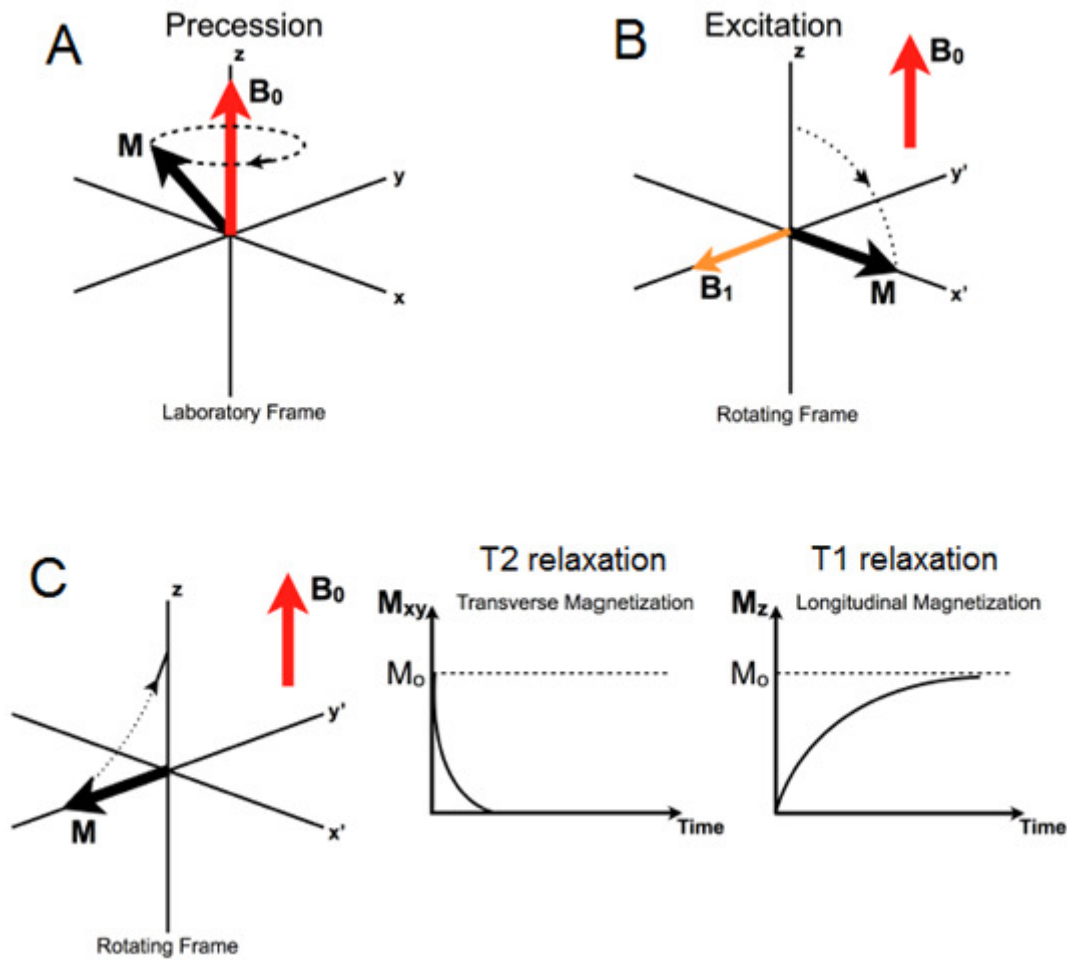


Figure 4: The precession, excitation, and relaxation of spins in MRI. The “laboratory frame” is the static reference frame of the MRI scanner with the z-axis oriented along the bore of the main magnetic. The rotation frame precesses about the z-axis of the laboratory frame at the Larmor frequency. A) The atoms of the imaged tissue precess around the magnetic field at the Larmor frequency. B) An excitation pulse of RF excites a slice of the tissue into the transverse plane. The net magnetization relaxes growing in the longitudinal direction, described by the parameter T1, and decaying away from the transverse plane as described by the parameter T2.

During the relaxation, the precessing nuclei emit RF that is received either by the large body coil that induced the excitation or by a smaller local coil for increased SNR. A gradient field varies during the imaging sequence to select different regions during excitation and read out to give the signal spatial information.

2.4.1. Relaxation Parameters

The magnitude of the signal emitted by the nuclei during an MRI sequence depends on the relationship between the relaxation parameters (T1 and T2) and the sequence parameters, repetition time (TR) and the echo time (TE). TR is the time between excitations and TE is the time between excitation and the start of signal acquisition. For T2-weighted imaging, a TR much longer than T1 is used to minimize the effect of T1, while a TE about as long as T2 is used to show differences in T2 decay. For T1-weighted imaging, a sequence with TR shorter than T1 is used so the longitudinal magnetization does not entirely recover before the next repetition, and a short TE is used to prevent T2 contrast. Sequences with long TR and short TE result in proton-density weighted images.

2.4.2. Contrast Agents

Exogenous contrast agents are used in MRI to give contrast to tissues or structures that would otherwise be difficult to visualize. The most widely used family of contrast agents are gadolinium based. Gadolinium has seven unpaired electrons, which results in it being strongly paramagnetic. The gadolinium atoms act as small magnetic field inhomogeneities, which decreases T1 and T2 relaxation times of protons around the molecule. At clinically used concentrations, about 0.1 mM, the decreased T1 is the predominant effect, resulting in gadolinium uptake appearing brighter in T1-weighted scans. At concentrations greater than 1 mM, the decreased T2 becomes the predominant effect on the image, and the gadolinium results in reduced MR signal. Gadolinium itself is toxic in elemental form, so it is chemically chelated to ligands, such as diethylene-triamine penta-acetic acid (DTPA), that reduce the biological toxicity. Due to the relatively high concentrations needed for MR contrast, gadolinium is generally used as a non-targeted imaging agent, taken up by brain lesions due to disruptions in

the blood brain barrier, or for perfusion and heart function imaging. The second family of MRI contrast agents is iron oxides, which will be detailed in Section 2.6. Iron oxides mainly reduce T2, so they are negative contrast agents in T2-weighted scans. They are FDA approved for the imaging of liver lesions.

2.5. Hybrid Imaging

Medical imaging techniques have a variety of advantages and disadvantages,⁸ and hybrid scanners and imaging probes have been developed combining multiple imaging modalities. With hybrid imaging, two or more imaging techniques are incorporated into a single scanner. Images from each modality are acquired either simultaneously or consecutively.²⁴ The resulting image data sets are co-registered, and in some cases, one image set is utilized in the reconstruction of the other.²⁵ A hybrid x-ray CT-fluorescence system has been developed, which not only gives the anatomical back drop from the CT scan, but also gives useful prior information for the reconstruction of the fluorescence molecular tomography.²⁶ Hybrid optical and MRI systems are being developed that similarly give anatomical detail and also identify the boundaries between tissues with different optical properties.²⁷ Hybrid nuclear medicine and optical scanners are used to simultaneously observe multiple molecular targets and bridge optical and radioactive imaging techniques.²⁸ Hybrid x-ray and MR imaging systems combining fluoroscopy and a vertical gap MR scanner have been used to assist with a number of patient interventions.²⁹ Photoacoustic tomography is a multi-modal imaging technology that uses laser light to cause thermal expansion in endogenous or externally administered chromophores. This expansion causes an ultrasonic pressure-wave that is received by an ultrasound transducer, and this signal can be co-registered onto an ultrasound image produced by the same system.³⁰

2.5.1. PET/CT

PET offers three-dimensional high sensitivity to imaging molecules that incorporate a positron emitting radionuclide, but has low spatial resolution and poor anatomical detail. To address the lack of anatomical information, a dual modality approach is commonly used, which pairs a PET scan with a computed tomography scan.^{31,32} CT scanners use kilo-voltage x-ray tubes to axially scan the patient with ionizing radiation and create a three-dimensional image based on each voxel's electron density and atomic number. By fusing the two scanners and the two images, one image is produced including both the molecular information of the PET image and the anatomical information of the CT image. MRI is a useful tool in evaluating pharmacodynamics and PET can be used to study pharmacodynamics and pharmacokinetics in clinical development of innovative therapeutics.^{33,34}

2.5.2. PET/MRI

Compared to CT, MRI offers better soft tissue contrast, more information, and no ionizing radiation dose. However, pairing it with PET has been difficult due to engineering challenges. Specifically, the magnetic field produced by a MRI scanner interferes with the movement of electrons within the photomultiplier tubes (PMTs) incorporated in a PET scanner. The development of avalanche photodiodes (APDs) to replace the PMTs lead to the creation of PET/MRI scanning systems.³⁵ These scanners integrate the PET scanner within the magnet of an MRI scanner, such that studies can be acquired simultaneously, rather than PET/CT scanners that have a back-to-back design for consecutive scans.³⁶

PET/MRI scanning systems, offer a number of advantages over PET/CT. The simultaneous acquisition of MR and PET images allows for faster imaging and higher patient through-put.

MRI allows for functional and metabolic imaging and better soft tissue contrast than CT.

Additionally MRI does not contribute to the ionizing radiation dose of the patient.³⁷

Interestingly, operating a PET scanner within the magnetic field of a MRI scanner has the additional benefit of shortening the mean free path of the positrons before annihilation, thereby increasing PET spatial resolution.³⁸ The strengths of combining PET and MRI, along with the development of the simultaneous PET/MRI scanner, has lead to its use in research and clinical molecular and neurological imaging.³⁹ Additionally, this combination of imaging modalities offers the opportunity to match the high sensitivity of PET with the high resolution of MRI in imaging probe detection. Hybrid PET/MRI systems have become increasingly utilized in clinical and pre-clinical research worldwide.

2.6. Superparamagnetic Iron Oxides

Superparamagnetic iron oxide (SPIO) contrast agents have been used clinically as MRI contrast agents for over a decade. They are strong enhancers of proton relaxation, but unlike gadolinium, they are superparamagnetic. Superparamagnetism occurs as the crystal-containing regions of unpaired spins are large enough they are thermodynamically independent, single domain particles. Each domain's net magnetic dipole is greater than that of its individual unpaired electrons. Without an external magnetic field (B_0), the magnetic domains rotate from thermal motion and orient randomly. When an external magnetic field is applied, the magnetic domains orient themselves with B_0 . Under these conditions, SPIOs mainly induce T2 relaxivity, and are used as negative contrast agents in T2-weighted images. SPIO contrast agents have a wide range of physico-chemical properties that are dependent on the design of the particles. Specifically, the size, charge, and coating of the particles affect their *in vivo* pharmacokinetics, and subsequently their application.⁴⁰ Clinically used SPIO contrast agents are composed of a number of

superparamagnetic iron oxide crystalline structures and a coating and material. The general formula of the crystalline structure $\text{Fe}_2^{3+}\text{O}_3\text{M}^{2+}\text{O}$, where M^{2+} is a divalent metal ion such as iron, manganese, nickel, cobalt, or magnesium.⁴¹ Each crystal is surrounded by the coating material, often composed of dextran or PEG-phospholipid amphiphilic molecules or dopamine-based derivatives that protects the nano-structure from the *in vivo* surrounding environment.

2.6.1. Applications

SPIO contrast agents range in size from about 15 nm up to 3.5 μm . Their size affects their usefulness in different medical imaging applications. The size of these particles is usually defined as hydrodynamic size as measured through dynamic light scattering. The largest SPIO agents range in size from 300 nm to 3.5 μm and are administered to patients orally to image the gastrointestinal lumen. Smaller SPIO agents (60-120 nm) are used as clinical molecular imaging probes. They are administered by either slow infusion or bolus injection. These agents are principally used for lesion detection in the liver and spleen. After intravenous administration, the SPIO agents are rapidly cleared from the blood and collected by the reticuloendothelial system (RES) cells of the liver and spleen. Lesions are generally without RES cells, including phagocytes, and do not phagocytose the SPIOs and appear unchanged in MR images. USPIO agents or “ultra-small” SPIOs are 20-40 nm in size are clinically used for metastatic lymph node detection and MR angiography (MRA). Unlike larger SPIOs, these agents are not cleared from the blood as quickly and offer increased contrast in MRA. Over time, they are collected by RES cells, including in lymph node monocytes and macrophages. Lymph nodes that have metastatic disease lose these RES cells and do not take up the SPIO agents.⁴² Superparamagnetic iron oxide contrast agents are also clinically used for bone marrow imaging and perfusion imaging of the brain, myocardium, kidney, and tumor vasculature.^{43,44} Mono-crystalline superparamagnetic

iron oxide nanoparticles (SPIONs) differ from other SPIO contrast agents in their monocrystallinity. With hydrodynamic sizes ranging from 2-20 nm, they are in the size range needed for target MR imaging. Each particle is composed of a maghemite ($\gamma\text{Fe}_2\text{O}_3$) or magnetite (Fe_3O_4) core and an organic coating. The maghemite crystal contains thousands of iron atoms and can generate MR signal contrast at concentrations orders of magnitude lower than conventional gadolinium chelates.⁴⁵

2.6.2. Mono-Crystalline Superparamagnetic Nanoparticles

While SPIONs are not widely used in the clinic, their strong change in signal intensity, biodegradable iron composition, straightforward surface chemistry, and flexible magnetic properties make them popular for target MR imaging probe research.⁴⁶ SPIONs have been used *in vivo* to image HER2/neu expression in NIH3T6.7 xenographic tumors by binding herceptin to the MION surface and to image angiogenesis through $\alpha_v\beta_3$ integrin expression in BT-20 xenographic tumors by binding arginine-glycine-aspartate peptides to the SPION surface.⁴⁷ By incubating SPIONs with ^{59}Fe with in organic solvents, SPIONs have been labeled with a gamma emitting radionuclide for bimodal detection.⁴⁸ Recently, cRGD targeted SPIONs extrinsically labeled with DOTA- ^{64}Cu were used to PET and MR image tumor integrin expression *in vivo*.⁴⁹ This nano-platform has additionally been conjugated with doxorubicin using a pH-sensitive hydrazone bond to achieve pH-responsive drug release.⁵⁰ Tumor targeted SPIONs have been used in a short external alternating magnetic field to produce heat and deliver hyperthermia treatment to tumor bearing mice.⁵¹ SPIONs are becoming utilized for “cancer nanotheranostics,” which is a strategy that simultaneous images and treats cancer cells through the application of nanoparticles.⁵² While SPIONs have been utilized in this multitude of applications, the synthesis of these nanoparticles with ideal characteristics for *in vivo* imaging is still developing. SPIONs

are promising tools in cancer imaging, drug delivery, and therapy. Their MR contrast and multifunctional potential highlight their potential in molecular imaging and cancer treatment.^{53,54}

2.6.3. Synthetic Strategies

SPIO production is achieved through three main families of chemical synthesis: chemical precipitation, reactions in constrained environments, and high temperature methods.⁵⁵ Chemical precipitation is the simplest and most well established method, where the SPIONs are created by co-precipitation of a mixture of ferrous and ferric salts.⁵⁶ This reaction is achieved in an aqueous base and can be written as:



During synthesis, the iron ions can become oxidized before they precipitate. This effect can be reduced, but not prevented, by precipitating under nitrogen protection. This results in the simultaneous production of magnetite and maghemite nano-particles.



Maghemite crystals exhibit lower mass magnetization than magnetite and are difficult to separate. The size of the crystals can be manipulated by controlling the reaction pH, ionic strength, temperature, nature of salts, and $\text{Fe}^{3+}/\text{Fe}^{2+}$ ratio.⁵⁷ The creation of crystal seeds simultaneous with crystal growth leads to disperse crystal size distribution. Chemical precipitation is depicted in Figure 5.

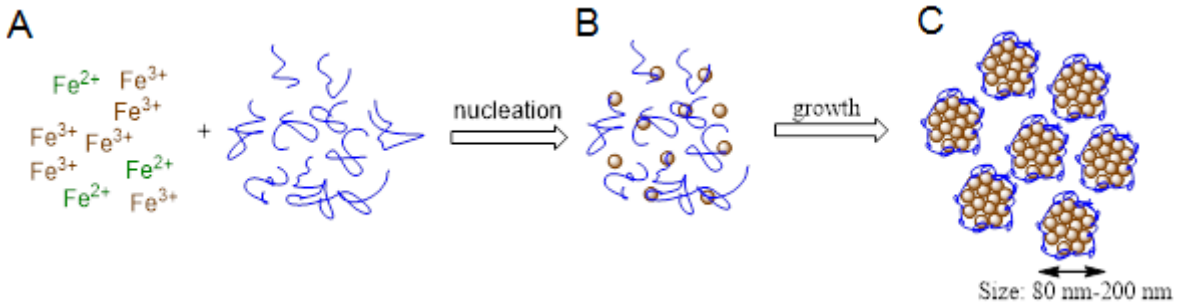


Figure 5: Chemical precipitation synthesis of SPIOs. A) Ferrous and ferric salts are dissolved aequously in the presence of carbohydrates, such as dextran. B) Iron oxide crystals form during nucleation. C) The iron oxide crystals aggregate and are coated by the carbohydrates to form SPIOs.

Reactions in constrained environments use structures to separate crystal growth from crystal seed creation. These structures include water-swollen reversed micellar structures in nonpolar solvents, apoferritin protein cages, dendrimers, cyclodextrins, and phospholipid membranes that form vesicles with iron oxide nanoparticles serving as solid supports.²³ Reversed micelles are good examples of how these structures are used to control iron oxide crystal size. These micelles are formed by amphiphiles. Amphiphiles are lipids that have both hydrophilic and hydrophobic parts. These amphiphiles form colloidal micelles when in an aqueous environment. In micelle-forming lipids, the hydrophobic chains are oriented inward and the hydrophilic chains outward. Reverse micelles are similar, but have the hydrophilic chains oriented inward and the hydrophobic chains oriented outward. They solubilize water in non-polar media and form micro-environments correct for SPION formation.⁵⁸ The reverse micelles restrict the amount of iron salts available for crystal formation. The size of the nanoparticles is controlled by the interplay between the lipid chain length and concentration, and solution pH and temperature. Other strategies employ other structures that separate crystal formation and crystal growth. In general, while these methods create more monodisperse crystal distribution, the reaction yield is reduced and the synthesis is not easily scaled up for industrial nano-particle production.

High temperature methods decompose iron complexes, such as $\text{Fe}(\text{Cup})_3$, $\text{Fe}(\text{CO})_5$, or $\text{Fe}(\text{acac})_3$, in the presence of surfactants and organic solvents. At these high temperatures the nature of the solvents results in the formation of crystal seeds that grow the longer the solution is heated.⁵⁹ These nanoparticles have a high level of monodispersity and size control. Maghemite crystals were obtained by thermal decomposition of iron pentacarbonyl at 100 °C in oleic acid and then increasing the temperature of the iron oleic complex to 300 °.⁶⁰ Magnetite nanoparticles are created through the high-temperature reaction of iron(III) acetylacetonate with 1,2-hexadecanediol in oleic acid and oleylamine. These particles are hydrophobic and have diameters that can be tuned from 4 to 20 nm by modifying the ratio between oleic acid and oleylamine and the reaction temperature.²⁸

Chapter 3

3. Hybrid PET/MR Nanoparticle Synthesis

To develop the synthetic process for the final hybrid PET/MRI nanoparticle, a number of steps were taken to synthesize similar nanoparticles that were useful in investigating the chemical process and SPION's behavior *in vivo*. Specifically, non-radioactive nanoparticles were produced to develop the chemistry of synthesis. Then, ^{59}Fe was incorporated, as a surrogate for ^{52}Fe , to develop the chemical process of incorporation. Later, the 44.5 day half-life, allowed these ^{59}Fe -SPIONs to be used for *in vitro* cell viability and uptake assays, and for *in vivo* biodistribution. To enable the incorporation of manganese PET radionuclides, MnFe_2O_4 nanoparticles were developed. Finally, with the radionuclide and manganese incorporation chemistry established, the ^{52}Mn -MIONs were synthesized.

3.1. [^{59}Fe]-SPION Synthesis

The synthetic method of radionuclide incorporation was developed first by producing natural iron-oxide nanoparticle by previously established high temperature thermal decomposition synthesis. Then a novel method for radio-intrinsic SPIONs was developed using ^{59}Fe .

3.1.1. Natural iron-oxide nanoparticle synthesis

Synthesis of non-radioactive natural SPIONs was accomplished through high temperature thermal decomposition synthesis of maghemite crystals developed by Sun and Zeng. This process is detailed below:

- (1) Combine iron(III) acetylacetonate [Fe(acac)₃] (140 mg), (Z)-Octa-9-decenylamine [oleylamine] (395 μL), (9Z)-Octadec-9-enoic acid [Oleic acid] (380 μL), and 1,2-hexadecanediol (517 mg), at a molar ratio of 1:3:3:5. Dissolve the mixture in 10 ml benzyl ether for each millimole of Fe(acac)₃.
- (2) Mix the reagents in a 50 mL three-neck flask under argon protection.
- (3) Heat the reaction solution to 200°C in 30 minutes and maintain this temperature for two hours.
- (4) Increase the temperature to 300°C in 30 minutes and maintain this temperature for one hour.
- (5) Cool the solution down to room temperature and add 50 mL of ethanol to precipitate the nanoparticles.
- (6) Centrifuge at 3100 g rcf for 5 minutes. Remove the supernatant containing the non-nanoparticle agents, suspend the nanoparticles in chloroform, and filter the nanoparticles solution by 0.22 μm nylon filter.

This synthesis produces mono-crystalline nanoparticles coated with oleic acid and oleylamine and is useful for this project because the total reaction time is short enough to be appropriate for the incorporation short half-lived imaging radionuclides.

Next, the reaction was scaled down as much as possible, so that smaller quantities of radionuclides can be used in future productions, while having a useful ratio of radioisotopes to stable isotopes. The reaction starting reagent masses were reduced down to the point where 0.4 millimoles (140 mg) of Fe(acac)₃ is used while maintaining the same molar ratios of the other reagents. The use of smaller masses of reagents caused poor control of the reaction, which was reflected by fluctuation of reaction temperature and worse magnetization of nanoparticles.

3.1.2. ⁵⁹Fe incorporation

The method to incorporate a radionuclide into the crystal structure of the SPION was developed using commercially purchased ⁵⁹Fe that comes as an 59-iron(III) chloride in a aqueous solution of HCl. The first strategy used was to use between 5 and 300 μCi of 59-iron(III) chloride and mix it with the non-radioactive Fe(acac)₃ before thermal decomposition reaction. This yielded SPIONs with similar size as the non-radioactive synthesis. The incorporation efficiently of the

^{59}Fe was ~90%, with the unincorporated ^{59}Fe being separated in step (6) of the synthesis into the supernatant.

A second strategy was developed to achieve nanoparticles with higher ^{59}Fe to natural iron ratios. This strategy begins with non-radioactive iron oxide cores and constructs an iron oxide shell around the core that incorporates the radionuclide. This is accomplished as detailed below:

- (1) Dry between 5 and 300 μCi of $^{59}\text{FeCl}_3$ by heating the solution under vacuum to remove all water and HCl.
- (2) Add 20 mg $\text{Fe}(\text{acac})_3$, 517 mg 1,2-hexadecanediol, 150 μL oleylamine, 150 μL oleic acid, and 4 mL benzyl ether to the dried ^{59}Fe in a 25 mL flask.
- (3) Add 12 mg (Fe) of the non-radioactive nanoparticles coated with oleic acid and oleylamine, suspended in chloroform to the 50 mL flask. Heat the reaction mixture under vacuum to remove the chloroform.
- (4) Mix this suspension and protect it from oxygen with argon gas flow.
- (5) Heat the reaction mixture in 30 minutes to 200°C and keep at this temperature one hour.
- (6) Increase the reaction temperature in 30 minutes to 300°C and keep this temperature for 1 hour.

This “thermal cycling” grows the iron oxide nanoparticles with a shell that incorporates ^{59}Fe with an efficiency ranging from 80% to 95% and increases the nanostructure size observed in TEM (see Section 3.5). Also, the mass of natural iron used in the final reaction is reduced, to achieve a higher ^{59}Fe to natural iron ratio.

3.2. [^{52}Mn]-MION synthesis

To achieve a hybrid PET/MRI nanoparticle, a positron emitting radionuclide must be utilized. A viable candidate is ^{52}Fe , which has positron emission ($\beta^+ = 55\%$) and a half-life ($t_{1/2} = 8.275$ h) long enough to be used in the thermal decomposition method previously developed in Section 3.1. This radionuclide was not utilized, because the small hospital based cyclotron available for this project is only commissioned for 12.9 MeV proton irradiation, and the proton energy needed to achieve the $^{55}\text{Mn}(p,4n)^{52}\text{Fe}$ is 54 MeV.⁶¹ Instead, manganese iron oxide nanoparticles

(MIONs) were synthesized, as previously described by Yang.⁶² Into these nanoparticles, we incorporated ⁵²Mn, which is a positron emission radionuclide ($\beta^+ = 29.6\%$) with a moderate half-life ($t_{1/2} = 5.591$ days). Additionally, ⁵²Mn can be produced through the available 12.9 MeV proton irradiation of natural chromium, as described in Section 3.2.3.

3.2.1. Natural Manganese Iron Oxide Nanoparticle Synthesis

Within the crystalline structure of the SPION, a number of divalent elements can be doped. Natural manganese was incorporated into the nanoparticle for the purpose of developing the chemical synthesis for the incorporation of positron emitting radionuclides of manganese. The chemical method for manganese iron oxide nanoparticle is similar to the non-doped synthesis (Section 1.1.1), except one third of the iron atoms are replaced with manganese atoms. This process was developed with natural manganese and is described below:

- (1) Combine 0.27 mmole (94 mg) of Fe(acac)₃, 0.13 mmole (47 mg) tris(acetylacetonato)manganese(III) [Mn(acac)₃], 2 mmole (517 mg) 1,2-hexadecanediol, 4 mL benzyl ether, 1.2 mmole (395 μ L) oleylamine, and 1.2 mmole (380 μ L) oleic acid in a 50 mL three-necked flask.
- (2) Mix the reagents under argon protection.
- (3) Heat the solution to 200°C in 30 minutes and keep this temperature for two hours.
- (4) Increase the temperature to 300°C in 30 minutes and keep this temperature for one hour.
- (5) Cool the solution down to room temperature and add 50 mL of ethanol to precipitate the nanoparticles.
- (6) Centrifuge at 3100 g ref for 5 minutes. Remove the supernatant containing the non-nanoparticle agents and suspend the nanoparticles in chloroform.

3.2.2. Core/shell synthesis of MIONs

A core/shell structure synthesis incorporating natural manganese was developed to simulate the future incorporation of a PET manganese radionuclide. This core/shell strategy was similar to the ⁵⁹Fe incorporation strategy described in Section 1.1.2, but natural manganese(II) chloride (MnCl₂) replaces the 59-Iron(II) chloride and Mn(acac)₃ replaces one third of the Fe(acac)₃:

- (1) Dry .0285 mmoles (2 mg) of MnCl_2 by heating the solution under vacuum.
- (2) Add the MnCl_2 to 12 mg (Fe) of the manganese doped non-radioactive nanoparticles coated with oleic acid and oleylamine, suspended in chloroform, in a three-necked flask. Heat the reagents under vacuum to remove the chloroform.
- (3) Add 20 mg $\text{Fe}(\text{acac})_3$, 2 mmole (517 mg) 1,2-hexadecanediol, 150 μL oleylamine, 150 μL oleic acid, and 4 mL benzyl ether to the manganese/iron-oxide cores in a 50 mL flask.
- (4) Mix this suspension and protect it from oxygen with argon gas flow.
- (5) Heated over 30 minutes to 200°C and hold at this temperature one hour.
- (6) Increase the reaction temperature over 30 minutes to 300°C and hold this temperature for 1 hour.

Similar to the ^{59}Fe incorporation described in Section 1.1.2, this “thermal cycling” increases the nanostructure size observed in TEM (see Section 3.5.3).

3.2.3. ^{52}Mn cyclotron production

The production of ^{52}Mn was accomplished through 12.9 MeV proton irradiation of natural chromium to achieve the $^{52}\text{Cr}(\text{p},\text{n})^{52}\text{Mn}$ reaction. A 99.995% purity natural chromium foil with 0.25 mm thickness was purchased from Trace Sciences International Corporation. This thickness was selected because it corresponds to the 12.9 – 7.8 MeV energy window, as shown in, Figure 6, which shows the energy a 12.9 MeV proton beam as it transverses chromium, based on chromium’s stopping power for protons.⁶³

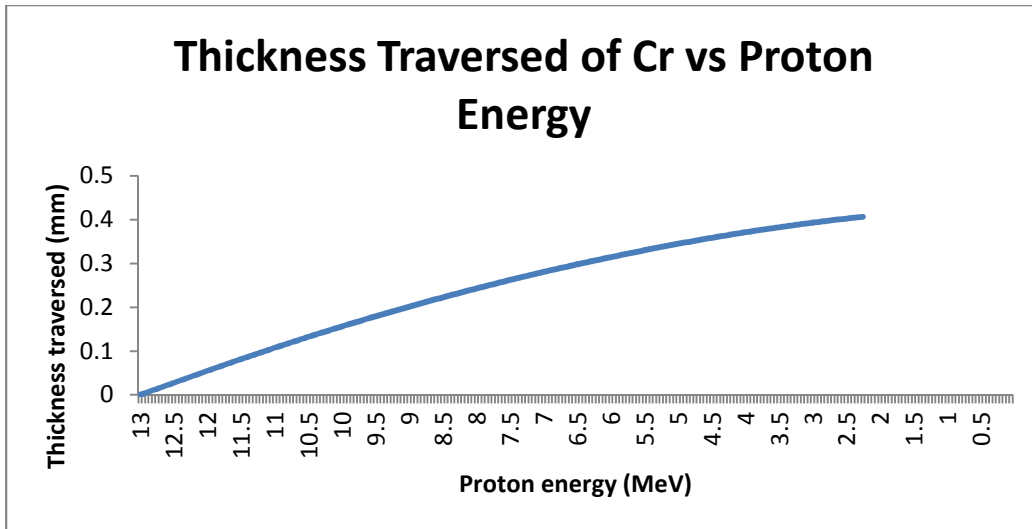


Figure 6: As the proton beam transverses the chromium target, it loses energy based on the stopping power of the chromium. This figure depicts the kinetic energy remaining in a 12.9 MeV proton beam as it travels through chromium.

Circular targets were formed from the foil with a 5.5 mm radius. Each target weighed 120 ± 11 mg. Foils were loaded into an iridium holder and secured with a steel clip, as shown in Figure 7. The initial cyclotron irradiation used an integral charge of $10 \mu\text{Ah}$. Follow up irradiations used greater integral charges, up to $240 \mu\text{Ah}$. Based on six separate irradiations, the yield was $108 \pm 9 \mu\text{Ci}/\mu\text{Ah}$. This is 20% less than the theoretical yield predicted by the $^{52}\text{Cr}(p,n)^{52}\text{Mn}$ excitation function.⁶⁴ This discrepancy is likely a result of a portion of the proton beam being blocked from the foil by the steel clip or missing the foil and being absorbed by the holder.



Figure 7: The target assembly used to support the chromium in the cyclotron beam. The chromium foil target (center) is held to the iridium holder (outside) by a steel clip (middle) during the irradiation.

Gamma energy spectrums of the irradiated foil were acquired with a high purity Ge gamma spectrometer (Ortec, Oak Ridge, TN), calibrated with a ^{152}Eu source. A representative gamma energy spectrum is shown in Figure 8. The detector background was acquired separately and subtracted from the acquired spectrum. ^{52}Mn is apparent from its multiple emissions and ^{54}Mn is detected by its 834.91 keV gamma emission. The ^{54}Mn ($t_{1/2} = 312$ d) is a byproduct of irradiating natural chromium, which contains ^{54}Cr , allowing the $^{54}\text{Cr}(p,n)^{54}\text{Mn}$ reaction. The ^{54}Mn accounts for $0.5 \pm 0.1\%$, as determined through gamma energy spectroscopy. Notably absent is a 320.1 keV photon peak, which is characteristic of ^{51}Cr , indicating that radionuclide has not been produced in detectable quantities.

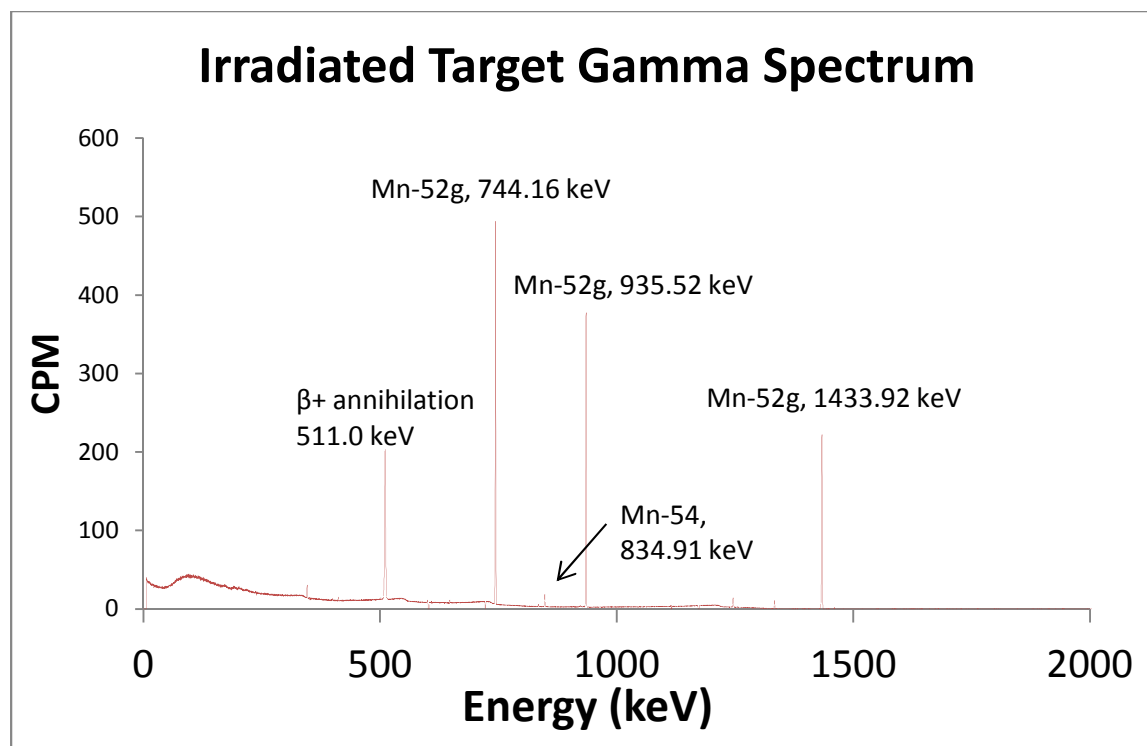


Figure 8: The gamma energy spectrum of a natural chromium foil after 12.9 MeV proton irradiation. The principle emissions of ^{52}Mn and ^{54}Mn are labeled. Additionally, the 511 keV peak associated with β^+ annihilation photons is labeled. Also visible is the 346 keV peak of ^{52}Mn .

3.2.4. ^{52}Mn radiochemical extraction

In order to incorporate the small mass of ^{52}Mn produced into our nanoparticles, the ^{52}Mn needed to be purified and isolated from the bulk chromium and other metals. Initially, an anion exchange method was developed for the chemical separation, but this method proved unsuitable for separating manganese from chromium. Instead, a liquid-liquid extraction was developed to isolate the manganese radionuclides. The extraction is depicted in Figure 9 and Figure 10. This method was previously developed by Lahiri and is detailed below.⁶⁵

- (1) Add the irradiated foil to 2 mL of 12 N HCl solution in a 25 mL glass flask.
- (2) Add 300 μL of 30% hydrogen peroxide solution and heat until the foil is totally dissolved and the solution is near dryness.
- (3) Add 2 mL of 12 N HCl solution and transfer the solution to a glass extraction tube.
- (4) Add 1 mL of 0.8 M trioctylamine (TOA) diluted in n-hexane. Vortex the organic liquid/aqueous liquid mixture.

- (5) Allow the aqueous phase to separate from the organic phase. The manganese radionuclides will transfer to the organic phase by forming a complex with TOA, while the chromium will stay in the aqueous solution. Remove the organic phase.
- (6) Repeat steps 4 and 5 until ~95% of the activity has been extracted. This requires 4-6 repeats.
- (7) Re-extract the manganese radionuclides from the organic phase by adding 0.001 M NH_4OH (ammonium hydroxide) aqueous solution to the organic phase and vortexing.
- (8) The activity will transfer to the re-extraction aqueous phase. Repeat step 7 until ~95% of the activity is in the re-extraction aqueous solution. This will take 2-3 repeats.
- (9) Heat the re-extraction solution until it is near dryness. Re-dissolve the manganese radionuclides in 0.05 M HCl solution.

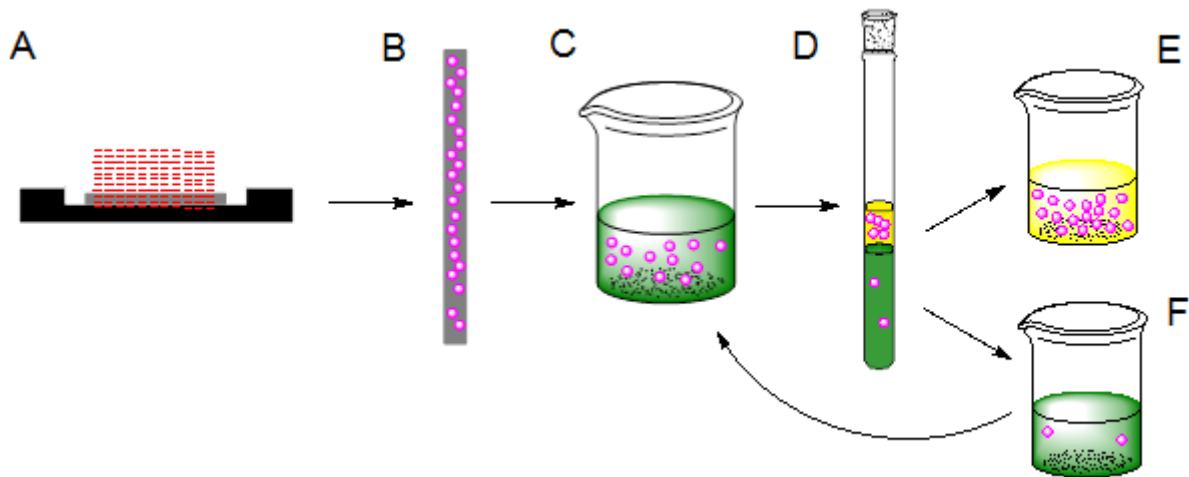


Figure 9: Radiochemical extraction of ^{52}Mn . A) The chromium foil (gray) is loaded into an iridium holder (black) and irradiated with 12.9 MeV protons (red). B) ^{52}Mn atoms (pink) are produced throughout the foil, which is unloaded from the holder. C) The foil is then dissolved in 12 N hydrochloric acid and hydrogen peroxide while heating. The chromium (green) and manganese (pink) are dispersed throughout the solution. D) The aqueous solution is mixed with the organic phase (yellow), trioctylamine diluted in n-hexane. The aqueous phase then separates from the organic phase, with the majority of the manganese in the organic phase and the chromium in the aqueous phase. E) The organic phase (yellow) is collected for re-extraction of the ^{52}Mn from the organic phase. F) The aqueous phase (green) still contains a portion of the ^{52}Mn (pink) and can be further extracted.

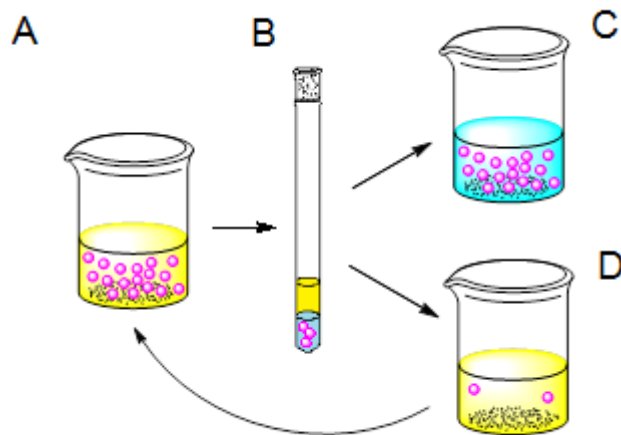


Figure 10: Re-extraction of ^{52}Mn from the organic phase produced from the extraction of manganese isotopes from the chromium isotopes. A) ^{52}Mn (pink) is dissolved in trioctylamine diluted in n-hexane (yellow) as a result of the initial extraction. B) Ammonium hydroxide aqueous solution (blue) is added to the organic phase and vortexed. The ^{52}Mn (pink) transfers to the aqueous phase. C) The aqueous phase (blue) containing the ^{52}Mn (pink) is collected for future utilization in MION synthesis. D) The aqueous phase is further re-extracted to collect any remaining ^{52}Mn .

The entire extraction process was $91\pm 6\%$ efficient. In order to obtain higher purity ^{52}Mn , the extraction was repeated. This further removed the bulk chromium from the final solution.

Inductively coupled plasma mass spectrometry (ICP-MS) was utilized to quantify the specific activity and chromium contamination. The initial specific activity was 108 ± 4 $\mu\text{Ci}/\text{ng}$ of Mn with a 10.4 ± 0.4 $\mu\text{Ci}/\text{ng}$ chromium contamination. This indicates that the repeated extraction removed 99.4% of the chromium. The gamma energy spectrum of the extracted ^{52}Mn solution was acquired and is shown in Figure 11. The spectrum is similar to the un-extracted foil, because the only non- ^{52}Mn radionuclide that contributes to the spectrum is ^{54}Mn , which cannot be chemically separated from all of the other manganese radionuclides.

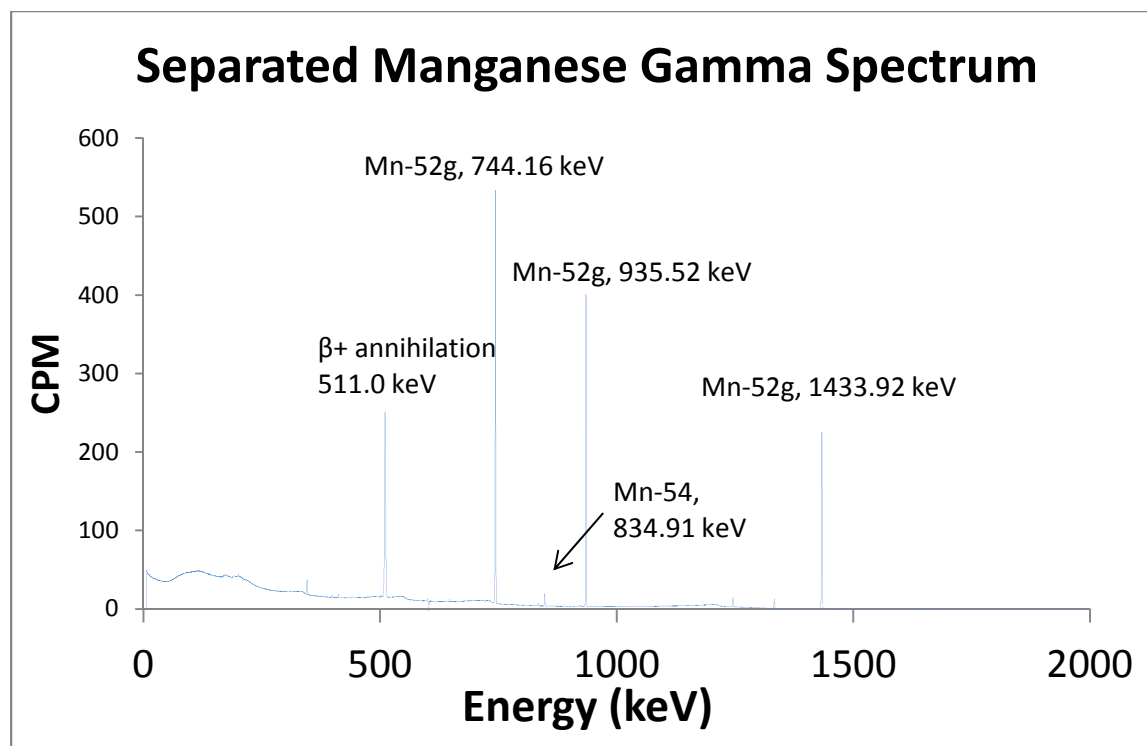


Figure 11: The gamma energy spectrum of the separated manganese radionuclides is similar to that of the irradiated foil. That is because the only major contributor to the spectrum aside from ^{52}Mn is ^{54}Mn , which cannot be chemically separated from the other manganese radionuclides.

3.2.5. ^{52}Mn incorporation

To incorporate the ^{52}Mn into the MIONs, initially a similar method to the ^{59}Fe incorporation was utilized, with the ^{52}Mn being incorporated into the shell of MION synthesis described in Section 3.2.2. The ^{52}Mn solution was dried and added to the three-necked flask before the other reagents were added and then heated. This approach produced [^{52}Mn]-MIONs with a wide range of incorporation efficiencies, from 10-70%. This synthetic strategy was not reproducible, therefore, the core/shell synthesis strategy, described in Section 3.2.2, was not utilized for further [^{52}Mn]-MION productions. Instead, ^{52}Mn incorporation was achieved by drying the ^{52}Mn solution produced during the ^{52}Mn radiochemical separation in a three-necked flask and then attending the reagents for a normal MION production as described in Section 3.2.1. This process is depicted in Figure 12 and described below:

- (1) Dry between 50 μCi and 14 mCi of $^{52}\text{MnCl}_2$ by heating the solution in a 50 mL three-necked flask under vacuum to remove all water and HCl.
- (2) Add 0.27 mmole (94 mg) of $\text{Fe}(\text{acac})_3$, 0.13 mmole (47 mg) tris(acetylacetonato)manganese(III) [$\text{Mn}(\text{acac})_3$], 2 mmole (517 mg) 1,2-hexadecanediol, 4 mL benzyl ether, 1.2 mmole (395 μL) oleylamine, and 1.2 mmole (380 μL) oleic acid in a 50 mL three-necked flask.
- (3) Mix the reagents under argon protection.
- (4) Heat the solution to 200°C in 30 minutes and keep this temperature for two hours.
- (5) Increase the temperature to 300°C in 30 minutes and keep this temperature for one hour.
- (6) Cool the solution down to room temperature and add 50 mL of ethanol to precipitate the nanoparticles.
- (7) Centrifuge at 3100 g rcf for 5 minutes. Remove the supernatant containing the non-nanoparticle agents, suspend the nanoparticles in chloroform, and filter the nanoparticles solution with a 0.22 μm nylon filter.

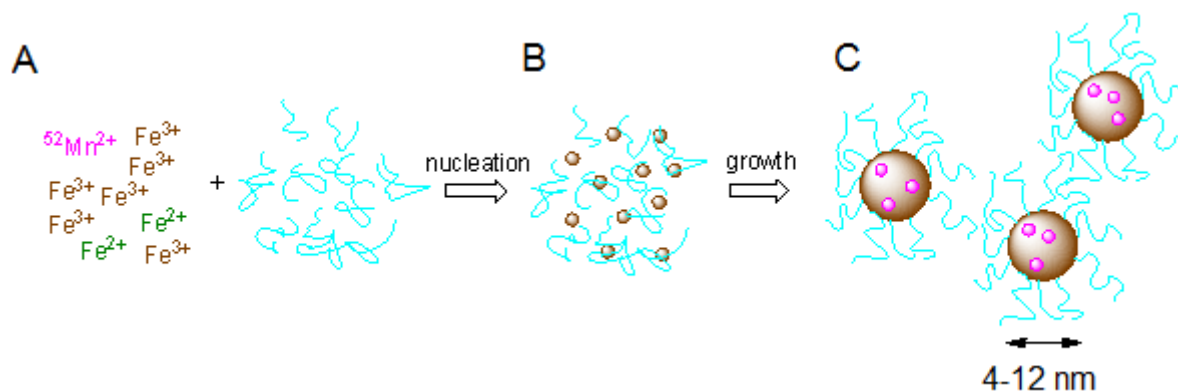


Figure 12: Incorporation of ^{52}Mn into the MION. A) $^{52}\text{Mn}^{2+}$, natural Mn^{2+} , and $\text{Fe}^{3+/2+}$, are combined and heated to 200°C with oleic acid and oleylamine. B) Manganese iron oxide nanoparticle seeds form. C) The seeds grow into larger crystals incorporating ^{52}Mn throughout and coated with oleic acid and oleylamine.

3.3. Modification of Nanoparticles with Polymer Coating

In order to make the hydrophobic oleic acid/oleylamine coated iron oxide nanoparticles water soluble, bio-compatible, and multi-functional, a multidentate poly-ethylene-glycol ligand was developed. This ligand, shown in Figure 16, is composed of dopamine, poly-acrylic acid (PAA-1800 MW), and poly-ethylene glycol (PEG-2000 MW). The dopamine is not incorporated for targeting. Instead, its two hydroxyl groups allow it to displace the oleic acid and oleylamine on the SPION and anchor the ligand to the surface of the nanoparticle through dipolar binding. The repeating PAA unit acts as the molecular skeleton of the ligand, while the PEG-2000 confers

water solubility, biocompatibility, and favorable pharmacokinetics to the SPION. From previous studies, the multi-dentate ligands, have stronger interactions with nanoparticles for greater stability *in vitro* and *in vivo*. The synthetic process for of PAA-Dopamine-PEG ligands is described below:

- (1) Dissolve 5.56 μ moles of PAA (100 mg) in 3 mL of dimethyl sulfoxide (DMSO).
- (2) Add 2 mmoles (319 mg) 1-ethyl-3-(3-dimethylaminopropyl)carbodiimide (EDC) and 1.7 mmols (192 mg) N-Hydroxysuccinimide (NHS) while stirring. Continue stirring for 4 hours at room temperature.
- (3) Add 0.86 mmole (132 mg) dopamine hydrochloride and 0.7 mmole (1400 mg) N-terminal amino group poly-ethylene-glycol (amino-PEG-2000) to the activated PAA solution and stir at room temperature for 16 hours.
- (4) Dialysis the solution with a 2,000 MW cutoff cassette to remove the unreacted molecules. Dry the product under vacuum and dissolve the ligands in deionized water.

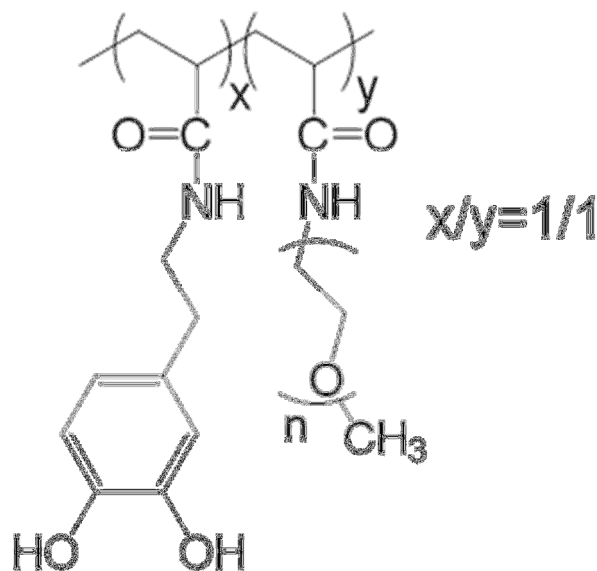


Figure 13: Multidentate poly-ethylene-glycol ligand for coating the SPIONs. It is composed of dopamine on the bottom left, which non-covalently binds to the surface of the SPION, a repeating poly-acrylic acid (PAA-1800 MW) chain on the top, which is the back bone of the molecule, and a repeating poly-ethylene glycol (PEG-2000 MW) that provides biocompatibility and water solubility.

A number of other ligands were developed with different PEG chain lengths (550 and 2000 MW). SPIONs coated with these ligands suffered reduced water solubility. Sodium dodecyl sulfate (SDS) was initially used during ligand exchange to increase these SPIONs' water solubility and allow for relaxometry measurements, but it was later discovered that the dodecyl sulfate could not be separated from the nanoparticles after ligand exchange. This reduced the nanoparticles' biocompatibility and the use of dodecyl sulfate was discontinued. Other ligands

were developed that either partially or completely replaced the PEG chains with sulfobetaine to create zwitterionic (containing both positive and negative charge) ligands. Without the use of dodecyl sulfate, these nanoparticles also suffered from reduced water solubility, in addition to possible aggregation and precipitation.

3.3.1. Ligand exchange reaction

The dopamine incorporate in the multidentate poly-ethylene-glycol ligand replaces the hydrophobic oleic acid/oleylamine coating on the iron oxide nanoparticles after a ligand exchange reaction. After this reaction, the nanoparticles are separated from the oleic acid/oleylamine through centrifugation. This process is below:

- (1) Mix 6 nmoles of oleic acid/oleylamine coated SPIONs suspended in chloroform (2 mL) with an excess of multidentate poly-ethylene-glycol ligand (5 mmoles) dissolved in deionized water (0.5 mL).
- (2) Stir the mixture rigorously and heat to 60 °C for 30 minutes.
- (3) Precipitate the PAA-Dopamine-PEG coated SPIONs by adding hexane.
- (4) Centrifuge the SPIONs at 824 rcf for 5 minutes.
- (5) Collect and dry the pellet containing the SPIONs. Then re-suspend them in deionized water.
- (6) Filter the suspension with a 0.22 µm nylon filter.
- (7) Then centrifuge again through a 30,000 MW cut off filter (Amicon filters) at 9,100 rcf for 30 minutes to remove un-bound ligands and concentrate the SPION solution.

3.3.2. Alternative coating strategy

An alternative strategy for coating the superparamagnetic nanoparticles was developed from previously reported methods.⁶⁶ The purpose of developing the alternative strategy was to directly compare the physical characteristics and *in vitro* uptake of an established coating with our novel coating approach. The protocol for this strategy is detailed below:

- (1) 0.5 g of dopamine and 0.4 g of sodium nitrite was dissolved in 6 mL of DI water and cooled to 0 °C.
- (2) Sulfuric acid (3.1 mmol in 2 mL of water) was added drop wise.

- (3) This solution was stirred overnight, filtered with a 45 μm Millipore filter, and dried under vacuum to yield 270 μg nitrodopamine (NDA). This is a 43% reaction yield.
- (4) The chemical structure of NDA was confirmed by NMR.
- (5) A CHCl_3 (3 mL) solution containing 7 mg of hydrophobic SPION was mixed dropwise over 5 minutes while stirring with 2 mL of DMSO containing 10 mg of NDA.
- (6) After overnight reaction, the nanoparticles were separated by centrifuge (4180 rcf for 10 minutes), washed with water twice, and filtered with a 30 kDa molecular weight cutoff filter.
- (7) $\text{CH}_3\text{O-PEG}_{2000\text{MW-NHS}}$ was synthesized from $\text{CH}_3\text{O-PEG}_{2000\text{MW-NH}_2}$, as shown in Figure 14, by first reacting 1.0 g of $\text{CH}_3\text{O-PEG}_{2000\text{MW-NH}_2}$ with 75 mg of succinic anhydride dissolved in 10 mL of chloroform. 4-Dimethylaminopyridine (6 mg) was included as a catalyst. This product was then separated by silica gel chromatography, eluted with 4:1 chloroform to methanol solution. The product (30 mg) was then reacted with 14.2 mg of (EDC) and 8.6 mg of (NHS) in 1 mL of DMSO. This yielded 470 mg of $\text{CH}_3\text{O-PEG}_{2000\text{MW-NH}_2}$, which was not further purified.
- (8) The NDA coated nanoparticles were then PEGylated as shown in Figure 15. $\text{CH}_3\text{O-PEG}_{2000\text{MW-NH}_2}$ (28 mg) was added to 2 mL DMSO containing 7 mg of NDA coated SPION under N_2 atmosphere. The mixture was bubbled with N_2 for 30 minutes and allowed to react for 5 hours. The SPIONs were then filtered with a 30 kDa molecular weight cutoff filter.

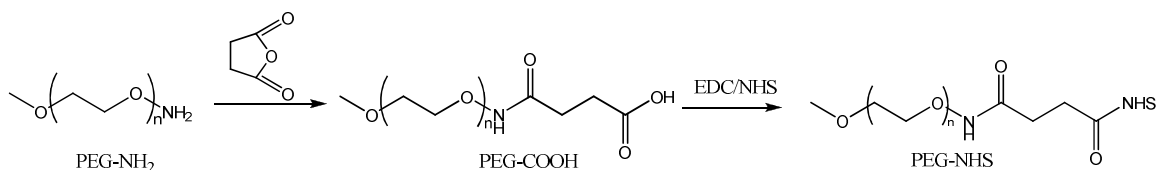


Figure 14: Synthetic scheme to produce $\text{CH}_3\text{O-PEG}_{2000\text{MW-NH}_2}$. This ligand is then used to coat the nanoparticle.

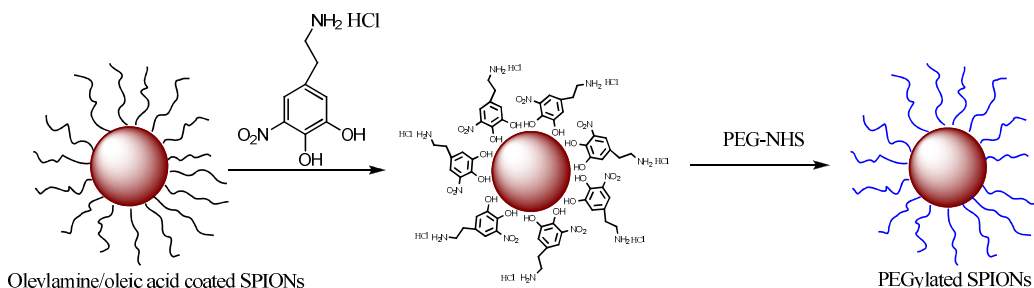


Figure 15: Alternative coating strategy schematic. The oleylamine and oleic acid is first replaced with NDA on the surface of the nanoparticles. Then, the $\text{CH}_3\text{O-PEG}_{2000\text{MW-NH}_2}$ is added to react with the NDA and PEGylate the nanoparticles.

3.3.3. Synthesis of coating ligand for bio-conjugation

For further conjugation to targeting moieties, the multidentate poly-ethylene-glycol ligand was modified to incorporate PEG chains that included a terminal amine (NH_2). These “amino-PEG”

chains were included in the ligand synthesis in a 2:1:1 ratio with the dopamine and unreactive PEG chain, as shown in Figure 16. The number of reactive amine group in each polymer ligand will be ~6-7 based on the molecular design. Considering each SPION will be coated tens of to hundreds of ligands, the total number of reactive amine on each nanoparticles will be several hundreds, which is enough to conjugate large amount targeting molecules. This synthesis is similar to the method described in Section 3.3, with the exception that in step 3, only 700 mg diamino-PEG is used and 700 mg of amino-PEG-OCH₃ is also included.

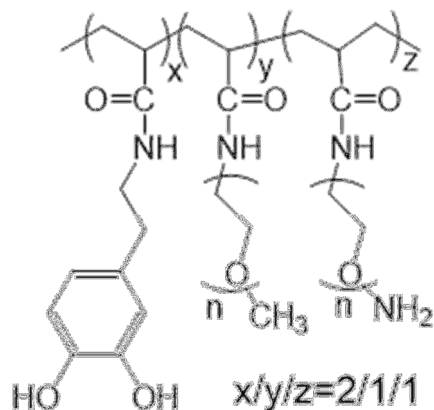


Figure 16 Multidentate amino-PEG ligand for coating the SPIONs and bio-conjugation. It is composed of dopamine on the bottom left, which non-covalently binds to the surface of the SPION, a repeating poly-acrylic acid (PAA-1800 MW) chain on the top, which is the back bone of the molecule, and repeating poly-ethylene glycol (PEG-2000 MW), half of which include a terminal amine group for bio-conjugation reactions.

3.3.4. Bio-conjugation reaction

After the synthesis of amino-PEG, the SPIONs are coated as described in Section 3.3.1. The resulting “amino-SPIONs” is then suspended in phosphate buffered saline (PBS) and conjugated with cRGD as described below. A schematic of the reaction and the two strategies is shown in the figure below.

- (1) Amino-SPION (0.9 nmole) in PBS was transferred to a 10 mL vial.
- (2) An over-excess of bis(sulfosuccinimidyl) suberate (26 μg) was added under stirring and mixed for 30 minutes at room temperature. The bis(sulfosuccinimidyl) suberate acts as a cross-linker between the SPION and the lysine-cRGD peptide.

- (3) The reaction mixture was purified by Sephadex G25 column to remove unreacted Bis(sulfosuccinimidyl) suberate.
- (4) Amino-Cyclo-RGD (100 μg) was mixed with cross-linker activated SPION solution and stirred at room temperature for 4 hours.
- (5) The RGD-SPIONs were purified and concentrated by centrifuging through a 30,000 MW cut-off centrifuge filter at 9,000 rcf for 30 min.

A second method for the RGD conjugation was developed using an alternative cross-linker, sulfo-SMCC.

- (1) Amino-SPION (0.9 nmole) in PBS was transferred to a 10 mL vial.
- (2) An over-excess of sulfo-SMCC (26 μg) was added to amino-SPION under stirring and reacted for 30 min at room temperature. The sulfo-SMCC acts as a bifunctional cross-linker between the SPION and the cysteine-cRGD peptide.
- (3) The reaction mixture was purified by Sephadex G25 column to remove unreacted sulfo-SMCC.
- (4) Thiol-Cyclo-RGD (100 μg) was mixed with activated SPION solution and stirred at room temperature for 1 hour.
- (5) The RGD-SPIONs were purified and concentrated by centrifuging through a 30,000 MW cut-off centrifuge filter at 9,000 rcf for 30 min.

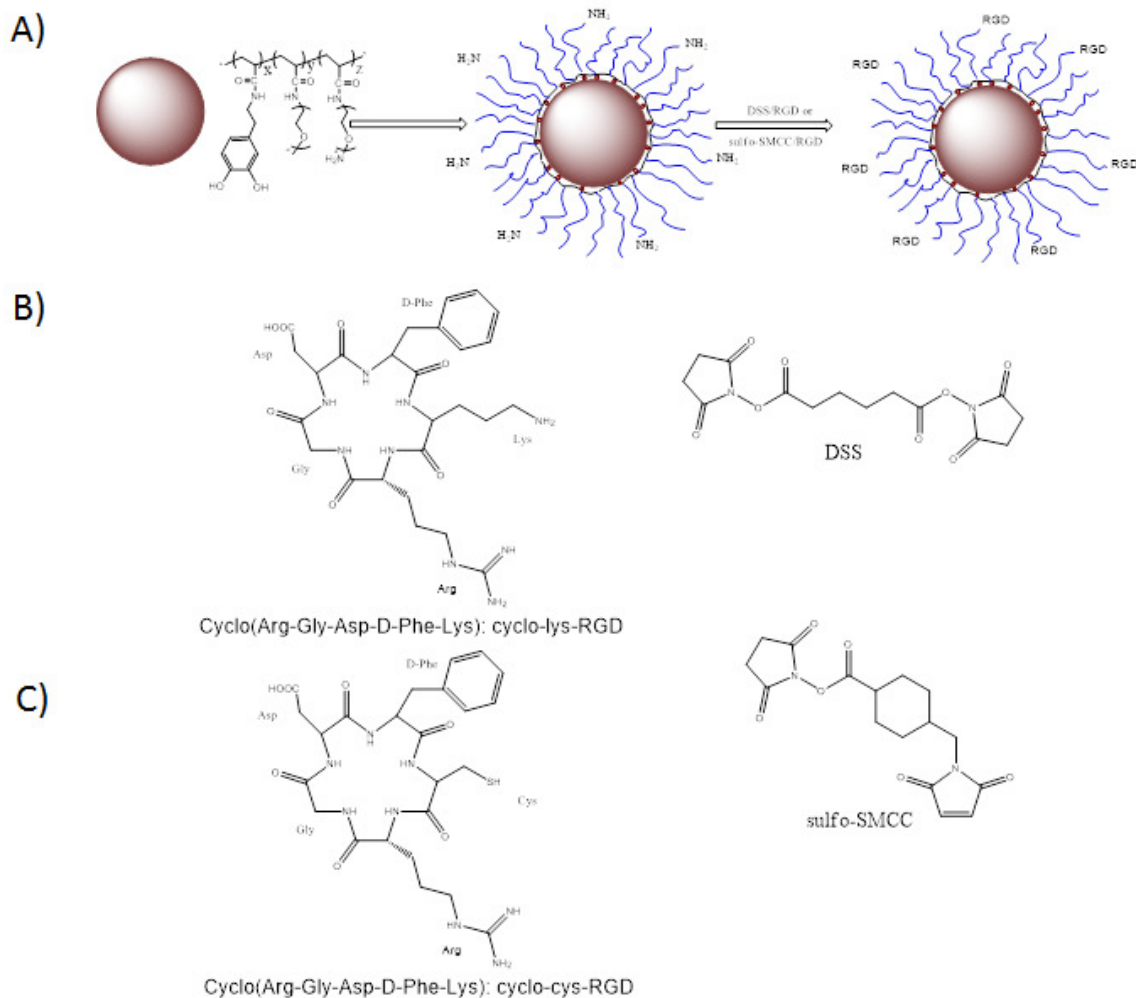


Figure 17 A) Schematic of the nanoparticle targeting with RGD peptide. B) The first strategy developed using the Bis(sulfosuccinimidyl) cross-linker. C) The second strategy developed using the sulfo-SMCC cross-linker. ia.com

3.4. SPION physical and magnetic characterization

The physical and magnet properties of the SPIONs will influence their interaction with biological compartments and their usefulness as molecular imaging probes. To characterize these properties, a number of methods were used.

3.4.1. Transmission electron microscopy

The size of the inorganic nano-crystal core was measured by imaging the nanoparticles through transmission electron microscopy (TEM) with a JEOL JEM-1230 Electron Microscope operating at an accelerating voltage of 120 KV. The samples were prepared by spreading a dilute toluene solution of SPION onto carbon-coated copper grid (Formvar/Carbon 300 Mesh Cu). These images were processed using ImageJ, an open source Java-written program developed by the National Institute of Health for image analysis. The steps of this process are described below:

- (1) The scale of the image is defined in the software by matching a scale line to the scale bar in the TEM image.
- (2) The background of the image was removed by subtracting a Gaussian blur filter image with a radius much larger than the nano-particle size (usually 150 nm).
- (3) The image was thresholded to give high nano-particle contrast and sharp edges.
- (4) The 'analyze particles' tool was used to measure the area of the particles in the image. Usually around 300 nanoparticles are analyzed.
- (5) When the particles appear round in the image, the radius (r) of each particle is calculated from the area (A) as shown in equation 2:

$$r = \sqrt{A/\pi}$$

- (6) An average radius is calculated and a histogram of the nanoparticles radius frequency is produced.

3.4.2. Hydrodynamic size and zeta potential measurement

The hydrodynamic size of the SPIONs differs from the size of the core, because the hydrodynamic size is measured while the nanoparticles are in suspension and it represents the whole size of the nanoparticle, including inorganic core and polymer layer. The hydrodynamic

size of the nano-particles was measured through dynamic light scattering (DLS) using a Zeta Sizer Nano Series ZEN3600 (Malvern, USA). In DLS, coherent monochromatic laser light (635 nm) is diffracted by the nanoparticles. The rate of change of the fluctuation of the diffraction pattern is related to the Brownian motion of the nanoparticle, which is related to the nanoparticles size. The zeta potential is the electrokinetic potential between the surface of nanoparticle coating and the dispersion medium. This potential was also calculated with the Zeta Sizer Nano Series ZEN3600, by measuring the effect of an external electric field on the nanoparticle motion.

3.4.3. Iron and manganese concentration measurement

For the purposes of relaxometry and calculating the injected dose of nanoparticles it is necessary to measure the iron and manganese concentrations of each SPION suspensions. This was accomplished through inductively coupled plasma (ICP) atomic emission spectroscopy with a Vista-MPX CCD Simultaneous ICP-OES (Varian). In ICP, samples are excited and produce optical emission dependent on the atomic composition. The magnitude of the optical emission of an atom's characteristic wavelength correlates to that atom's concentration. Standards of iron and manganese were used to find the characteristic wavelengths of iron at 238.2 nm, manganese at 257.6 nm and to make a calibration standard curve. Samples were digested for three days using a 7% nitric acid solution before ICP measurement.

3.4.4. Relaxometry

The strength of SPIONs as MR contrast agents is best evaluated by quantifying the increase in relaxation rate on the surrounding protons per unit concentration, or “specific relaxivity” (r_2).

This section will describe the method used to evaluate r_2 , while results from this method will be

given later in sections 3.5.1 through 3.5.5. Any data shown here is used as an example depicting the method. During relaxometry, the T_2 perimeter is measured of a number of SPION doped vials. T_2 is the time at which the transverse magnetization is reduced to 37% ($1/e$) of its original value after excitation. The effect of the contrast agent on the water of each vial is best described using transverse relaxation rates (R_2) rather than times (T_2), which have an inverse relationship, as shown in equation 3.

$$3 \quad R_2 = 1 / T_2$$

Relaxation rates are additive, so the relaxation rate observed in a vial (R') is the sum of the water's relaxation rate (R) and the relaxation induced by the SPIONs (R_{Spion}).

$$4 \quad R' = R + R_{Spion}$$

Within the range of concentrations useful for MRI imaging, the relaxation induced by the SPIONs is directly proportional to the concentration of the SPION (C) and the SPION's specific relaxivity (r_2), as depicted in equation 5.

$$5 \quad R_{Spion} = r_2 C$$

By combining equations 3, 4, and 5, it is possible to define the r_2 of a SPION sample in terms of the T_2 of a contrast free vial of water ($T_{2_{water}}$), the measured T_2 of a contrast doped vial ($T_{2_{vial}}$), and the known SPION concentration (C) within that vial.

6

$$r_2 = \frac{1}{T2_{vial}} - \frac{1}{T2_{water}} \cdot C$$

For each relaxometry measurement, a phantom was produced containing vials water suspended SPIONs at known concentrations of iron (as measured by ICP) and one contrast free vial. A representative phantom and image are shown in Figure 18 for the purpose of describing the method, but results are shown in sections 3.5.1 through 3.5.5.

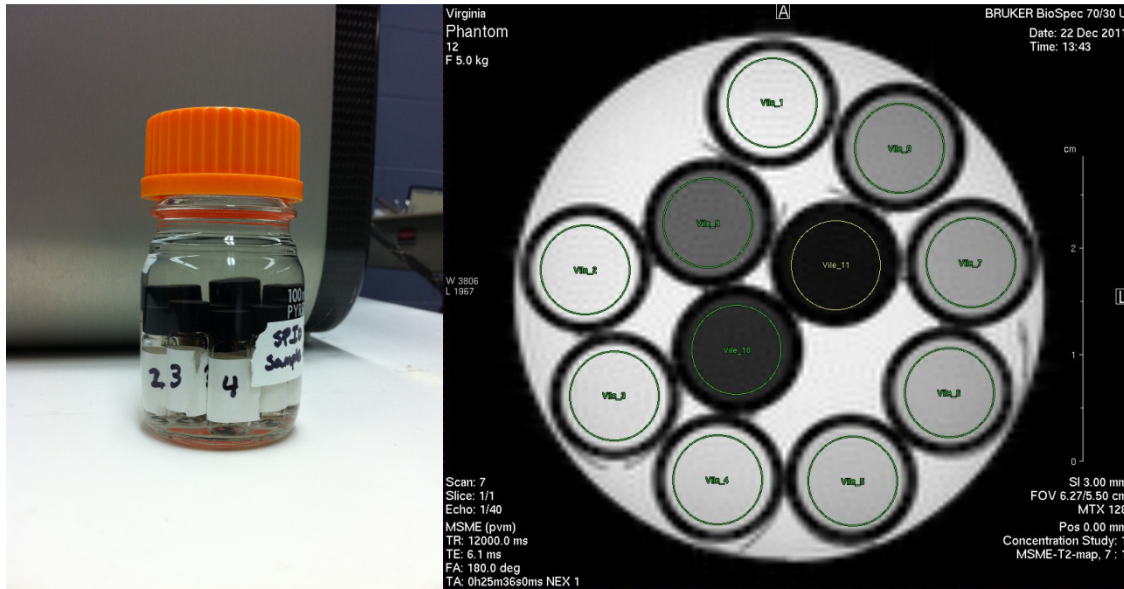


Figure 18: The SPIONs are loaded into vials at known concentrations, including one control vial without any SPION added. These vials are incorporated into a phantom that is imaged and the T₂ value of each vial is calculated. The decrease in T₂ with respect to increasing SPION concentration yields the transverse relaxivity (R₂) of the SPION sample.

This phantom was imaged in the 7T BioSpec 70/30 small animal MRI scanner (Bruker), with a multiple-slice multiple-echo (MSME) sequence where the echoes are acquired at times (TE) ranging from 10 ms to 640 ms in 10 ms increments, and a repeat time (TR) of 12,000 ms. This produces 64 images of one slice of the phantom at 64 different TEs, similar to the image in Figure 18. The signal intensity from each voxel decreases with longer TEs at a rate defined by the transverse relaxivity (T₂). By plotting the signal intensity of a region of interest within each vial vs. echo time, as shown in Figure 19, the rate of signal loss can be fitted. T₂ is the time at

which the transverse magnetization—and with this imaging sequence, the signal, is reduced to 37% (1/e) of its original value. This value is calculated for a ROI within each vial.

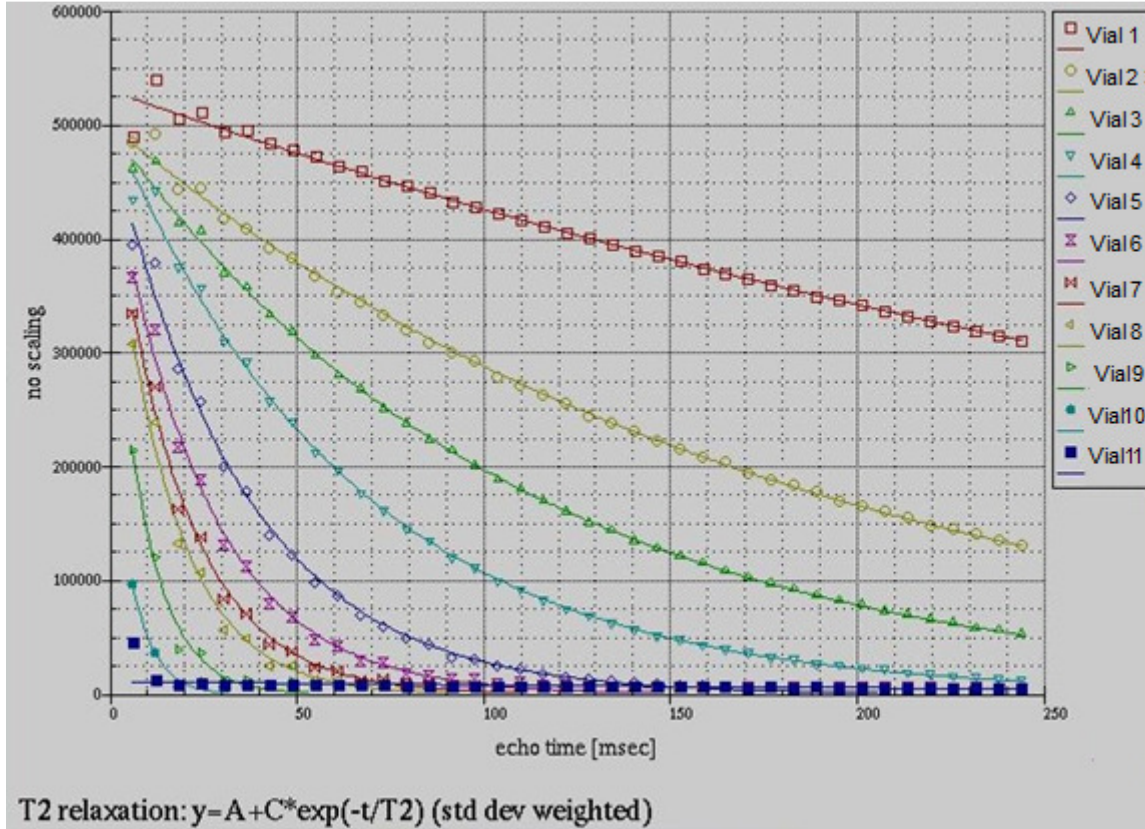


Figure 19 Plotting the signal of a vial’s ROI versus the echo time shows the transverse relaxation of the SPION suspension within each vial. Higher concentrations of SPION (and higher vial numbers in this example) result in greater signal loss with increasing TE.

Using the T_2 of the SPION loaded vials (ms), the T_2 of the non-SPION vial (ms), and the SPION concentrations (mM of Fe), the r_2 of each vial was calculated using equation 6 (1/mM*s). The average of all of the SPION loaded vials was used as the relaxivity value and the standard deviation of the measurements was used to evaluate the uncertainty.

3.4.5. Gamma emission characterization and quantification

The gamma emission spectrum was initially characterized for the ^{59}Fe samples using a Perkin Elmer LKB Wallac 1282 compugamma CS universal gamma counter. For quantification of ^{59}Fe

using the gamma-counter, a program was implemented which windowed using channels 222 through 236, corresponding to the 1099 keV and 1292 keV gamma emission. The efficiency of the counter using this program was evaluated using equation 7 by comparing the emission from three ^{59}Fe standards and their known nominal activities.

$$7 \quad \text{Efficiency} = \frac{\text{measured activity (CPM)}}{\text{nominal activity (DPM)}}$$

For ^{59}Fe , the efficiency of the counter was $15.2 \pm 0.2\%$.

3.5. Nano-particle characterizations

As an overview, the characteristics of TEM measured particle size, DLS measured hydrodynamic size, zeta potential, and relaxivity are shown for the 5 synthetic routes describes in Sections 3.1.1 through 3.2.2 and 3.2.5 are shown in Table 6. All nanoparticles were coated with multidentate poly-ethylene-glycol ligands. The natural SPIONs were coated molecular weight 550 PEG using the SDS ligand exchange described in 3.3.1, and thus does not have a valid zeta potential measurement. All other nanoparticles in Table 6 are coated with molecular weight 2000 PEG and the ligand exchange was accomplished without the use of SDS.

Table 6: Nanoparticle characteristics of different synthetic routes.

Nanoparticle Metal(s)	Nanoparticle structure	TEM radius (nm)	DLS radius (nm)	Zeta potential (mV)	Radionuclide used	r_2 ($\text{s}^{-1}\text{mM}^{-1}$ of metal)
Fe	Core	4.3 ± 1.3	25 ± 5	NA	None	72 ± 10
Fe	Core/Shell	5.0 ± 1.5	17 ± 6	-46 ± 5	^{59}Fe (130 μCi)	97 ± 3
Fe, Mn	Core	3.3 ± 1.0	15 ± 5	-20 ± 6	None	90 ± 1
Fe, Mn	Core/Shell	4.4 ± 1.6	18 ± 4	-16 ± 4	None	234 ± 8
Fe, Mn	Core	4.0 ± 1.0	17 ± 5	-42 ± 9	^{52}Mn	220 ± 40
Fe, Mn	Core/cRGD	4.0 ± 1.0	34 ± 14	-27 ± 17	^{52}Mn	200 ± 20

The relaxivity of the nanoparticles varied considerably between different production batches. This is possible due to difficulty controlling the aspects of reaction environment, such as temperature. Unlike organic synthesis, the synthesis of nanoparticles is not 100% reproducible because the final product is a mixture of different size/composition particles. The relaxivity of samples remained stable up to one month, as shown in Table 7.

Table 7: Relaxometry results of a single MION sample over one month. Nanoparticles were coated with molecular weight 2000 PEG.

Date of relaxometry	Nanoparticle Metal(s)	Nanoparticle structure	r_2 (1/s*mM of metal)
5/11/2012	Fe, Mn	Core	140 ± 8
5/18/2012	Fe, Mn	Core	134 ± 10
5/25/2012	Fe, Mn	Core	136 ± 6
6/12/2012	Fe, Mn	Core	130 ± 10

3.5.1. Natural SPION

The first step of the hybrid PET/MRI nanoparticle synthetic development was to create a non-radioactive SPION core and to coat the SPION with a multidentate poly-ethylene-glycol ligand to make the nanoparticle water-soluble and biocompatible. Transmission electron microscopy (TEM) images of these SPIONs were then produced and analyzed as described in Section 3.4.1. A representative TEM image and its analysis are shown in Figure 20. The SPION radius measured from the TEM image, which is characteristic of the nanoparticles' inorganic core, was 4.3 ± 1.3 nm. The SPION hydrodynamic radius was 25 ± 5 nm, as shown in Figure 21 (see Section 3.4.2 for method). The zeta-potential measurement is not available for these nanoparticles, because the use of SDS during the ligand exchange (as explained in Section 3.3.1) made the measurements invalid. After the iron concentration of the SPION solution was measured using ICP (see Section 3.4.3), the relaxivity of the SPIONs was measured and calculated to be 72 ± 10 (s*mM of iron)⁻¹.

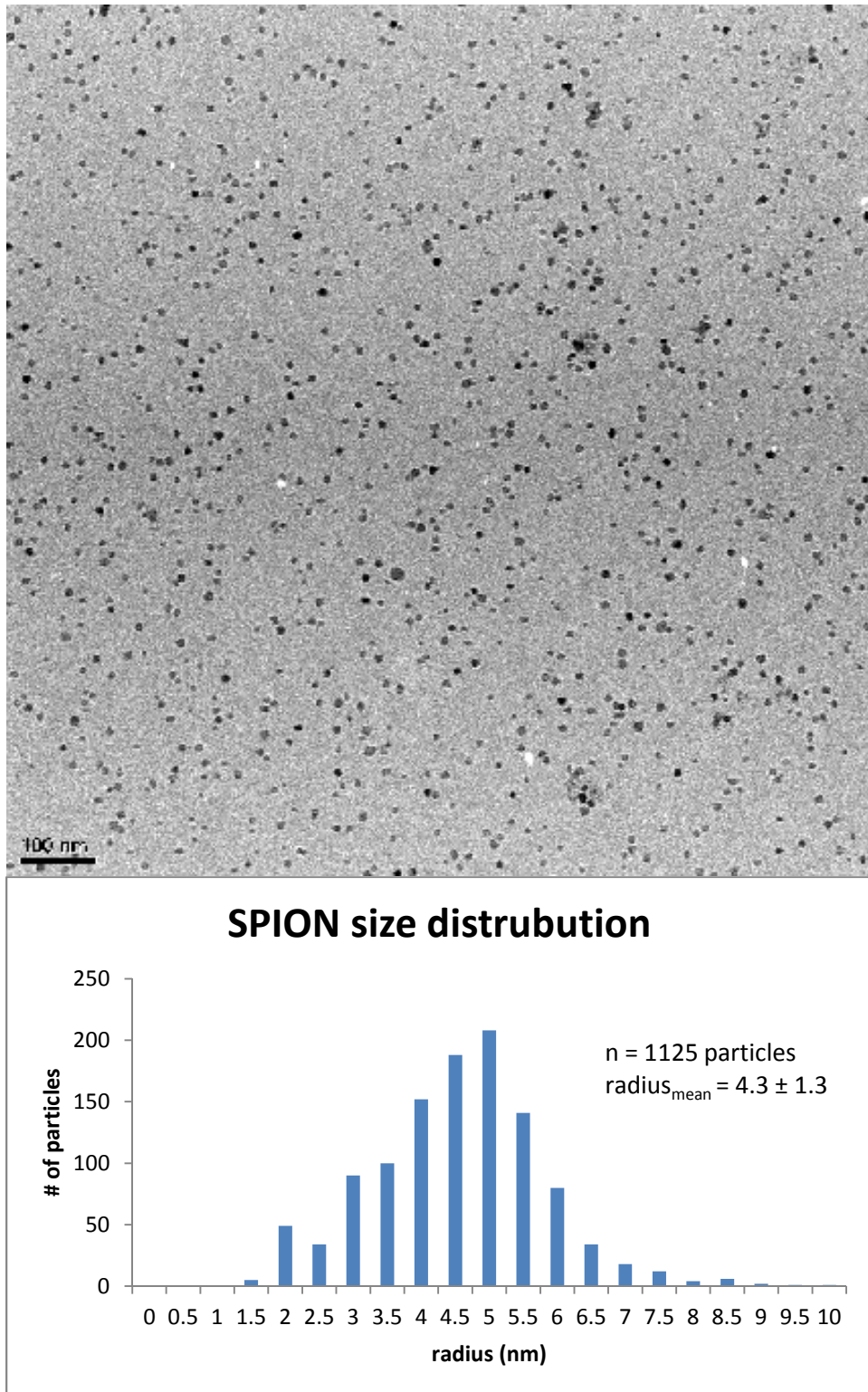


Figure 20: Representative TEM image and histogram of natural SPIONs coated with oleic acid and oleylamine. Samples were prepared by spreading a dilute toluene solution of SPION onto carbon-coated copper grid. The size measured of each particle is characteristic of the size of the inorganic iron oxide core.

Natural SPION hydrodynamic radius

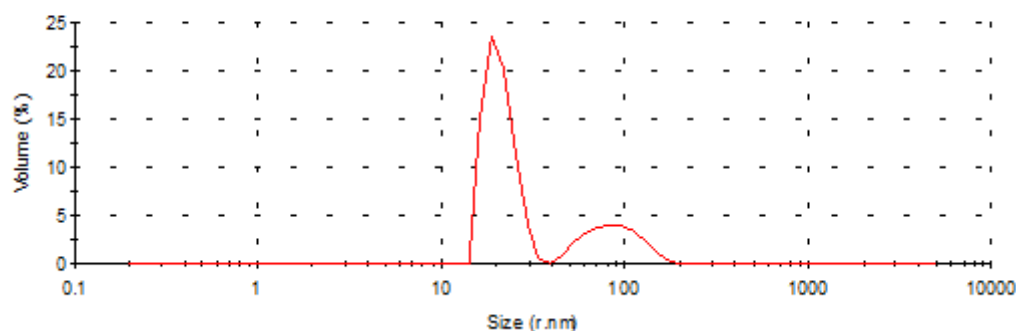


Figure 21: Hydrodynamic radius distribution of natural multidentate poly- ethylene-glycol coated SPIONs as measured through DLS. The left peak is SPION size and the right peak likely represents a small fraction of nanoparticle aggregation.

3.5.2. ^{59}Fe SPION

The synthesis of ^{59}Fe -SPIONs was accomplished with the synthetic method described in Section 3.1. TEM images of these ^{59}Fe -SPIONs were then produced and analyzed as described in Section 3.4.1. A representative TEM image and its analysis are shown in Figure 22. The SPION radius measured from the TEM image, which is characteristic of the nanoparticles' inorganic core, was 5.0 ± 1.5 nm. The ^{59}Fe -SPION hydrodynamic radius was 17 ± 6 nm and the zeta-potential was -46 ± 5 mV, as shown in Figure 23 (see Section 3.4.2 for method). After the iron concentration of the SPIONs was measured using ICP (see Section 3.4.3), the relaxivity of the SPIONs was measured to be 97 ± 3 (s*mM of iron) $^{-1}$. The ^{59}Fe -SPIONs had an activity to iron mass ratio of 32 ± 2 $\mu\text{Ci}/\text{mg}$ of Fe.

Successful incorporation of ^{59}Fe was verified by separating the nanoparticles at 3100 rcf from unreacted iron and by comparing the TEM size of the core to the core/shell structure. The nanoparticle radius increased between 0.5 – 2 nm from the addition of the ^{59}Fe doped shell.

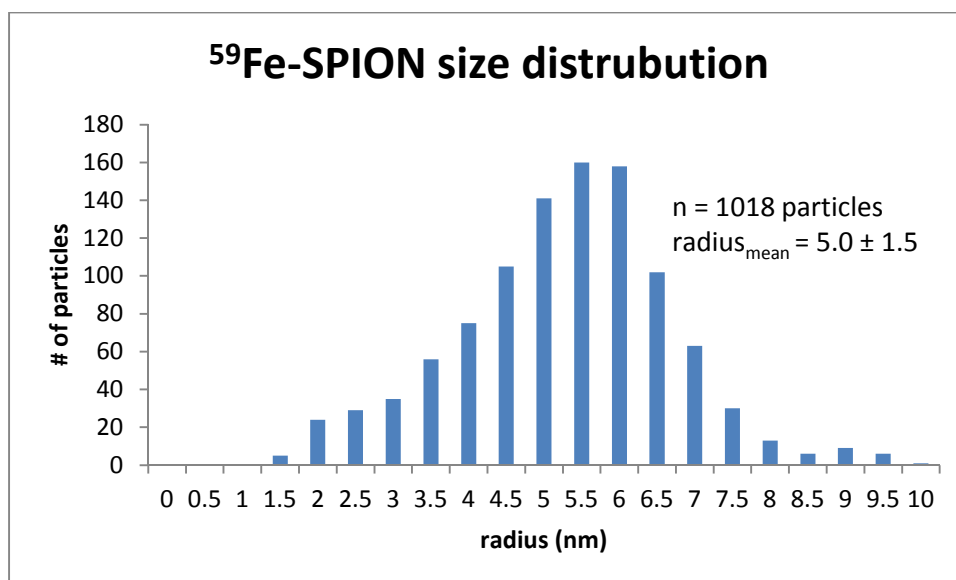
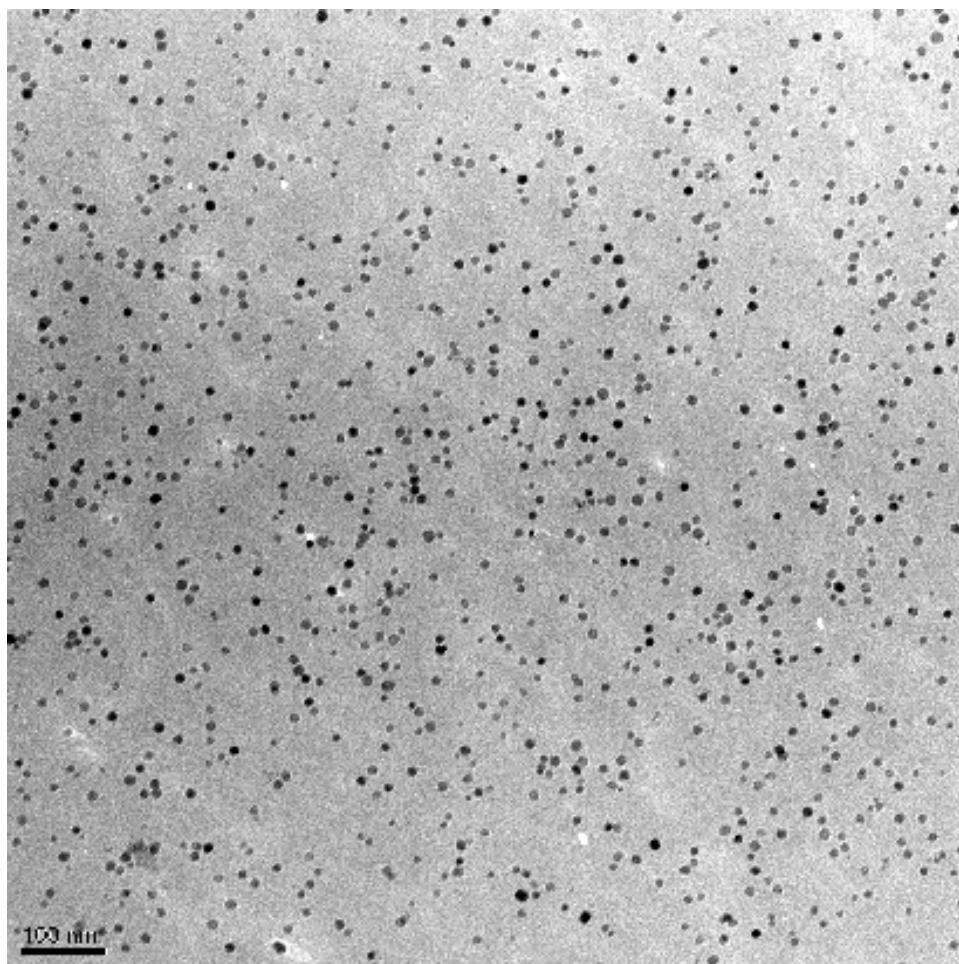


Figure 22: TEM image and histogram of ^{59}Fe -SPIONs coated with oleic acid and oleylamine. Samples were prepared by spreading a dilute toluene solution of SPION onto carbon-coated copper grid. The size measured of each particle is characteristic of the size of the inorganic iron oxide core.

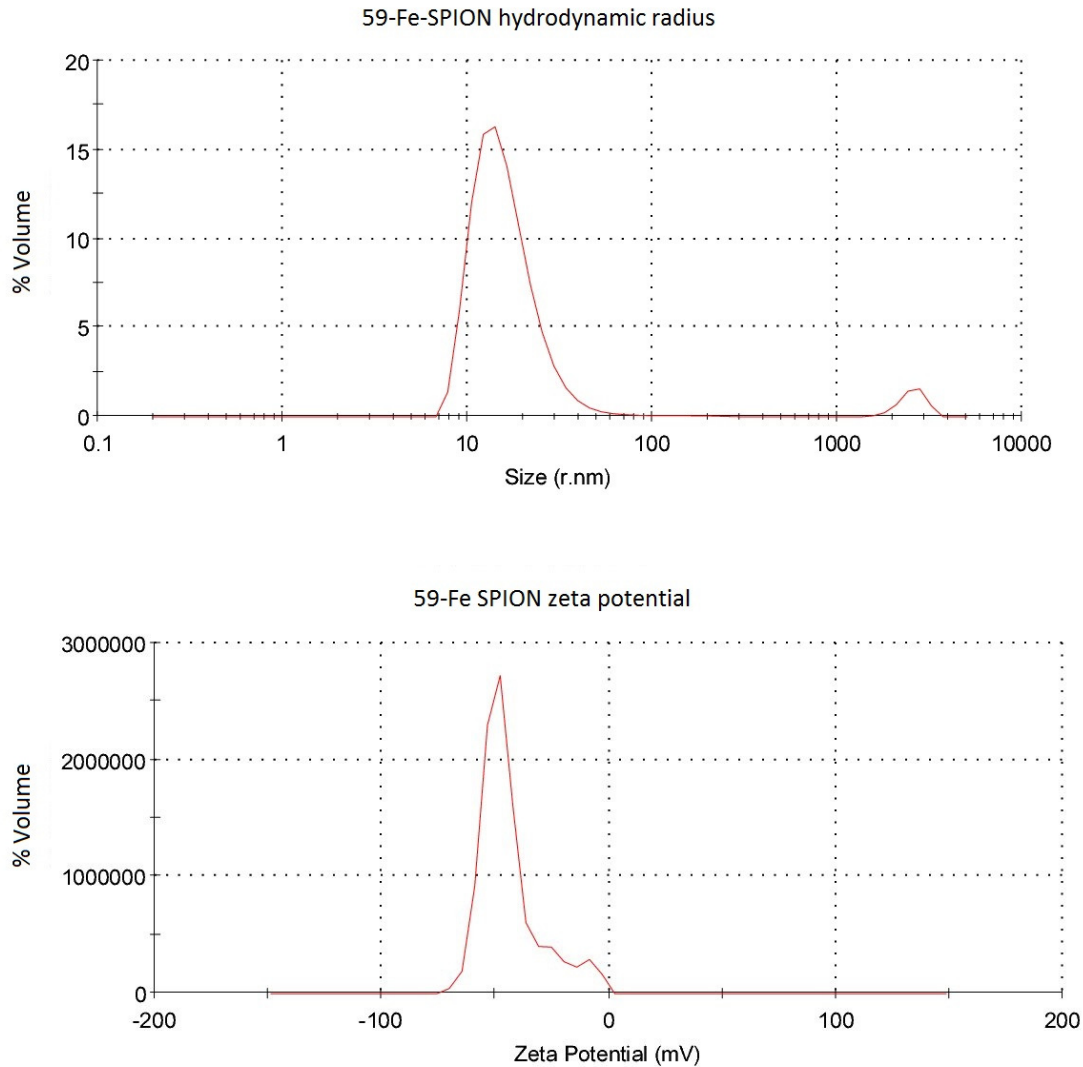
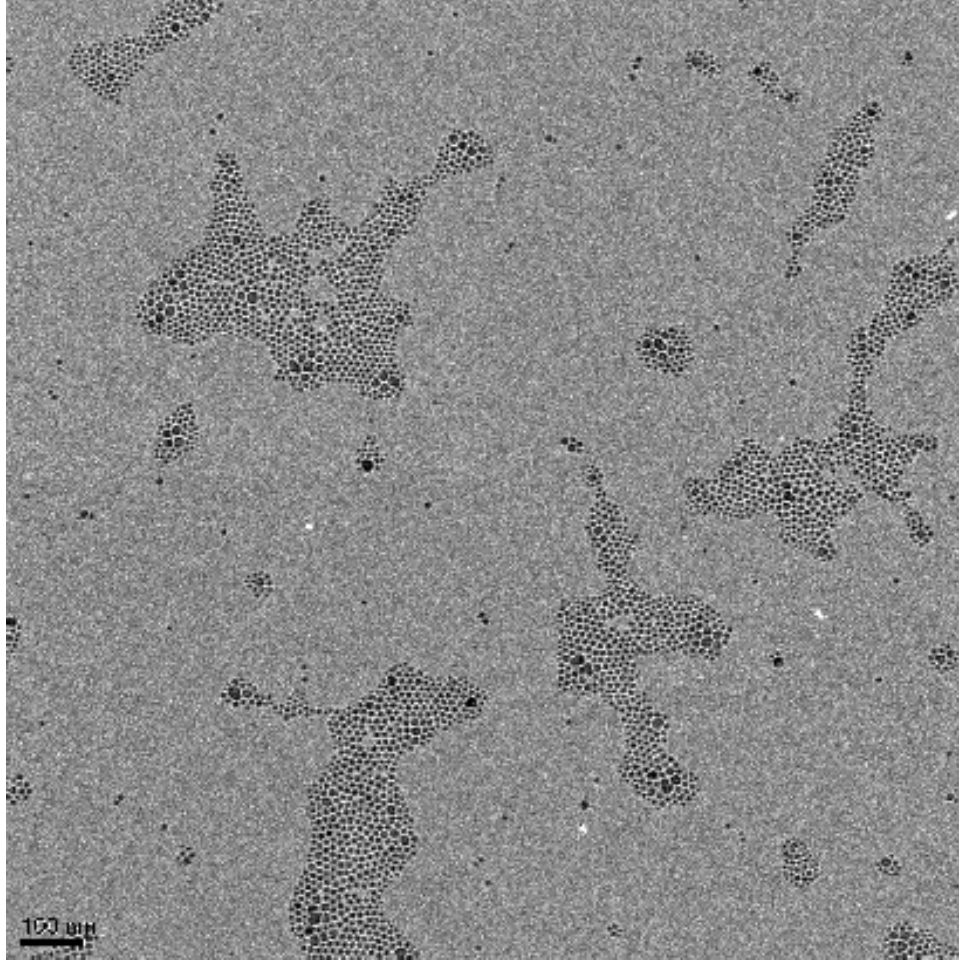


Figure 23: Hydrodynamic radius (top) and zeta potential (bottom) of ⁵⁹Fe-SPION.

3.5.3. Natural MION

The synthesis of natural MIONs was accomplished with the synthetic method described in Section 3.2.1. TEM images of these MIONs were then produced and analyzed as described in Section 3.4.1. A TEM image and its analysis are shown in Figure 24. The MION radius measured from the TEM image, which is characteristic of the nanoparticles' inorganic core, was 3.3 ± 1.0 nm. The MION hydrodynamic radius was 15 ± 5 nm and the zeta-potential was -20 ± 6 mV, as shown in Figure 25 (see Section 3.4.2 for method). After the iron and manganese

concentration of the MIONs was measured using ICP (see Section 3.4.3), the relaxivity of the MIONs was measured to be 97 ± 3 (s*mM of metal)⁻¹.



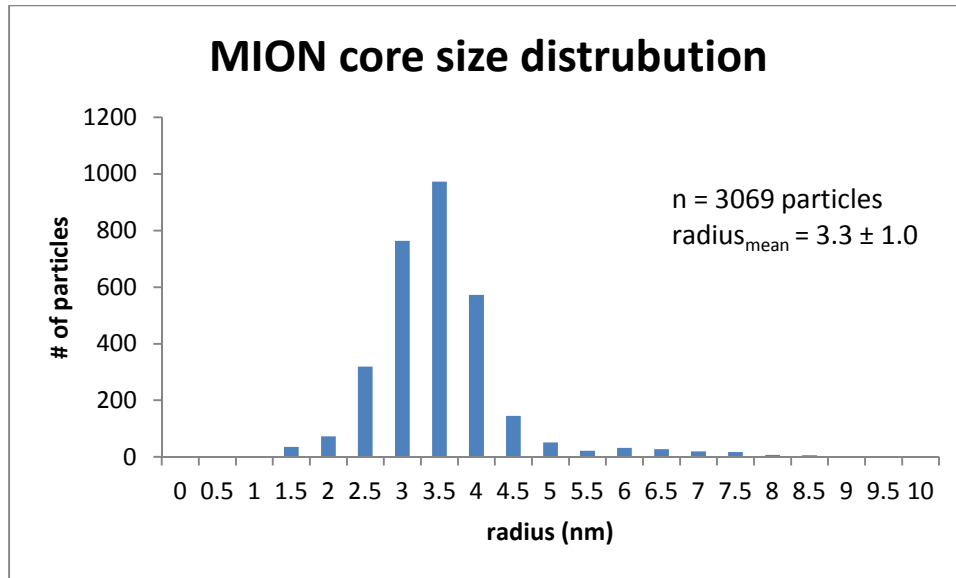


Figure 24: TEM image and histogram of MIONs coated with oleic acid and oleylamine. Samples were prepared by spreading a dilute toluene solution of SPION onto carbon-coated copper grid. The size measured of each particle is characteristic of the size of the inorganic iron oxide core. The clumping of the nanoparticles seen in the TEM image may be a result of the evaporation pattern of the toluene solution.

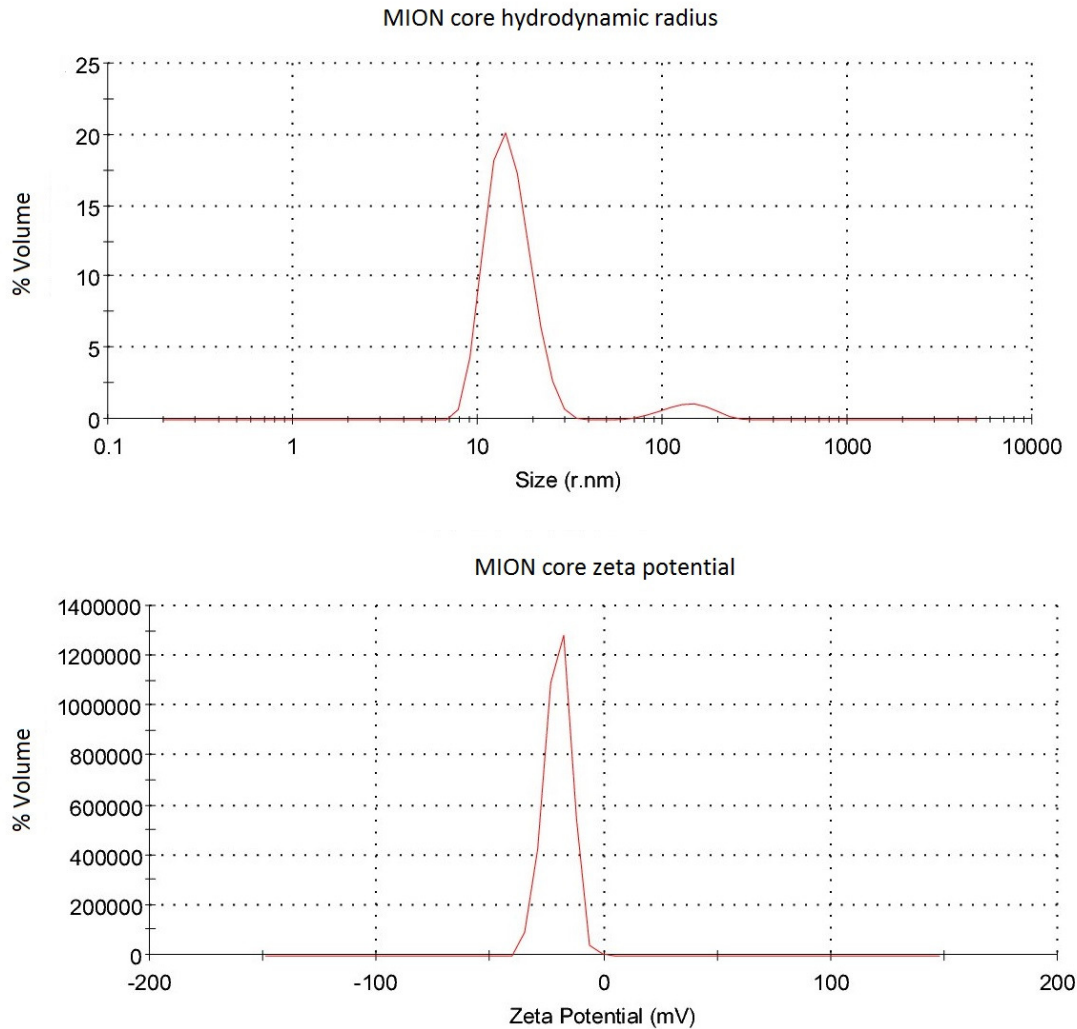
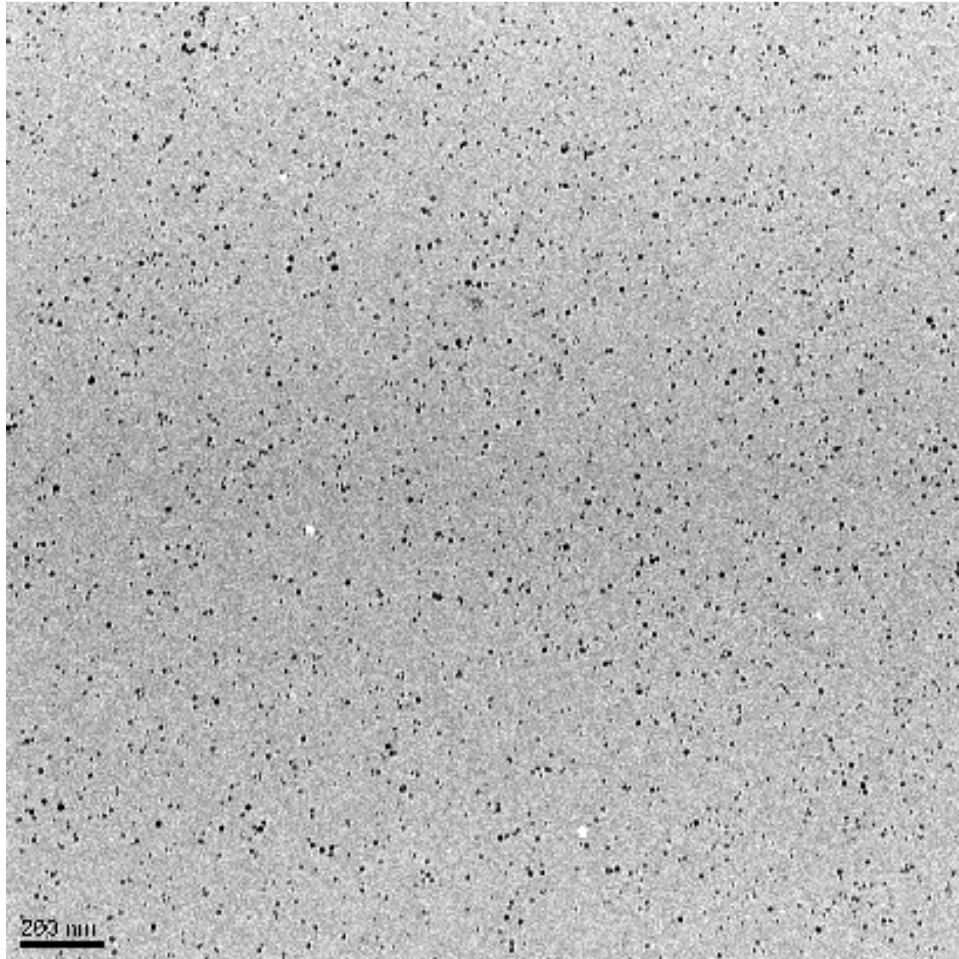


Figure 25: Hydrodynamic radius (top) and zeta potential (bottom) of MION.

3.5.4. MION core/shell

The synthesis of natural MIONs with a core/shell structure was accomplished with the synthetic method described in Section 3.2.2. TEM images of these MIONs were then produced and analyzed as described in Section 3.4.1. A TEM image and its analysis are shown in Figure 18. The MION radius measured from the TEM image, which is characteristic of the nanoparticles' inorganic core, was 4.4 ± 1.6 nm. The MION hydrodynamic radius was 18 ± 4 nm and the zeta-potential was -16 ± 4 mV, as shown in Figure 27 (see Section 3.4.2 for method). To allow for

direct comparison, this data depicts the same nanoparticle cores as shown in Section 3.5.3, but after the addition of the shell layer. After the iron and manganese concentration of the MIONs was measured using ICP (see Section 3.4.3), the relaxivity of the MIONs was measured to be $234 \pm 8 \text{ (s} \cdot \text{mM of metal)}^{-1}$.



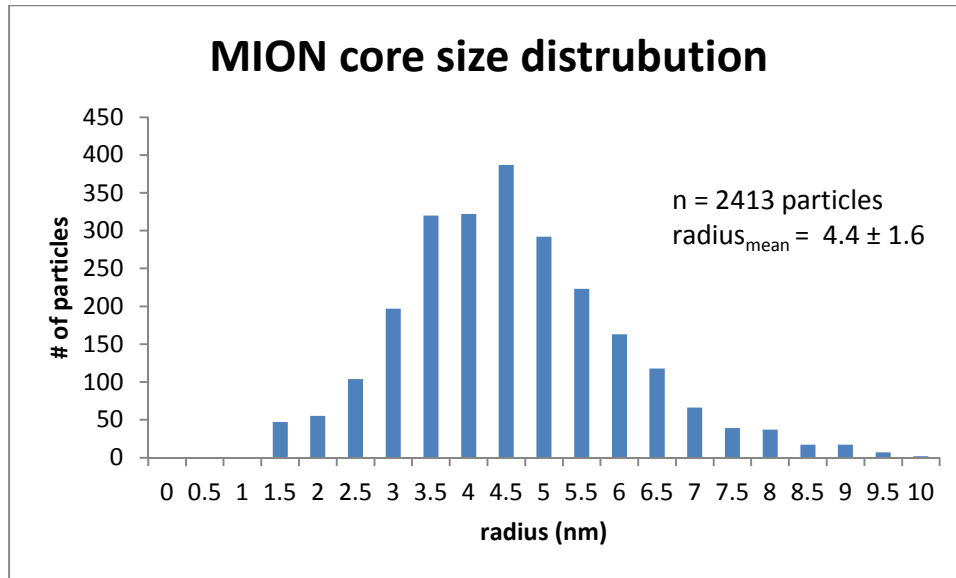


Figure 26: TEM image and histogram of MIONs with a core/shell structure coated with oleic acid and oleylamine. Samples were prepared by spreading a dilute toluene solution of SPION onto carbon-coated copper grid. The size measured of each particle is characteristic of the size of the inorganic iron oxide core.

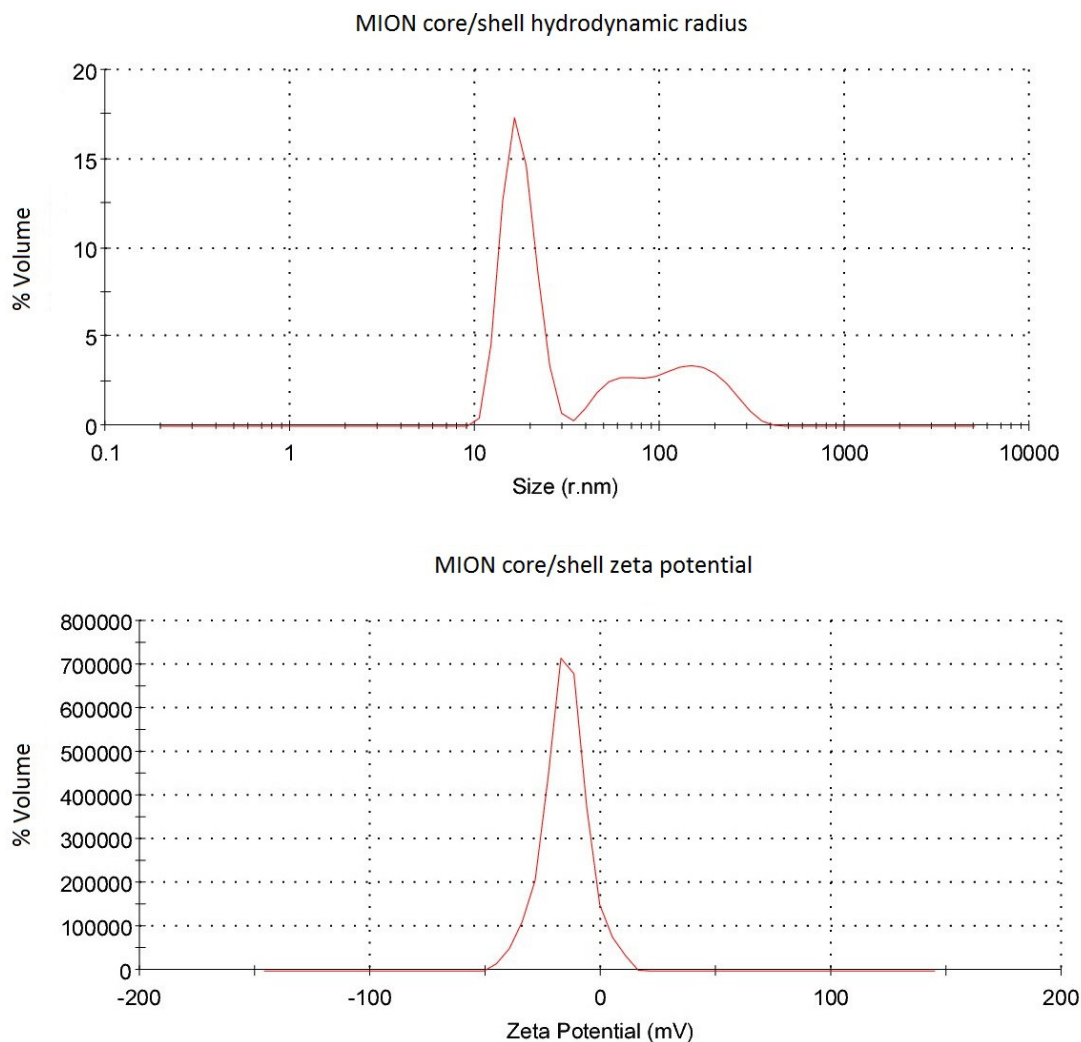


Figure 27 Hydrodynamic radius (top) and zeta potential (bottom) of MIONs with a core/shell structure. The second smaller peak in the DLS figure is possibly caused by minor sample contamination.

3.5.5. [^{52}Mn]-MION

The synthesis of ^{52}Mn -MIONs was accomplished with the synthetic method described in Section 3.2.5. TEM images of these ^{52}Mn -MIONs were then produced and analyzed as described in Section 3.4.1. A representative TEM image and its analysis are shown in Figure 30. The MION radius measured from the TEM image, which is characteristic of the nanoparticles' inorganic core, was 4.0 ± 1.0 nm. The ^{52}Mn -MIONs hydrodynamic radius was measured twice. Once for the untargeted nanoparticles and once for the cRGD conjugated MIONs. For the untargeted

MIONs, the hydrodynamic radius was 17 ± 5 nm and the zeta-potential was -17 ± 5 mV, (see Section 3.4.2 for method), as shown in Figure 28. For the cRGD conjugated MIONS, the hydrodynamic radius was 34 ± 14 nm and the zeta-potential was -27 ± 17 , as shown in Figure 29. The increase in hydrodynamic size is likely a result of the addition of cRGD peptide to the nanostructure and the greater unraveling of the multi-dentine PEG ligands. After the iron concentration of the MIONs was measured using ICP (see Section 3.4.3), the relaxivity of the cRGD conjugated MIONs and the untargeted MIONs was measured to be 220 ± 40 (s*mM of iron)⁻¹ and 200 ± 20 (s*mM of iron)⁻¹ respectively. These measurements represent the cRGD targeted and the untargeted MIONs used in the animal experiments described in chapter 5. The ⁵²Mn-MIONs had a activity to mass of iron ratio of $1.47 \pm .06$ μ Ci/mg of Fe.

Successful incorporation of ⁵²Mn was verified by separating the nanoparticles at 3100 rcf to isolate the nanoparticles from unreacted iron and manganese.

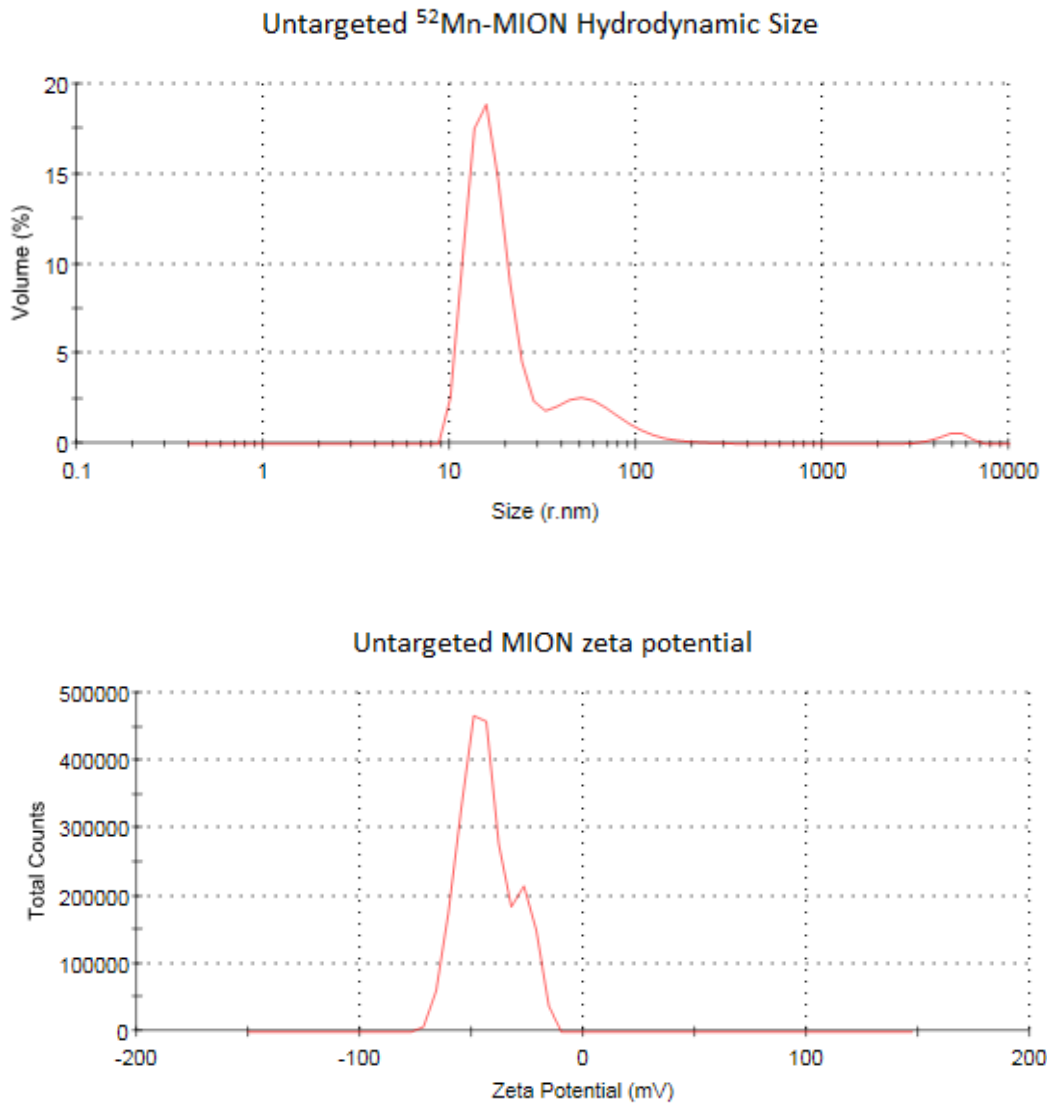


Figure 28: Hydrodynamic radius (top) and zeta potential (bottom) of untargeted ⁵²Mn-MIONs.

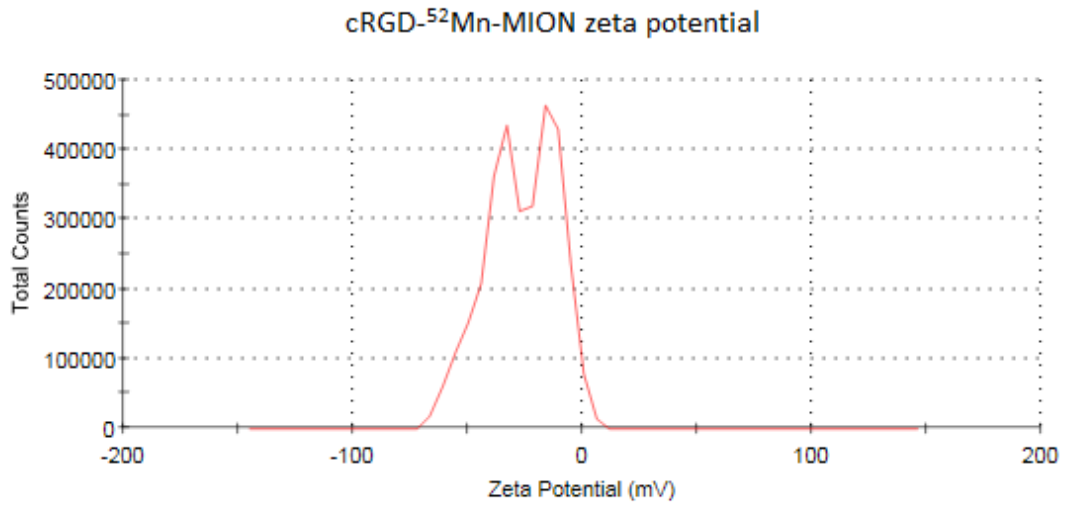
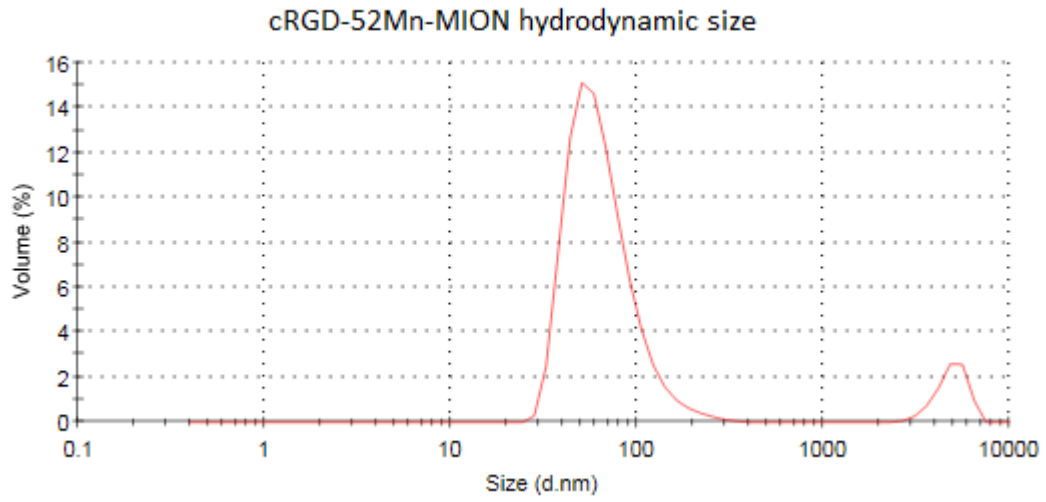


Figure 29: Hydrodynamic radius (top) and zeta potential (bottom) of ^{52}Mn -MION-cRGDs.

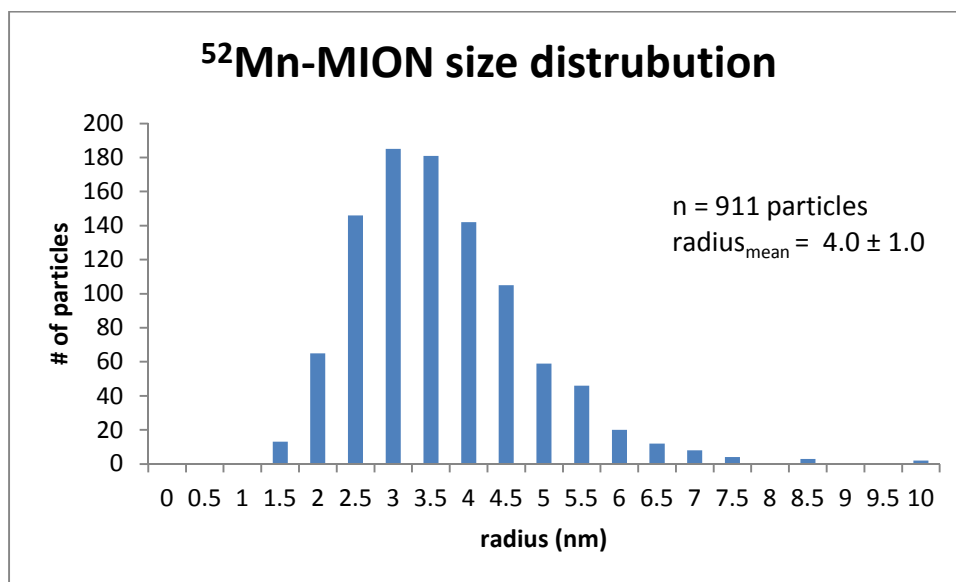
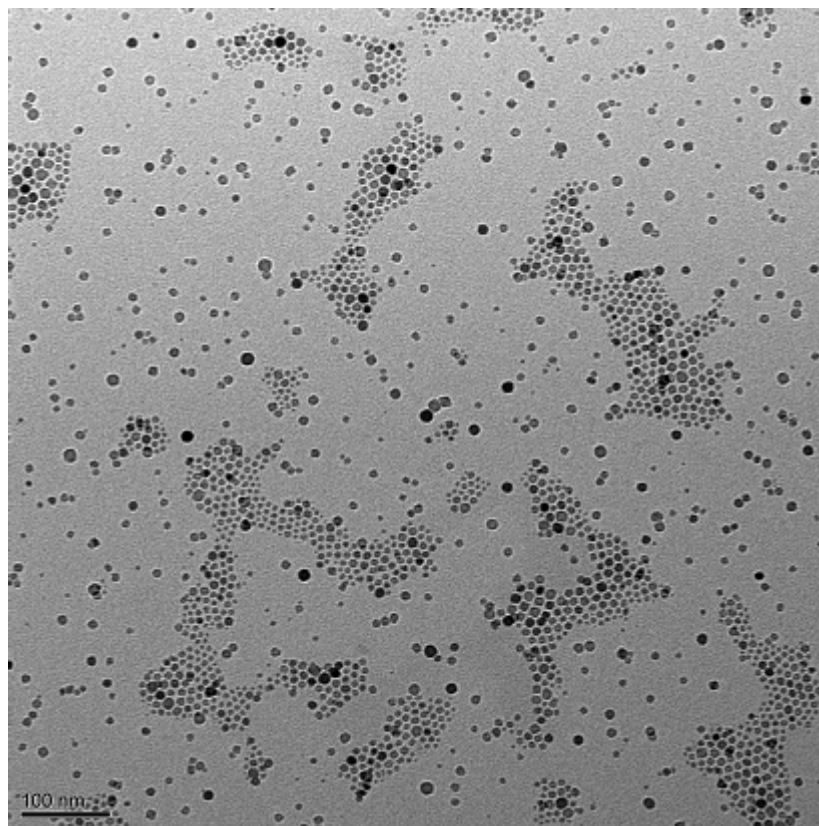


Figure 30: TEM image and histogram of ^{52}Mn -MIONs coated with oleic acid and oleylamine. Samples were prepared by spreading a dilute toluene solution of SPION onto carbon-coated copper grid. The size measured of each particle is characteristic of the size of the inorganic manganese iron oxide core.

Chapter 4

4. [⁵⁹Fe]-SPION Evaluation

To evaluate the potential of this nanoparticle for targeted molecular imaging, the non-targeted SPION's *in vivo* behavior was evaluated. Specifically, the [⁵⁹Fe]-SPIONs were utilized in imaging and biodistribution studies with non-tumor bearing mice. Injected mice were MR imaged and the MR results were compared with the biodistribution results. Finally, signal contrast mapping was demonstrated using the imaging data obtained before and after [⁵⁹Fe]-SPION injection imaging results.

4.1. [⁵⁹Fe]-SPION Biodistribution

In order to evaluate the *in vivo* pharmacokinetics of the non-targeted nanoparticles, a biodistribution study was conducted using ⁵⁹Fe-SPIONs. All animal experiments were approved and performed according to the policies and guidelines of the Institutional Animal Care and Use Committee (IACUC) at Virginia Commonwealth University. Adult male and female nude mice (n=15) were injected through the tail-vein with 26 ± 1 ug Fe and 840 ± 30 nCi of ⁵⁹Fe-SPION. Doses were drawn, weighed, and then diluted with saline to 200 μ L.

The mice (3) were sacrificed at each of five time points ranging from 1 to 144 hours post injection. Tissues were harvested, weighed, and the gamma-emission was measured.

$$8 \quad \%ID/g = 100 \frac{\text{tissue activity (CPM)}}{\text{injected activity (CPM)}} \text{tissue mass (g)}$$

The percent injected dose per gram (%ID/g) of each tissue was calculated from the decay corrected activity of the tissue (tissue activity), the activity injected, and the mass of the tissue, using equation 8. The injected activity was calculated by measuring the mass of the empty syringe and the full syringe. The difference represented the mass of nanoparticle solution in the syringe (g), and this was related to the activity (CPM) by measuring the activity of a known standard of SPION solution (CPM/g). The residual activity in the syringe after injection was measured (CPM) and subtracted from the activity in the syringe to give the injected activity (CPM).⁶⁷

A similar procedure was used to characterize the biodistribution of ⁵⁹FeCl₃, as a non-SPION control at 24 hours and 144 hours after injection. An aqueous solution (1 μL) of ⁵⁹FeCl₃ in hydrochloric acid was diluted into 600 μL of deionized water, and neutralized to pH 3.5 with .00023 M sodium hydroxide. Doses were drawn to 40 μL (0.23±.3 μCi) and then further diluted to 200 μL with saline solution before injection. The %ID/g of each tissue was calculated as described above.

4.2. MR imaging of ⁵⁹Fe-SPION

In order to establish the usefulness of the iron oxide nanoparticles as MR contrast agents, each mouse of the ⁵⁹Fe-SPION biodistribution study was MR imaged before injection and before

sacrifice using the 7T BioSpec 70/30 small animal MRI scanner (Bruker, Billerica, MA). A Fast Imaging with Steady State Precession (FISP) sequence was used with a repeat time (TR) of 9.4 ms and echo time (TE) of 4.7 ms and number of scans averaged (NSA) of 4. A flip angle (FA) of 35° was used to achieve T2*/T1 weighted images. Smaller flip angles were used to achieve proton density weighted images and larger flip angles resulted in images with unacceptably low signals. The short TR (9.4 ms) allowed for a 384×128×128 matrix acquisition with isotropic 274 micron voxels (FOV = 10.5×3.5×3.5 cm). The isotropic acquisition of specifically developed to allow for future comparison with isotropic PET data. Attenuator and receiver gain values were recorded from the pre-injection imaging and reused for the pre-sacrifice imaging.

The un-gated acquisition time was 614 s. A bellows was placed under the mouse and a Control / Gating Module (SA Instruments) was used to acquire the mouse's respiratory cycle. The MR sequence was actively gated to avoid acquisition during inhalation and exhalation. This gating increased the acquisition time to ~13 minutes. The mice were anesthetized under 2% isoflurane flow during imaging. The images were exported in Digital Imaging and Communications in Medicine (DICOM) format for processing and analysis using the 3DSlicer software package.⁶⁸

Regions of interest (ROIs) were drawn on the brain, kidneys, and liver of each mouse before and after injection to quantify the contrast caused by the ⁵⁹Fe-SPION injection at different times. The contrast was compared with the ⁵⁹Fe accumulation from the biodistribution study. Then a phantom containing known concentrations of SPION iron was imaged using the same MR sequence that was used for the *in vivo* imaging to produce a standard curve of SPION iron concentration versus MR contrast in water. By linearly interpolating between the points on the standard curve, the SPION iron concentration of each ROI was evaluated. These concentration

values from the MRI data were compared to concentration values calculated from the biodistribution %ID/g values, as shown in equation 9.

$$9 \quad C_{SPION} \left(\mu g \text{ of } \frac{\text{iron}}{\text{mg}} \right) = \% \frac{\text{ID}}{100} \times \text{ID} (\mu g \text{ of iron}) \times \frac{1g}{1mL}$$

4.3. Signal contrast mapping

The SPIONs effectively reduced the MR signal from a number of tissues. To spatially characterize this effect, signal contrast maps were created from the pre-injection and pre-sacrifice images. The pre-sacrifice images were deformed and co-registered to the pre-imaging images using the basis spline algorithm available in the 3DSlicer software package (BRAINSFit). The quality of the co-registration was only evaluated visually. The percent signal contrast (%SC) of each voxel was then calculated from the pre-injection signal ($S_{injection}$) and the pre-sacrifice signal ($S_{sacrifice}$) using equation 10.

$$10 \quad \%SC = \frac{S_{injection} - S_{sacrifice}}{S_{injection}}$$

Voxels that resulted in a negative %SC, or “signal gain,” were thresholded to a %SC value of zero, as the signal gain is not accurately attributed to of the SPION injection. Initially, the signal contrast mapping was developed for analytical comparison with PET data, but due to the difficulty of deformably co-registering PET/CT to MRI datasets, ROI analysis was utilized instead.

4.4. [⁵⁹Fe]-SPION in vivo evaluation results

4.4.1. Biodistribution

The %ID/g values of the ⁵⁹Fe-SPIONs in blood and other major organs at different times after injection is given in Table 8 and shown in Figure 31. These values differed from the ⁵⁹FeCl₃ biodistribution given in Table 9 and shown in Figure 32, indicating that the SPION nano-structure was affecting the ⁵⁹Fe pharmacokinetics. Both ⁵⁹Fe-SPIONs and ⁵⁹FeCl₃ exhibit accumulation in the liver and spleen. The accumulation of ⁵⁹Fe-SPION in the spleen was significantly less than the accumulation of ⁵⁹FeCl₃ at both 24 hours (p = 0.012) and 144 hours (p = 0.019). At 24 hours, the accumulation of ⁵⁹Fe-SPION in the liver (39±3 %ID/g) was not significantly less than ⁵⁹FeCl₃ (46±8 %ID/g) accumulation (p = 0.23), but at 144 hours there was significantly less ⁵⁹Fe-SPION accumulation in the liver (31±2 %ID/g) than ⁵⁹FeCl₃ (50±10) accumulation (p = 0.041).

Table 8: Biodistribution of intravenously injected ⁵⁹Fe-SPIONs in nude mice (n=3 per time point). Data are presented as %ID/g (mean±stdv) values determined through gamma counting. Nude mice (n=3 per time point) were injected through the tail vein with ⁵⁹Fe-SPIONs (0.84±0.03 μCi; 200 μL; 26±1 μg of Fe). Tissues were collected, weighted, and the gamma emission was measured to calculate the %ID/g.

Organs	1 Hour	4 Hour	24 Hours	72 Hours	144 Hours
Blood	3.9±0.7	1.4±0.3	2.8±0.2	4±0.4	5.5±0.7
Heart	1.2±0.2	0.48±0.07	0.51±0.02	0.8±0.3	0.9±0.2
Lungs	1.9±0.5	0.94±0.04	1.2±0.2	1.3±0.4	1.8±0.2
Liver	46±7	30±7	39±3	33±5	31±2
Spleen	16±6	19±2	17.5±0.9	14±5	15.2±0.3
Stomach	0.4±0.3	0.13±0.04	0.25±0.05	0.2±0.2	0.26±0.1
Intestines	0.7±0.2	0.9±0.1	1.4±0.1	1.3±0.4	0.8±0.1
Kidneys	1.4±0.2	0.7±0.1	0.99±0.1	0.7±0.2	1.4±0.2
Skin	0.9±0.4	0.5±0.2	0.7±0.1	0.9±0.2	0.81±0.03
Muscle	0.9±0.6	0.3±0.3	0.19±0.07	0.3±0.3	0.36±0.07
Skull	2.1±0.9	1.8±0.3	1.5±0.4	2.1±0.4	4±1
Brain	0.14±0.05	0.1±0.1	0.12±0.03	0.12±0.01	0.28±0.08
Femur	5.4±0.5	4.9±0.9	7±2	5.3±0.9	4±1

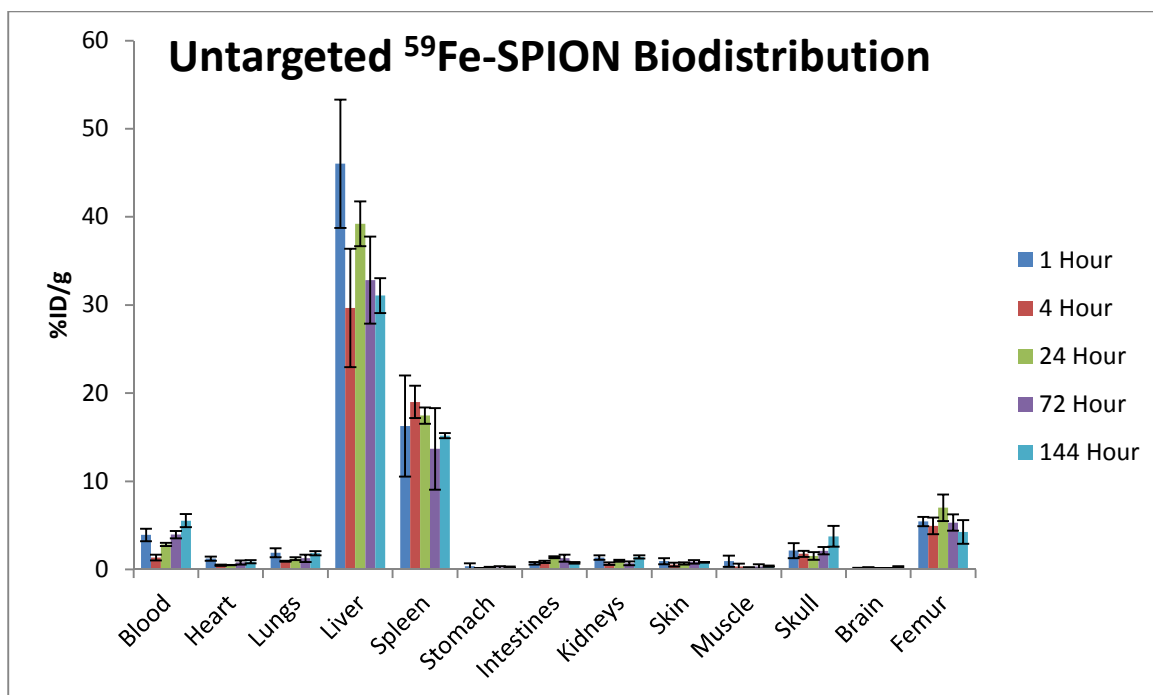


Figure 31: Biodistribution (%ID/g) at various time points post intravenous administration. Nude mice (n=3 per time point) were injected through the tail vein with ⁵⁹Fe-SPIONs (0.84±0.03 μCi; 200 μL; 26±1 μg of Fe). Tissues were collected, weighed, and the gamma emission was measured to calculate the %ID/g.

Table 9: Biodistribution of tail-vein injected ⁵⁹FeCl₃ (0.23±.3 μCi) in nude mice (n=3 per time point). Data are presented as %ID/g (mean±stdv) values determined through gamma counting. Tissues were collected, weighed, and the gamma emission was measured to calculate the %ID/g.

Organ	24 Hours	144 Hours
Blood	14±2	28±4
Heart	3±0.3	4.1±0.5
Lungs	7±1	11±3
Liver	46±8	50±10
Spleen	41±5	48±9
Stomach	4±2	1.1±0.5
Intestines	6±1	2.1±0.8
Kidneys	5.8±0.6	6.1±0.7
Skin	2.2±0.4	3.4±1
Muscle	0.9±0.1	1±0.2
Skull	5±2	10±4
Brain	0.5±0.2	1.13±0.1
Femur	21±6	10±2

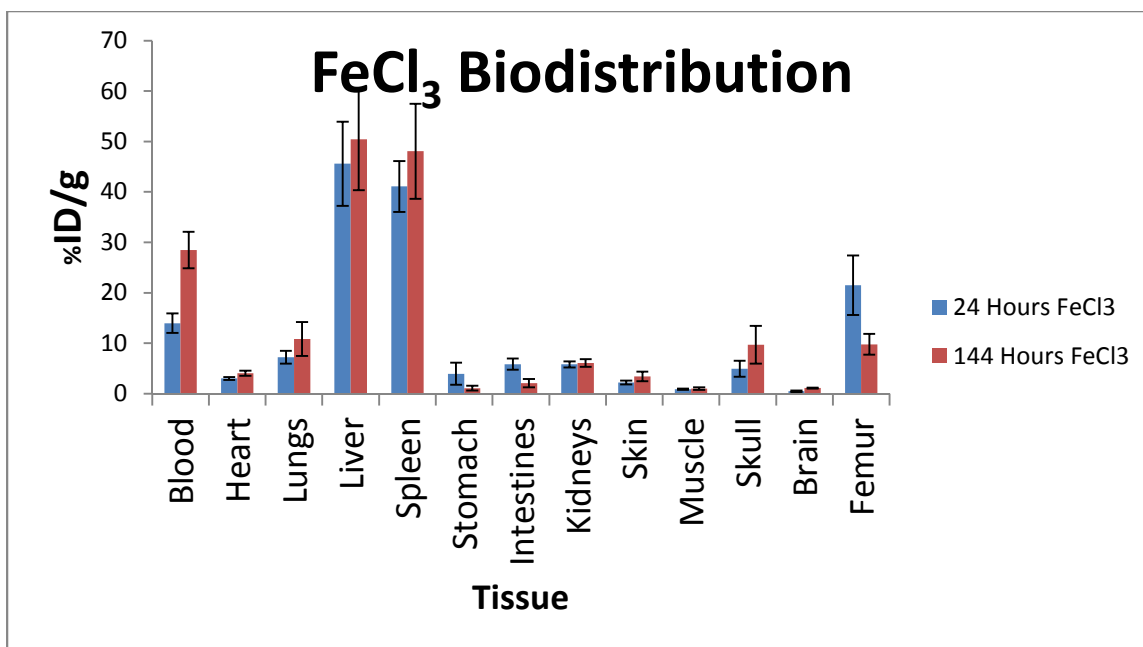


Figure 32: Biodistribution (%ID/g) at various time points post tail-vein administration ($0.23 \pm 0.03 \mu\text{Ci}$; $200 \mu\text{L}$) of $^{59}\text{FeCl}_3$. Tissues were collected, weighted, and the gamma emission was measured to calculate the %ID/g.

4.4.2. MR imaging

Representative MR images of the ^{59}Fe -SPION injected mice are shown before and at 1 hour post injection in Figure 33, at 4 hours post injection in Figure 34, at 24 hours post injection in Figure 35, at 72 hours post injection in Figure 36, and at 144 hours post injection in Figure 37. High contrast was observed in the liver, while medium contrast was observed in the kidneys, and little or no contrast was observed in the brain. ROIs were drawn on these three larger tissues, and the contrast gained by the SPION injection was quantified and compared to the ^{59}Fe -SPION biodistribution data in Figure 38. A standard curve of contrast (% Signal) versus ^{59}Fe -SPION iron concentration (mg/L) was produced and is shown in Figure 39. Concentrations between the known values were linearly interpolated, as shown by the connecting line segments. The SPION iron concentration values calculated from the MRI data and the biodistribution study are shown in Figure 40. SPION iron concentrations calculated from MRI ROI data were greater

than values calculated from the biodistribution study by a mean factor of 62 ± 38 in the liver, a factor of 3.2 ± 1.8 in the kidneys, and 0.55 ± 0.25 in the brain.

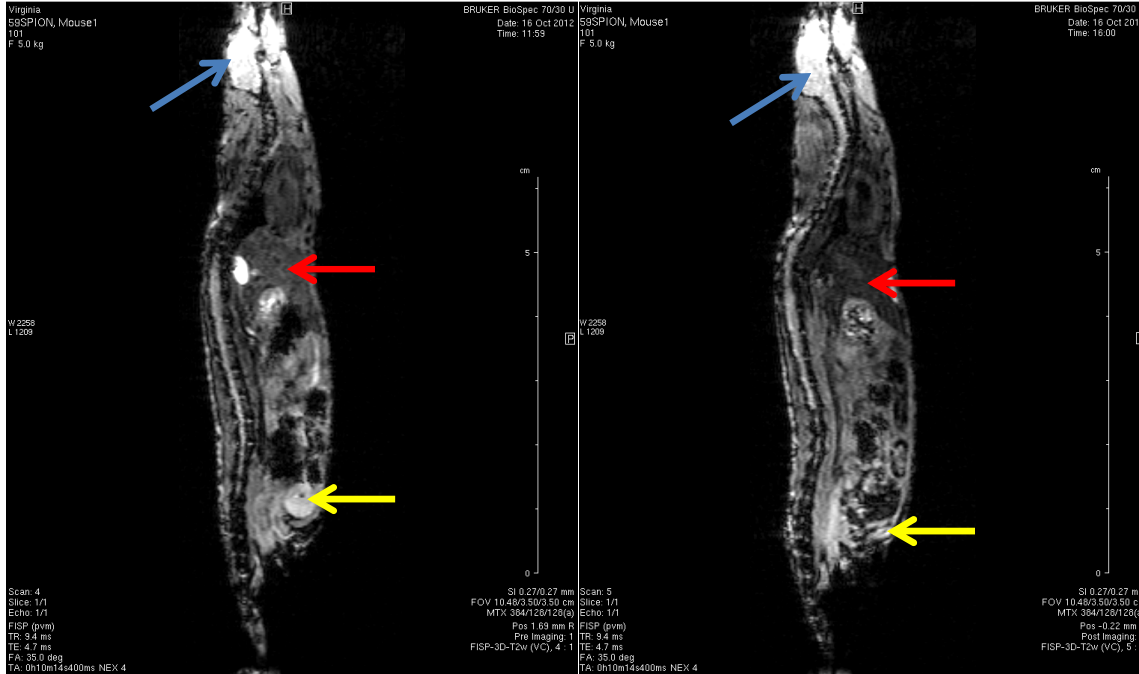


Figure 33: Sagittal MR images of ^{59}Fe -SPION (26 ± 1 μg Fe and 840 ± 30 nCi) tail-vein injected nude mouse before (left) and 1 hour (right) after injection. The mouse was imaged with a Fast Imaging with Steady State Precession (FISP) sequence with a repeat time (TR) of 9.4 ms and echo time (TE) of 4.7 ms and number of scans averaged (NSA) of 4. A flip angle (FA) of 35° was used to achieve T2*/T1 weighted images. The blue arrows indicate the brain, the red arrows indicate the liver, and the yellow arrows indicate the bladder.

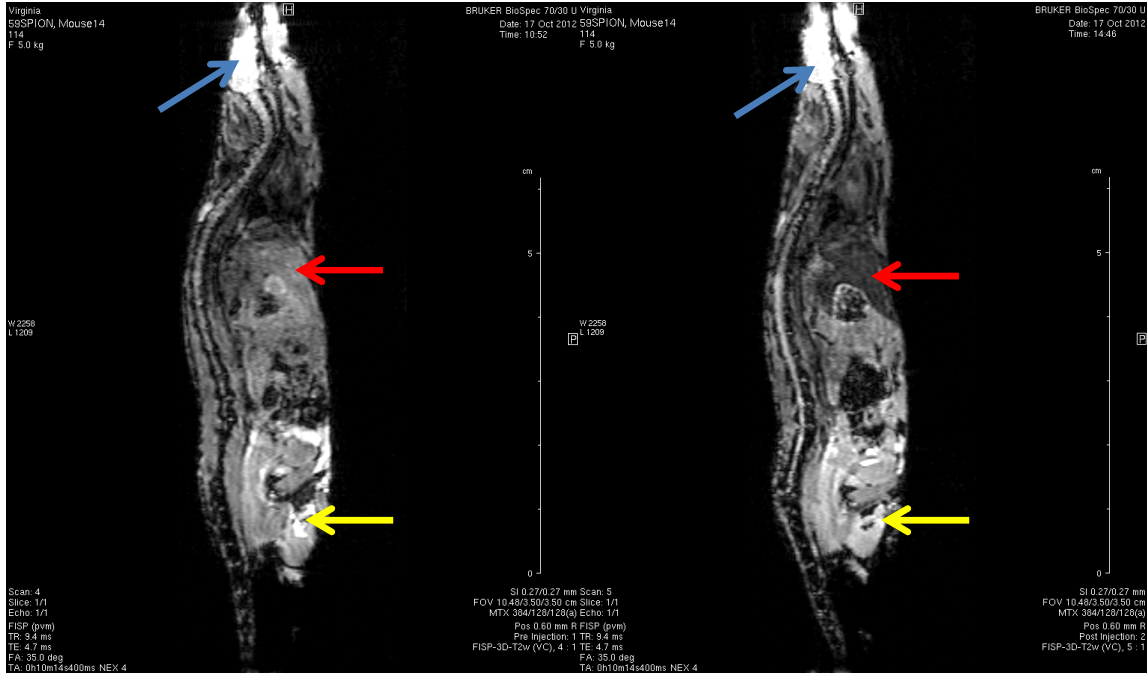


Figure 34: Sagittal MR images of ^{59}Fe -SPION ($26 \pm 1 \text{ ug Fe}$ and $840 \pm 30 \text{ nCi}$) tail-vein injected nude mouse before (left) and 4 hours (right) after injection. The mouse was imaged with a Fast Imaging with Steady State Precession (FISP) sequence with a repeat time (TR) of 9.4 ms and echo time (TE) of 4.7 ms and number of scans averaged (NSA) of 4. A flip angle (FA) of 35° was used to achieve T2*/T1 weighted images. The blue arrows indicate the brain, the red arrows indicate the liver, and the yellow arrows indicate the bladder.

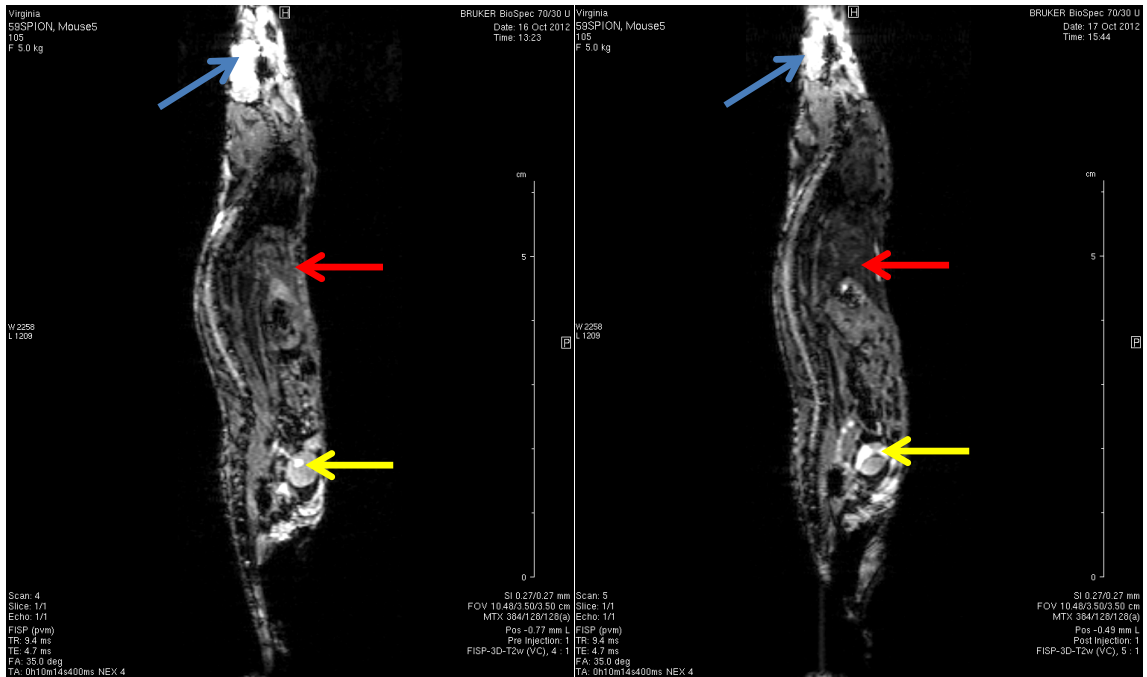


Figure 35 Sagittal MR images of ^{59}Fe -SPION ($26 \pm 1 \text{ ug Fe}$ and $840 \pm 30 \text{ nCi}$) tail-vein injected nude mouse before (left) and 24 hours (right) after injection. The mouse was imaged with a Fast Imaging with Steady State Precession (FISP) sequence with a repeat time (TR) of 9.4 ms and echo time (TE) of 4.7 ms and number of scans averaged

(NSA) of 4. A flip angle (FA) of 35° was used to achieve T2*/T1 weighted images. The blue arrows indicate the brain, the red arrows indicate the liver, and the yellow arrows indicate the bladder. averaged (NSA) of 4. A flip angle (FA) of 35° was used to achieve T2*/T1 weighted images.

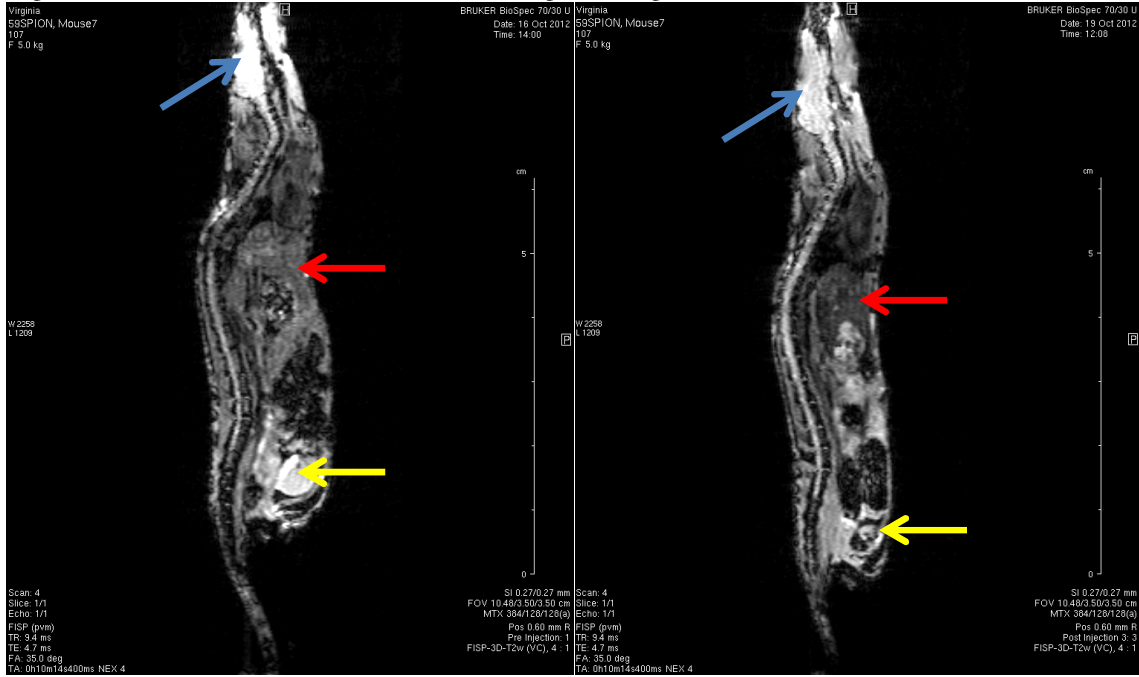


Figure 36: Sagittal MR images of ^{59}Fe -SPION ($26 \pm 1 \text{ ug Fe}$ and $840 \pm 30 \text{ nCi}$) tail-vein injected nude mouse before (left) and 72 hours (right) after injection. The mouse was imaged with a Fast Imaging with Steady State Precession (FISP) sequence with a repeat time (TR) of 9.4 ms and echo time (TE) of 4.7 ms and number of scans averaged (NSA) of 4. A flip angle (FA) of 35° was used to achieve T2*/T1 weighted images. The blue arrows indicate the brain, the red arrows indicate the liver, and the yellow arrows indicate the bladder.

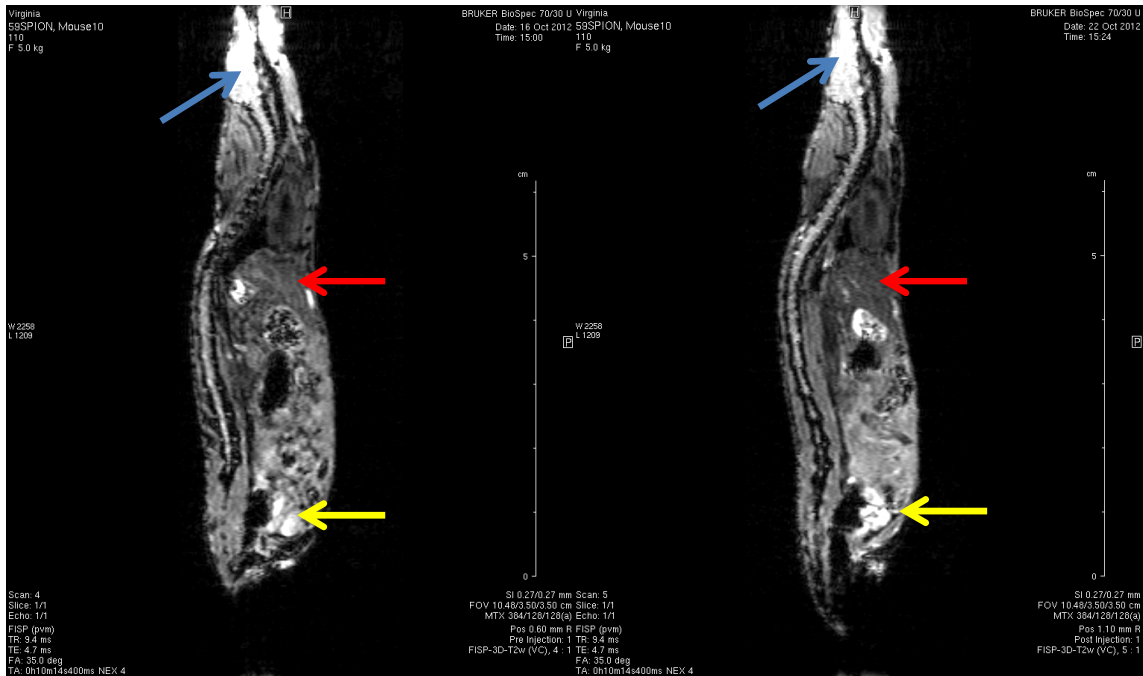


Figure 37: Sagittal MR images of ^{59}Fe -SPION ($26 \pm 1 \text{ ug Fe}$ and $840 \pm 30 \text{ nCi}$) tail-vein injected nude mouse before (left) and 144 hours (right) after injection. The mouse was imaged with a Fast Imaging with Steady State Precession (FISP) sequence with a repeat time (TR) of 9.4 ms and echo time (TE) of 4.7 ms and number of scans averaged (NSA) of 4. A flip angle (FA) of 35° was used to achieve T2*/T1 weighted images. The blue arrows indicate the brain, the red arrows indicate the liver, and the yellow arrows indicate the bladder.

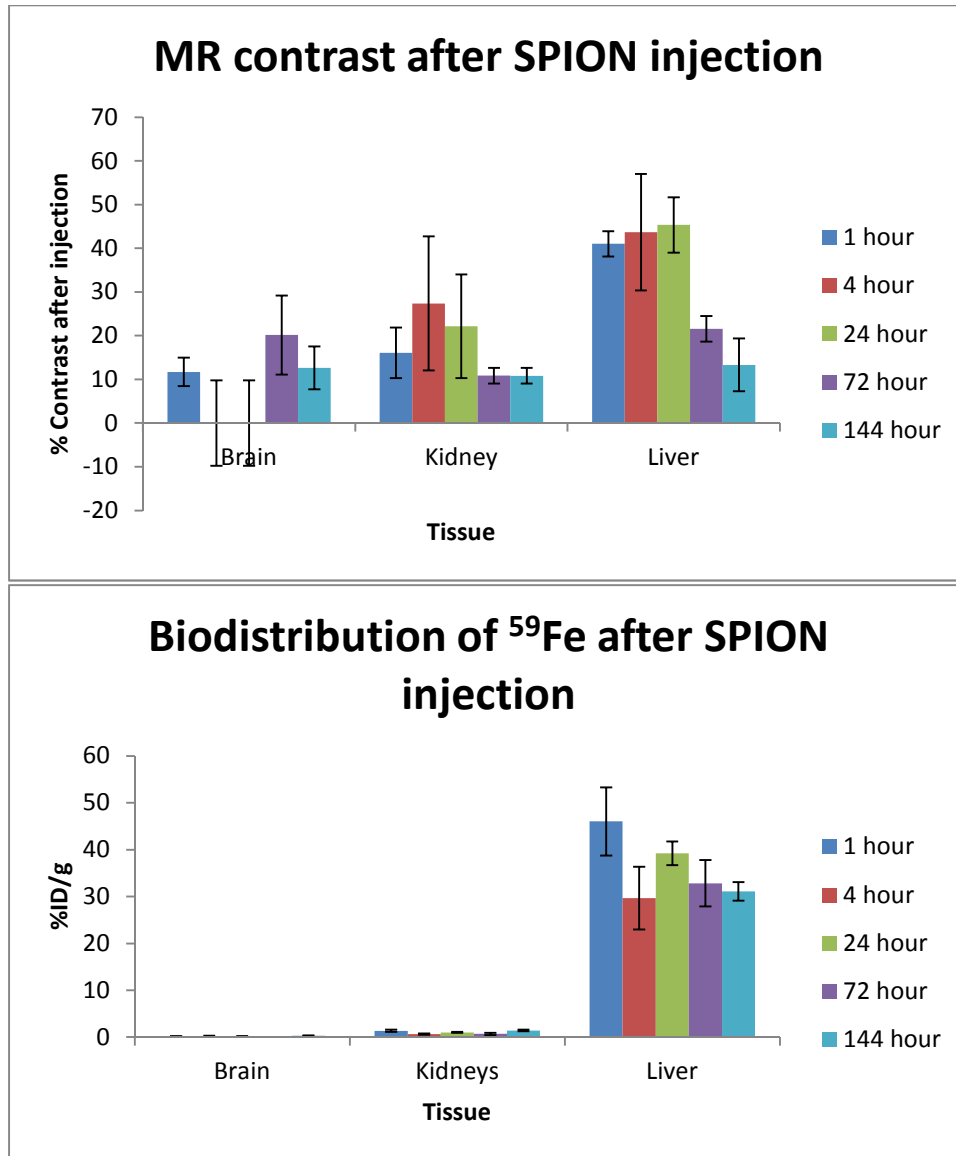


Figure 38: The MR contrast caused by the SPION injection as measured by ROI analysis of various tissues (top) and the %ID of those tissues from the biodistribution (below) for comparison. Mice were tail-vein injected with ⁵⁹Fe-SPION (26 ± 1 ug Fe and 840 ± 30 nCi) and imaged and sacrificed at different time points.

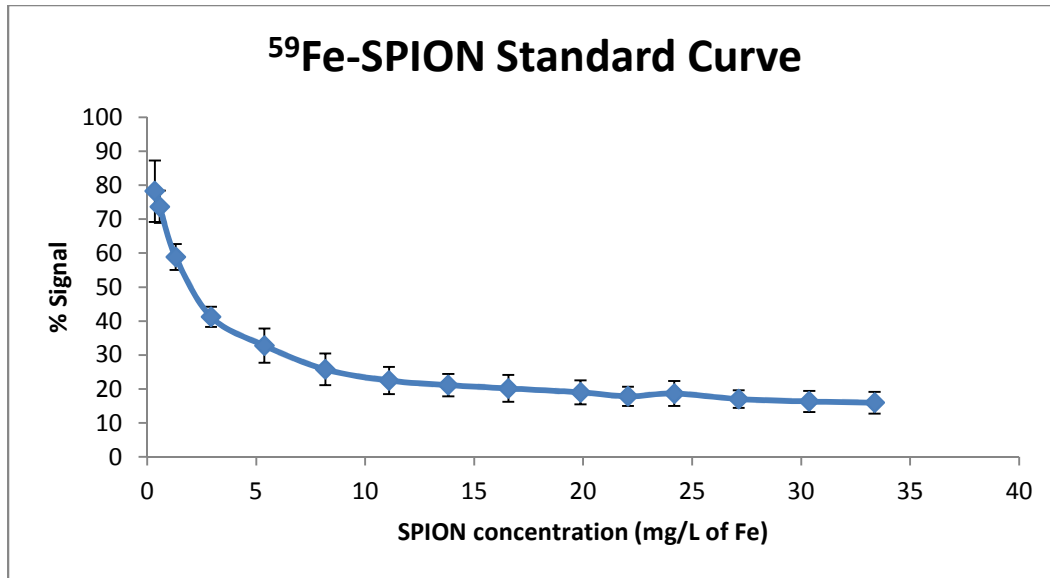


Figure 39: The standard curve of the % signal contrast versus ^{59}Fe -SPION iron concentration. The connecting line segments represent the linear interpolation used to evaluate values between the known concentrations. The phantom was imaged with a Fast Imaging with Steady State Precession (FISP) sequence with a repeat time (TR) of 9.4 ms and echo time (TE) of 4.7 ms and number of scans averaged (NSA) of 4. A flip angle (FA) of 35° was used to achieve T2*/T1 weighted images.

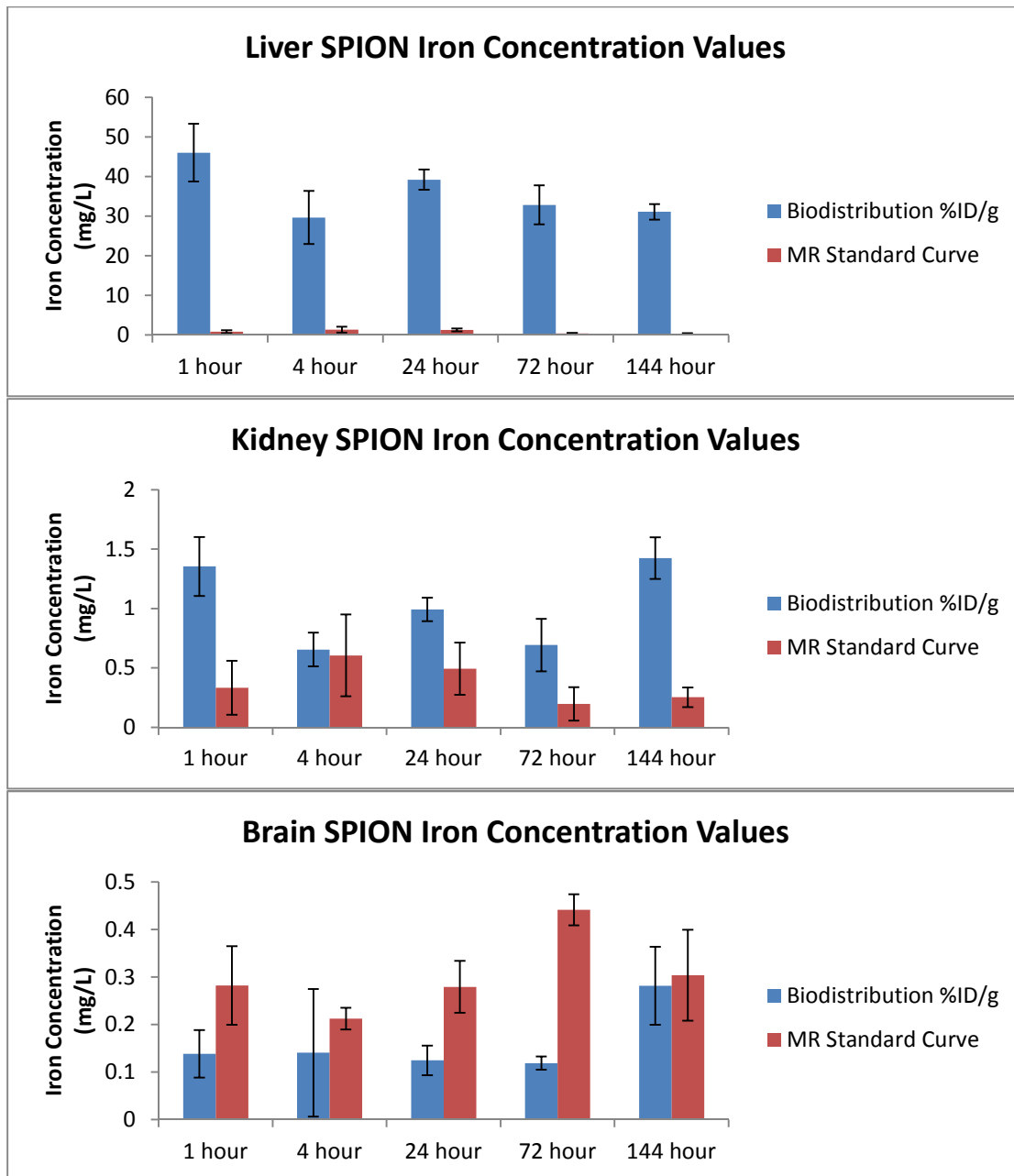


Figure 40: SPION iron concentration values are calculated from MRI ROI data and ^{59}Fe -SPION biodistribution %ID/g values for the liver (top), kidney (middle), and brain (bottom). Mice were tail-vein injected with ^{59}Fe -SPION (26 ± 1 ug Fe and 840 ± 30 nCi) and imaged and sacrificed at different time points.

The large discrepancy in the liver between the %ID/g values and the MR standard curve values may be a result of the fact that the % contrast induced by the nanoparticles plateaus at higher concentrations, and the liver has high uptake. Additionally, the % contrast depends on the interaction between the SPIONs and the surrounding hydrogen nuclei. This interaction can be

affected by a number of factors, including the cellular and sub-cellular localization of the SPIONs, the temperature of the tissue, and the surrounding of the nanoparticles with proteins. These variables and the results shown here indicate the difficulties measuring probe concentration from MR data. This challenge shows a potential strength of a hybrid PET/MRI nanoparticle, where probe concentration information is derived from PET data, while MR data is used for spatial information.

4.4.3. Signal contrast mapping

A representative signal contrast map is shown in Figure 41. The left image shows the central sagittal slice of the mouse before ^{59}Fe -SPION injection. The center image shows the mouse 24 hours post-injection and the right image is the % contrast map produced from the post and pre-injection images. The central slice shows contrast in the liver and back bones. Other slices show contrast in the kidneys. No contrast is seen in the intestines, stomach, or brain.

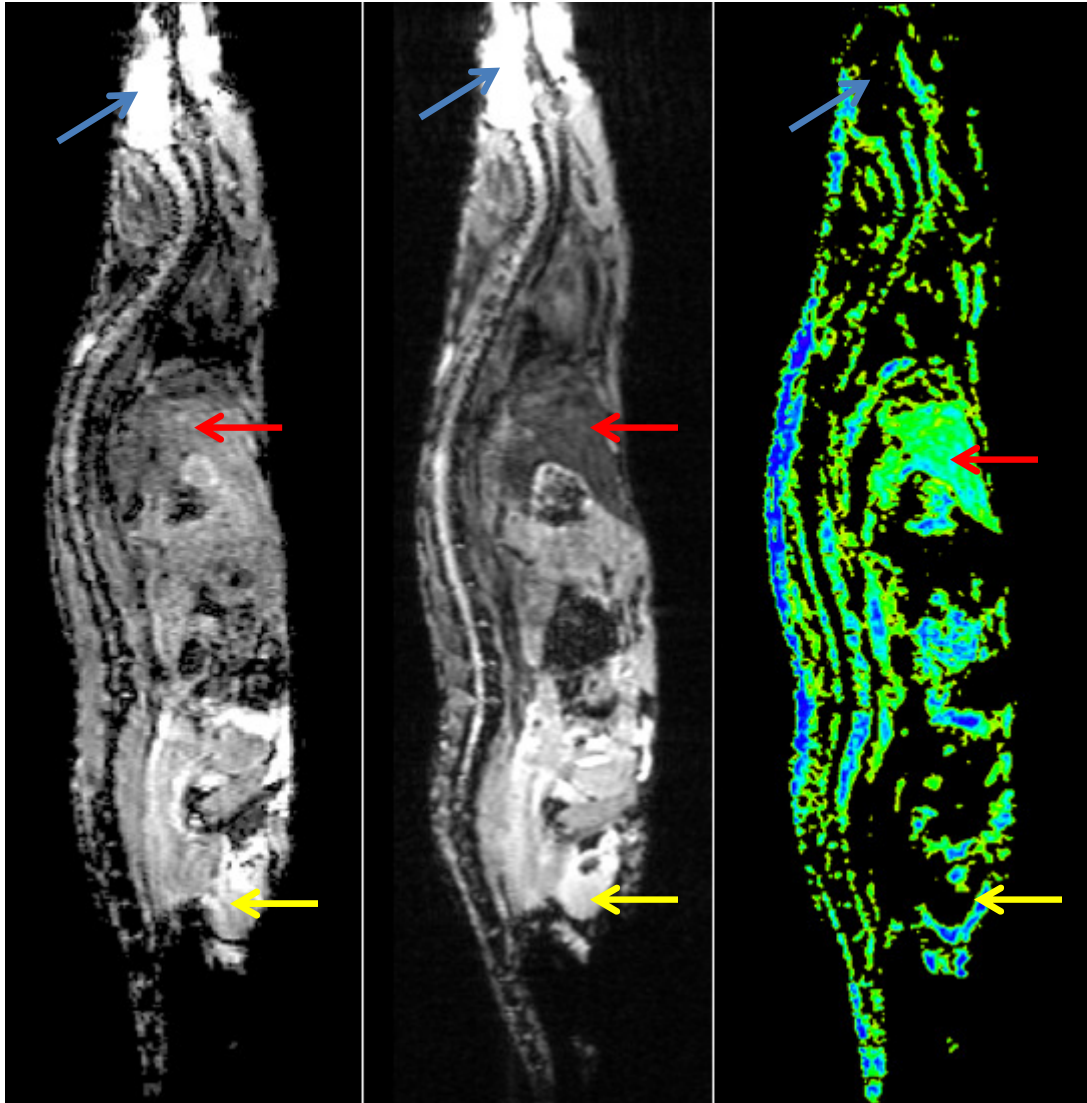


Figure 41: ^{59}Fe -SPIONs ($26 \pm 1 \text{ ug Fe}$ and $840 \pm 30 \text{ nCi}$) tail-vein injected nude mouse before (left) and 24 hours (middle) after injection. The mouse was imaged with a Fast Imaging with Steady State Precession (FISP) sequence with a repeat time (TR) of 9.4 ms and echo time (TE) of 4.7 ms and number of scans averaged (NSA) of 4. A flip angle (FA) of 35° was used to achieve T2*/T1 weighted images. The blue arrows indicate the brain, the red arrows indicate the liver, and the yellow arrows indicate the bladder. The right image shows the % contrast map, calculated by the difference of the before and after (deformably co-registered) images, divided by the before injection image.

Chapter 5

5. [⁵²Mn]-MION-cRGD Evaluation

To demonstrate the use of hybrid PET/MRI nanoparticle in targeted molecular imaging, the [⁵²Mn]-MION-cRGDs were utilized to image nude mice bearing U87MG xenograft tumors. As a precursor to this study, the PET characteristics of spatial resolution, sensitivity, and count rate linearity, for ⁵²Mn and two other imaging radionuclides were characterized in a small animal PET/SPECT/CT scanner (Inveon, Erlangen, Germany). For all PET studies, signal was acquired within a 350 - 650 keV energy window, and images were reconstructed with the 3D-OSEM+MAP reconstruction algorithm (0.78 mm voxel size), except for images used for spatial resolution measurements, which were reconstructed with the filtered back projection algorithm (0.39 mm voxel size). Additionally, the $\alpha_v\beta_3$ integrin expression of the U87MG cells before and after implantation was characterized using fluorescent anti-body staining and flow cytometry.

5.1. PET characterization of imaging radionuclides

The physical decay characteristics of every imaging radionuclide affect the image quality of that radionuclide. Specifically, the positron decay energy will affect the image spatial resolution, while additional gamma rays produced by non-pure positron emitting radionuclides may change sensitivity and count rate linearity. In order to assess these effects, the spatial resolution, sensitivity, and count rate linearity of ⁵²Mn, ¹⁸F and ⁸⁹Zr were measured with a small animal PET/SPECT/CT scanner. The methods used to assess each characteristic are described in the following three sections.

5.1.1. Spatial Resolution

The spatial resolution of each radionuclide was assessed by loading a thin tube, with inner diameter of 0.39 mm, with 5-27 μCi of the imaging radionuclide. This tube was placed within an acrylic glass phantom shown in Figure 42. The phantom has four bores, which act as four positions of the radionuclide during scanning. The central bore was placed to cover the scanner isocenter. The phantom was imaged with the PET scanner long enough to acquire 100 million counts. For spatial resolution measurements, images were reconstruction using a filtered back projection algorithm and a 0.78 mm voxel size. The full width at half maximum (FWHM) of the signal from each position was measured using AMIDE, a medical imaging data examining software.⁶⁹ This measurement was repeated ten times for each position and the standard deviation of the measurement was used to assess uncertainty.

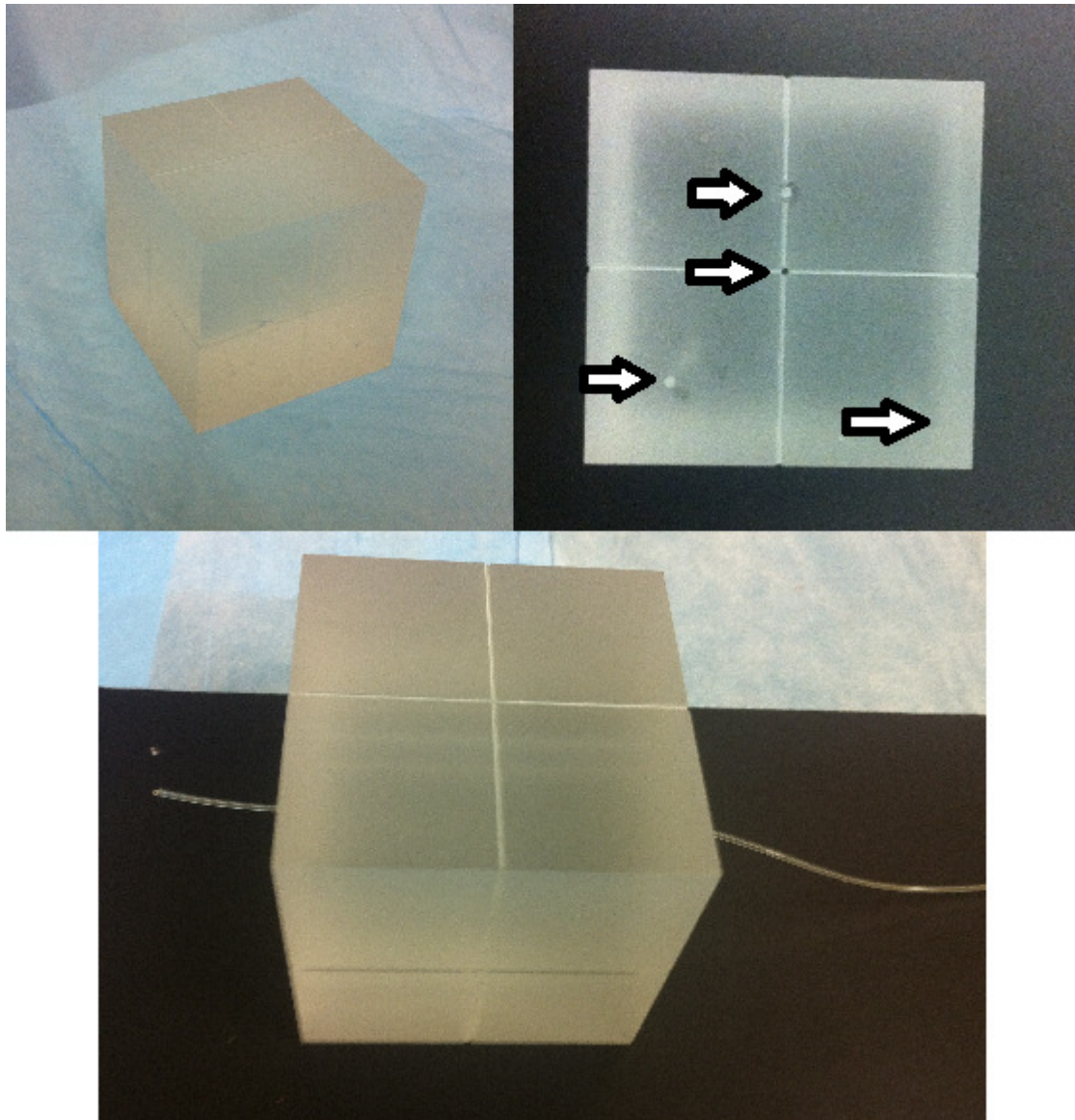


Figure 42: The acrylic glass cube functions as a phantom, holding the radionuclide loaded tube at four positions within the scanner. The cube is 5 cm in each dimension and has a density of $1.13 \pm 0.05 \text{ g/cm}^3$. The bores within the block, shown in the top right, are displaced by 0 mm \times 0 mm, 0 mm \times 10 mm, 15 mm \times 15 mm, and 20 mm \times 20 mm. The tube goes through the bores, as shown (bottom).

5.1.2. Sensitivity Measurement

The assessment of sensitivity (counts/decay) was accomplished by loading a 16.8 mL vial with known activities of the radionuclide. Before scanning, the activity of each vial was measured with a re-entrant ionization chamber or “dose calibrator” (Capintec, Ramsey, NJ, USA). The ionization chamber was calibrated with a known activity ^{52}Mn , ^{18}F and ^{89}Zr . These known

activities were measured with the high purity Ge gamma spectrometer, described in Section 3.2.3. The 16.8 mL vial phantom, shown in Figure 43, was then imaged for 5 minutes with the small animal PET scanner. The phantom approximated the size of the mice to be used later for the imagine study, and were positioned within the scanner to approximate the mice's positions.

The number of true counts was then compared to the known activity and the sensitivity was calculated. This measurement was done with ten known activities for ^{52}Mn and ^{89}Zr , and 34 known activities for ^{18}F . The activities used covered the range from 5 μCi to 500 μCi , which included the range of activities that would be used in the animal imaging experiments. The standard deviation of the measurements was calculated and used to assess the measurement's uncertainty. The scanner efficiency (counts/positron decay) was also calculated, by dividing the sensitivity by the positron yield of each radionuclide.



Figure 43: Radionuclide filled vial, containing 16.8 mL of water. This vial serves as a phantom for sensitivity and count rate linearity measurements for ^{52}Mn , ^{18}F , and ^{89}Zr .

5.1.3. Count Rate Linearity

In order to measure the count rate linearity of ^{52}Mn , ^{18}F and ^{89}Zr , the same phantoms described in Section 5.1.2 were utilized. Known activities ranging from $>500\ \mu\text{Ci}$ to $<5\ \mu\text{Ci}$ were used because this covered the range of activities that would be used in the mouse imaging study. Each sample was PET imaged for 5 minutes and the number of true counts was plotted as a function of the known activity. This plot was then fitted with a linear regression and the R^2 value was calculated to evaluate the linearity of the response.

5.1.4. ^{18}F Characterization

The PET imaging characteristics of ^{18}F , a widely used PET radionuclide, were assessed. ^{18}F has 110 minute half-life, a positron yield of 96.7%, and mean positron energy of 250 keV. The spatial resolution of ^{18}F measured at the four positions is shown in Table 10.

Table 10: The full width at half maximum of the reconstructed ^{18}F spatial resolution phantom image at different offsets from the PET scanner isocenter.

Position Offset	Full width at half maximum (mm)
0 mm × 0 mm	2.01 ± 0.03
0 mm × 10 mm	2.03 ± 0.05
15 mm × 15 mm	2.09 ± 0.02
20 mm × 20 mm	2.32 ± 0.02

The sensitivity of ^{18}F with the Inveon PET/SPECT/CT scanner in the geometry previously described was measured to be 0.036 ± 0.002 counts/decay. After correcting for the positron yield, this gave an efficiency of 0.037 ± 0.002 counts/positron. Finally, the count rate linearity was fitted with a linear regression, as shown in Figure 44, with $R^2 = 0.9984$. These values are comparable to those measured by Visser and colleagues on the Inveon system.⁷⁰

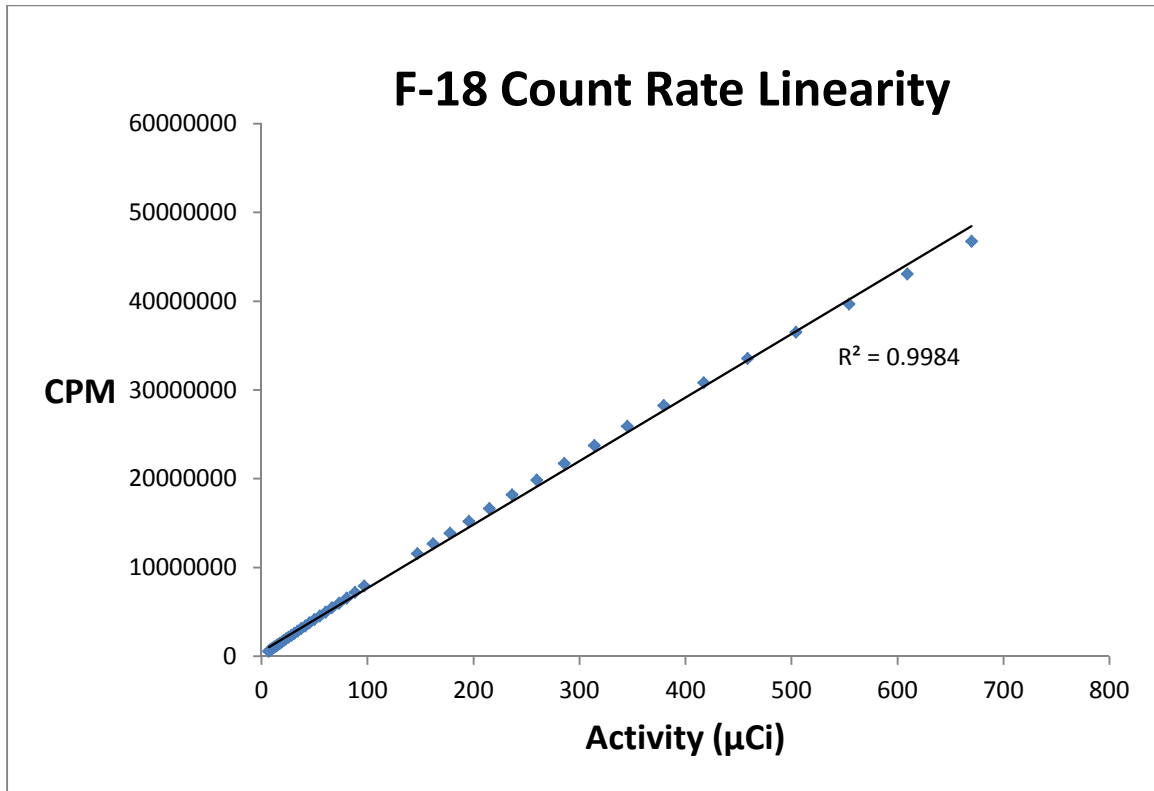


Figure 44: The count rate linearity of ^{18}F was assessed by plotting the observed counts versus the known activity in the phantom. The 16.9 mL phantom was imaged with a small animal PET scanner for 5 minutes at each activity with a 350 - 650 keV energy window.

5.1.5. ^{89}Zr Characterization

^{89}Zr has 78.4 hour half-life, a positron yield of 22.7%, and mean positron energy of 395.5 keV.

The PET imaging characteristics of ^{89}Zr were assessed because it has higher positron energy than ^{18}F , so the change in spatial resolution should be observed. Additionally, it has a different positron yield than ^{18}F , so a different sensitivity should also be measured. The spatial resolution of ^{89}Zr measured at the four positions is shown in Table 11. These values were comparable to those previously reported by Disselhorst.⁷¹

Table 11: The full width at half maximum of the reconstructed ^{89}Zr spatial resolution phantom image at different offsets from the PET scanner isocenter.

Position Offset	Full width at half maximum (mm)
0 mm × 0 mm	2.10 ± 0.06
0 mm × 10 mm	2.11 ± 0.08
15 mm × 15 mm	2.23 ± 0.09
20 mm × 20 mm	2.40 ± 0.11

The sensitivity of ^{89}Zr with the Inveon PET/SPECT/CT scanner in the geometry previously described was measured to be 0.008 ± 0.001 counts/decay. After correcting for the positron yield, this resulted in an efficiency of 0.035 ± 0.005 counts/positron, which was similar to that measured for ^{18}F . Finally, the count rate linearity was fitted with a linear regression, as shown in Figure 45, with $R^2 = 0.9807$.

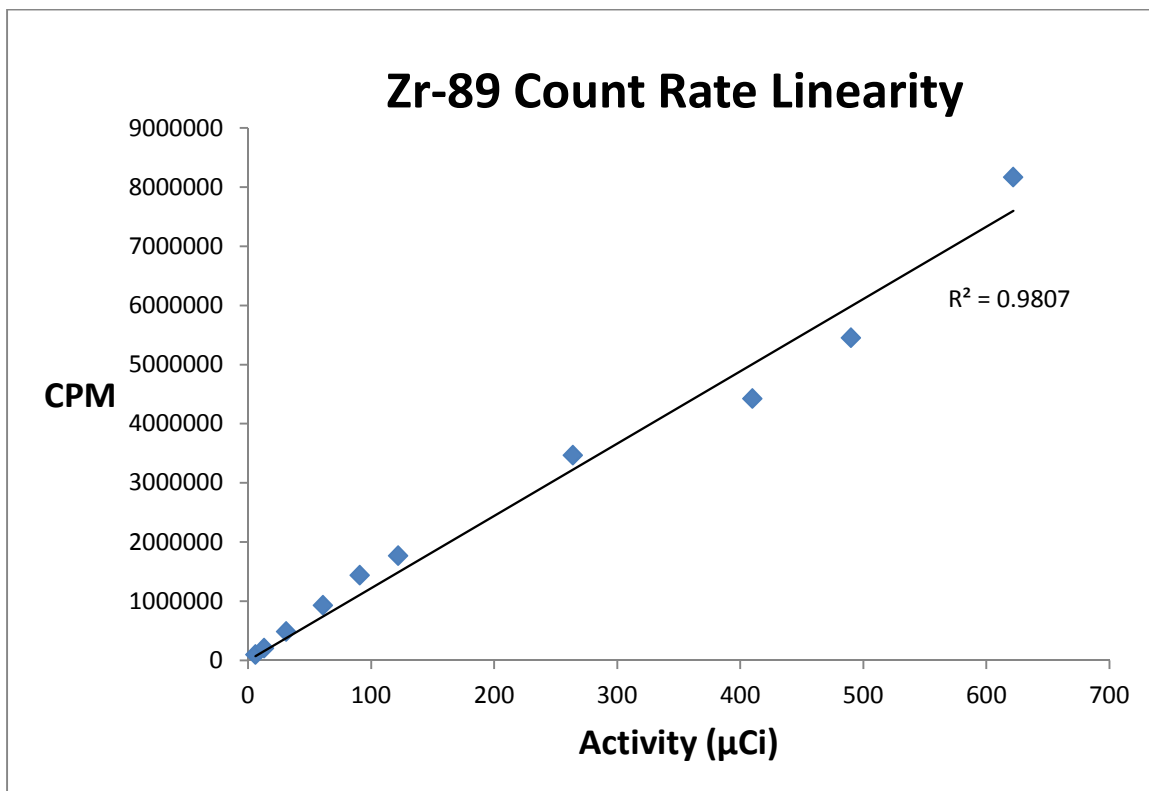


Figure 45: The count rate linearity of ^{89}Zr was assessed by plotting the observed counts versus the known activity in the phantom. The 16.9 mL phantom was imaged with a small animal PET scanner for 5 minutes with a 350 - 650 keV energy window.

5.1.6. ^{52}Mn Characterization

^{52}Mn has 5.59 day half-life, a positron yield of 29.6%, and mean positron energy of 241.6 keV.

The spatial resolution of ^{52}Mn measured at the four phantom bore positions is shown in Table 12.

The measured values are similar to those reported for ^{52}Mn by Topping.⁷²

Table 12: The full width at half maximum of the reconstructed ^{52}Mn spatial resolution phantom image at different offsets from the PET scanner isocenter.

Position Offset	Full width at half maximum (mm)
0 mm × 0 mm	1.96 ± 0.08
0 mm × 10 mm	1.96 ± 0.16
15 mm × 15 mm	2.01 ± 0.08
20 mm × 20 mm	2.23 ± 0.14

The sensitivity of ^{52}Mn with the Inveon PET/SPECT/CT scanner in the geometry previously described was measured to be 0.0104 ± 0.0008 counts/decay. After correcting for the positron yield, this resulted in an efficiency of 0.035 ± 0.003 counts/positron, which was similar to that measured for the other imaging radionuclides. Finally, the count rate linearity was fitted with a linear regression, as shown in, with $R^2 = 0.998$.

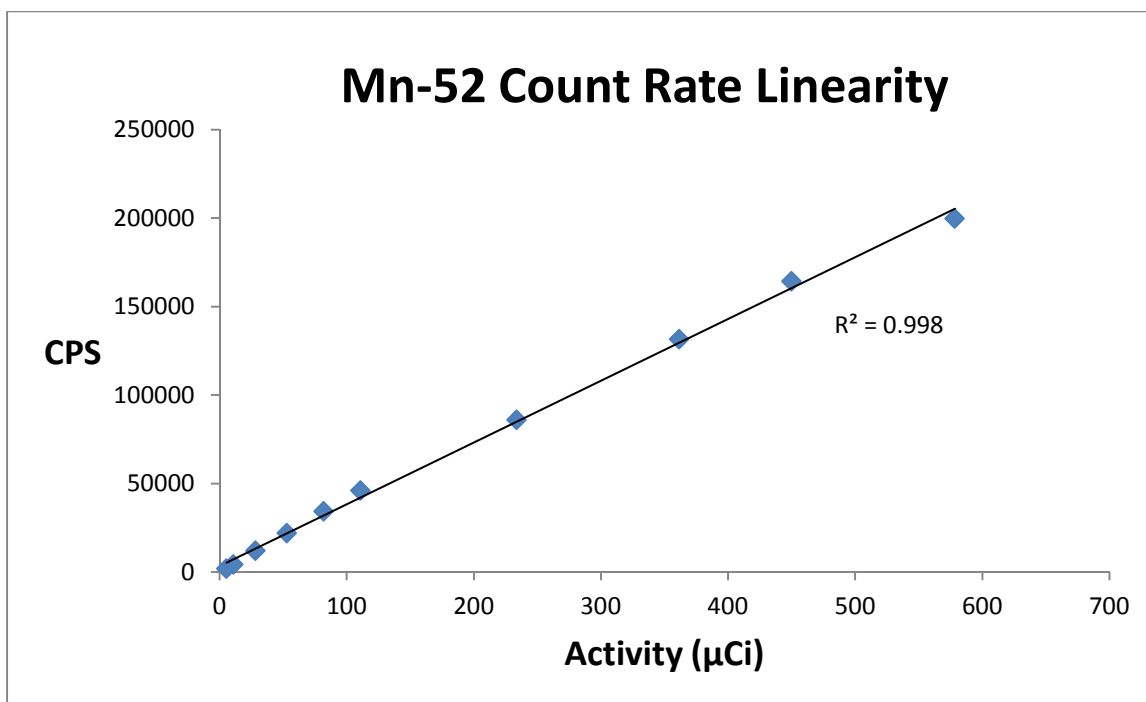


Figure 46: The count rate linearity of ^{52}Mn was assessed by plotting the observed counts versus the known activity in the phantom. The 16.9 mL phantom was imaged with a small animal PET scanner for 5 minutes with a 350 - 650 keV energy window.

5.2. Hybrid PET/MR Imaging of U87-MG Tumor Bearing Mice

To demonstrate the multi-modal use of the ^{52}Mn -MIONs developed in Section 3.2, the ^{52}Mn -MION-cRGDs were utilized to image nude mice bearing U87MG xenograft tumors. The $\alpha_v\beta_3$ integrin expression was first characterized using fluorescent anti-body staining and flow cytometry. Then the binding of the ^{52}Mn -MION-cRGDs to the $\alpha_v\beta_3$ integrin was demonstrated through a solid phase assay.

5.2.1. Hybrid PET/MRI phantom study

To observe and compare the PET and MRI signals from ^{52}Mn -MIONs, a phantom was made with 15 vials of known concentrations and activities of ^{52}Mn -MIONs. It was MR and PET imaged, then resulting PET signal and MR contrast was quantified. The MRI sequence used to image the phantom, was the same described in Section 4.2, and used for all animal MRI studies.

Each vials signal and contrast was plotted as a function of the probe concentration. The MR and PET images are shown in Figure 47 and the quantification of the PET and MR signals are shown in Figure 48. The PET signal scales linearly with probe concentration and activity ($R^2 = 0.9975$), unlike the MR contrast, which stops increasing at high $[^{52}\text{Mn}]$ -MION concentrations. This indicates that the PET signal is better to use for MION concentration quantification than MR contrast.

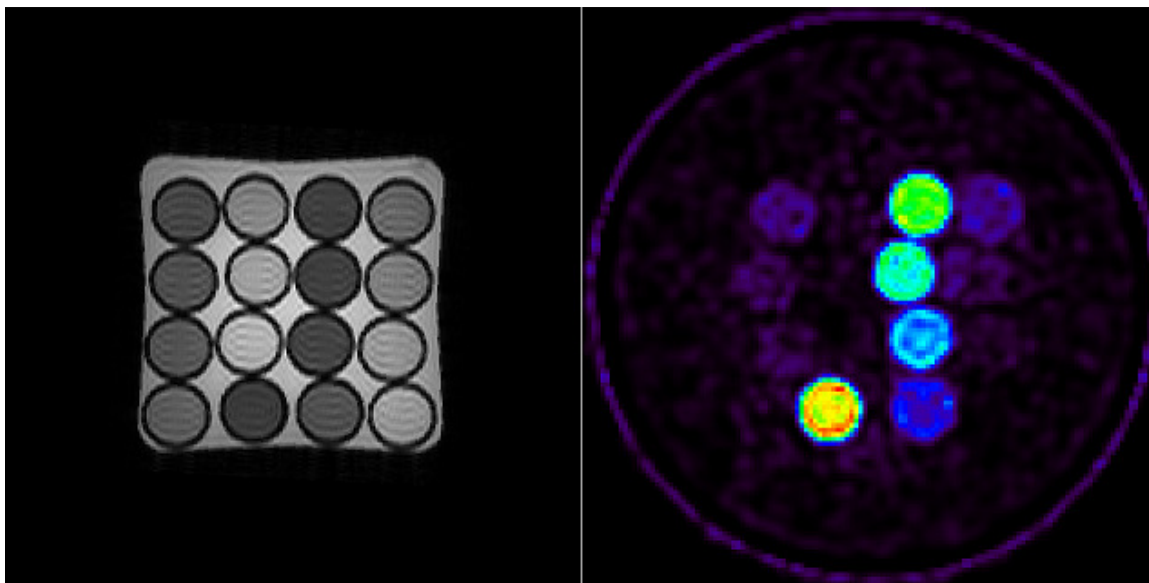


Figure 47: $[^{52}\text{Mn}]$ -MION loaded phantom was imaged with MRI and PET. The known probe concentrations gave MR contrast (left) and PET signal (right). Two different $[^{52}\text{Mn}]$ -MIONs are in the phantom. Low activity (left part of the phantom) and high activity (right part of the phantom). The ringing artefact seen in the MR image is a result of the sharp discontinuity between the plastic of the vial and the water in each phantom and the finite number of harmonics used in the fourier series in image reconstruction, as known as the “Gibbs phenomenon.” It does not affect the ROI values, as long as the ROI covers a large area of the vial.

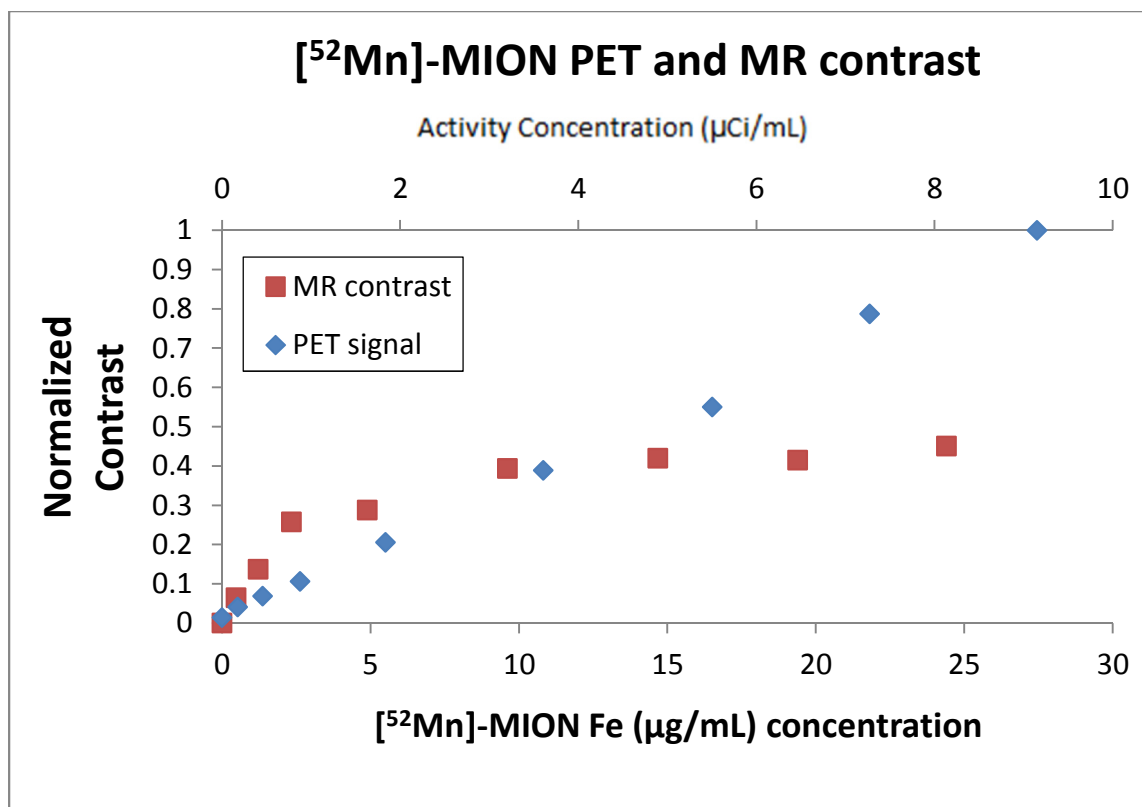


Figure 48: The MR contrast (red) and PET signal (blue) of a [⁵²Mn]-MIONs loaded phantom. The high activity [⁵²Mn]-MION vials shown in Figure 47 were quantified. The PET signal increases linearly with probe concentration, unlike the MR contrast which stops increasing at high MION concentrations.

5.2.2. U87MG tumor model

The U87MG human primary glioblastoma cell line is known to express $\alpha_v\beta_3$ integrin and has been utilized in previous $\alpha_v\beta_3$ integrin imaging studies using RGD peptide.^{73,74,75,76} Parental human glioblastoma U87MG cells were obtained from American Type Culture Collection (Manassas, VA, USA). The cells were cultured in Eagle's minimum essential medium (EMEM) containing 10% FBS, 100 U/ml penicillin, and 100 ug/ml streptomycin. The cells were propagated at 37° Celsius in a 5% carbon dioxide atmosphere. Xenografts were implanted by subcutaneous injection of 2.5 million cells into the right shoulder of 6 week old female athymic nude mice.

Before implantation, the expression of $\alpha_v\beta_3$ integrin of the U87MG cells was assessed with a fluorescent labeled antibody by flow cytometry, as described below:

- (1) 1×10^6 U87MG cells were collected and washed with PBS three times.
- (2) The cells were resuspended in 100 μ l of PBS/BSA/Azide staining buffer and incubated with 2 μ L of Fc blocker (BD Pharmingen, San Jose, Ca) on ice, to prevent non-specific binding of the anti-body.
- (3) The cells were incubated for 20 minutes with 2 μ g of human integrin $\alpha_v\beta_3$ anti-body labeled with Alexa Fluor 488 (R&D Systems, Minneapolis, Mn)
- (4) The cells were washed three times with staining buffer.
- (5) The cells were resuspended in 1 ml of staining buffer and analyzed by flow cytometer.
- (6) The fluorescence signal of 50,000 cells was analyzed on a cell by cell basis using FACSCalibur (BD Pharmingen, San Jose, Ca).

After the imaging study, the tumor xenografts were resected. Tumors were cut into small pieces and digested using triple enzyme mix in Hank's balanced salt solution (Life Technologies, Grand Island, NY) for 1 hr. The digested tissues were passed through a cell strainer to obtain single cell suspension. These cells were stained and analyzed for human integrin $\alpha_v\beta_3$, as described above. This further verified the $\alpha_v\beta_3$ integrin expression *in vivo*. Cells were recovered by homogenizing the tumor tissue. In flow cytometry, light scattered by the cell forward (FSC), corresponds to cell volume. Light scattered by the cell to the side (SSC) corresponds to the cell's inner complexity or granularity. During flow cytometry analysis, a gate was created to include the relatively large complex living tumor cells, and exclude apoptotic bodies and, in the case of the recovered tumor cells, any non-U87MG cells also recovered. Representative gates are shown in Figure 49.

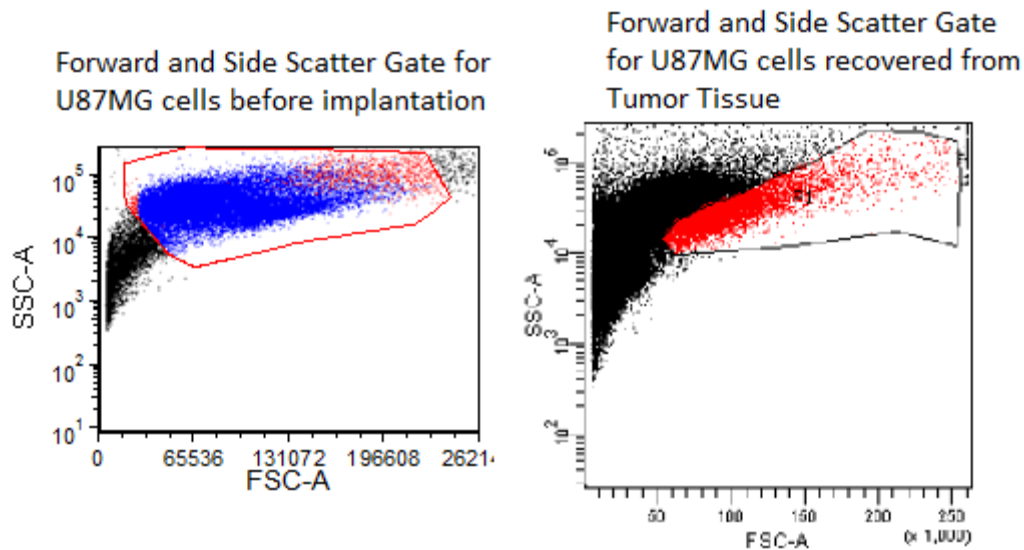


Figure 49: The U87MG cells analyzed with flow cytometry were gated to select mainly living U87MG cells, and exclude apoptotic bodies and other cells recovered from tumor tissue.

The result from the flow cytometry analysis of the U87MG cells before implantation is shown in Figure 50. The antibody stained cells are compared to unstained cells, and cells incubated with and isotype negative control. The isotype negative control is a fluorescently labeled protein that does not have a cellular target, showing the extent of non-specific binding. MCF-7 human breast cancer cells, known not to express $\alpha_v\beta_3$ integrin, were also used as a negative control to show the specificity of the antibody staining. These cells were grown and analyzed in the same fashion as the U87MG cells. The results of the flow cytometry analysis of the U87MG cells recovered from the tumor xenografts are shown in Figure 51. The histogram reveal, an increase in mean fluorescent intensity of U87MG cells stained with $\alpha_v\beta_3$ antibody compared to unstained and isotype negative control stain both before implantation and after recovery from tumor tissues. This indicates that the $\alpha_v\beta_3$ integrin is expressed on the U87MG cells *in vitro* and *in vivo*. Therefore, U87MG tumors were verified as appropriate for molecular imaging studies targeting

the $\alpha_v\beta_3$ integrin.

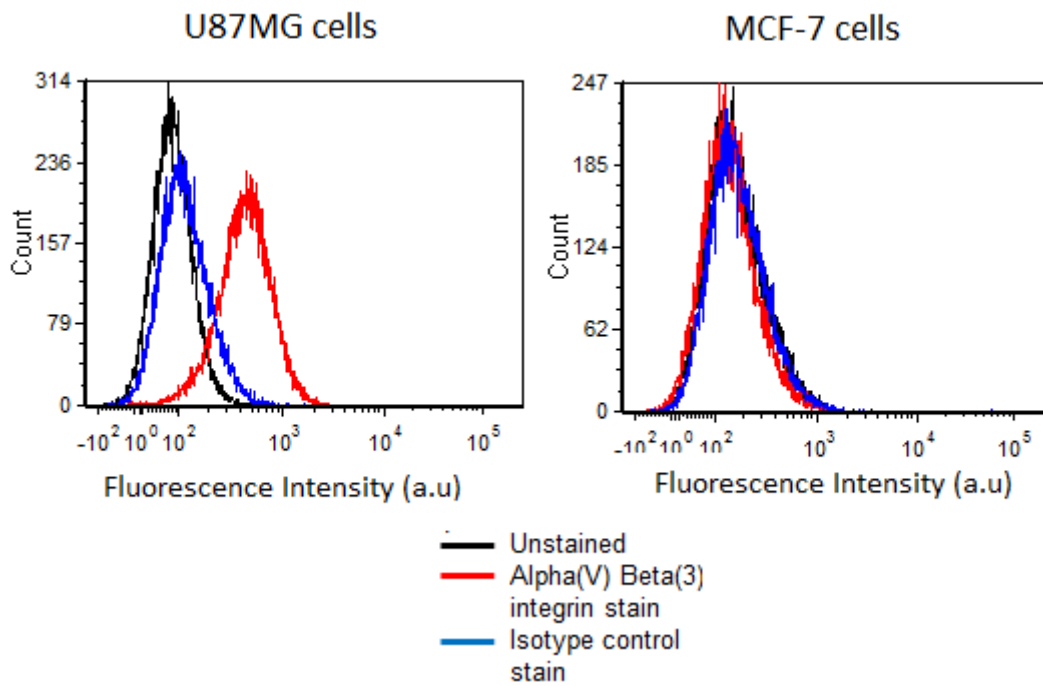


Figure 50: Flow cytometry results of U87MG and MCF-7 cells before implantation as xenograft tumors in nude mice. U87MG cells show increased fluorescence with the $\alpha_v\beta_3$ antibody stain compared to unstained and isotype negative control stain, indicating that the $\alpha_v\beta_3$ integrin is expressed on the U87MG cells. The MCF-7 cells do not show a shift in fluorescence intensity, indicating a lack of $\alpha_v\beta_3$ integrin expression.

Flow Cytometry Results from Recovered U87MG Tumor Cells

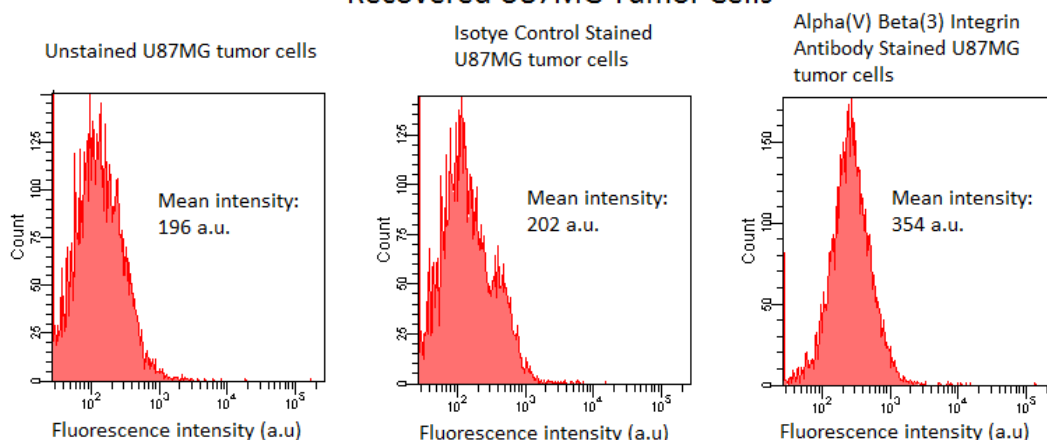


Figure 51: Flow cytometry results of U87MG cells recovered from xenograft tumors used for the hybrid imaging study. The increased mean fluorescence intensity of the $\alpha_V\beta_3$ antibody stained cells compared to the unstained and isotype control stained cells indicates that the U87MG cells are expressing $\alpha_V\beta_3$ integrin *in vivo*.

5.2.3. Assessment of $\alpha_V\beta_3$ Integrin Binding

In order to evaluate the binding of cRGD and cRGD conjugated nanoparticles to the $\alpha_V\beta_3$ integrin in isolation, a solid phase binding assay was developed. Purified $\alpha_V\beta_3$ integrin

(eBioscience, Inc., San Diego, CA) was coated onto flexible 96 well plates as described below:

- (1) The wells of a flexible 96 well plate were coated with 100 μ L of recombinant human integrin $\alpha_V\beta_3$ in duplicates at various integrin concentrations (4 μ g/mL, 2 μ g/mL, 1 μ g/mL, and uncoated) dissolved in one of three coating buffers (PBS, 1 mM $MgCl_2$ in PBS, or Tris NaCl Buffer).
- (2) The plate was sealed and incubated overnight at 4°C.
- (3) The unbound integrin containing buffer was removed from the wells.
- (4) The wells were washed three times with wash buffer (0.005% Tween 20 in PBS (pH7.2-7.4)).
- (5) The wells were loaded with 220 μ L of blocking buffer (3% BSA in PBS) and incubate at room temperature for 2 hours.
- (6) The blocking buffer was discarded and the wells were washed three times with wash buffer.

To determine the effectiveness of each coating buffer and integrin concentration sufficient to coat the wells and to establish the binding of cRGD with $\alpha_V\beta_3$ integrin, the wells were then loaded with biotinylated cRGD (Peptides International, Louisville, KY). This was followed by

incubation with StreptavidinPE (eBioscience, Inc., San Diego, CA), which is a fluorescent dye with established binding with biotin. This process is described below:

- (1) The wells were loaded with an excess (100 μL of 1 $\mu\text{g}/\text{mL}$) of biotinylated cRGD for 1 hour at 37 $^{\circ}\text{C}$ prepared in PBS containing 0.1% BSA.
- (2) The biotinylated cRGD was aspirated out and the wells were washed three times with wash buffer.
- (3) The wells were then incubated with 100 μL of 0.6 $\mu\text{g}/\text{mL}$ of StreptavidinPE for 30 min at room temperature.
- (4) The wells were aspirated and washed them three times with wash buffer.
- (5) With 100 μL of PBS loaded in each well, the fluorescent signal of the StreptavidinPE remaining in the wells was measured with a fluorescence microplate reader.

The fluorescent intensity of each well was measured to verify the binding of cRGD with $\alpha\text{v}\beta_3$ integrin. In all cases, greater fluorescent signal was detected from $\alpha\text{v}\beta_3$ integrin wells compared with the un-coated negative control wells (1000 \pm 350 counts). The results are shown in Figure 52. Based on these results, all further wells were coated with $\alpha\text{v}\beta_3$ integrin at 1 $\mu\text{g}/\text{mL}$ dissolved in 1 mM MgCl_2 in PBS solution.

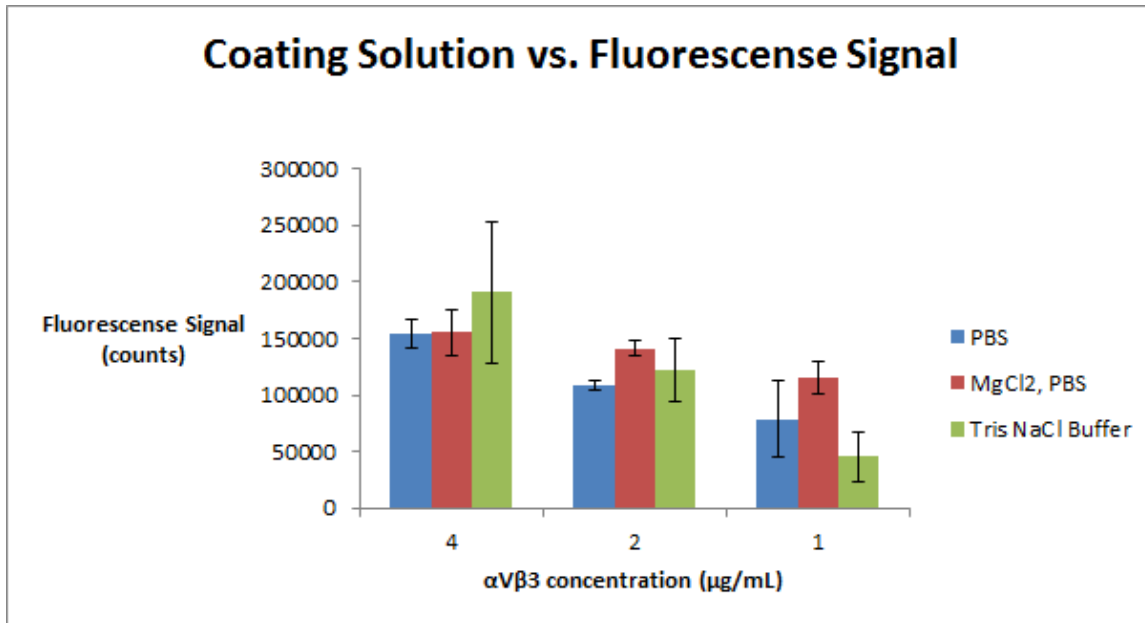


Figure 52: The StreptavidinPE fluorescence signal from wells coated with different concentrations of integrin and different coating buffers. After coating, wells were incubated with biotinylated cRGD and then StreptavidinPE.

Next, the binding of cRGD conjugated nanoparticles was evaluated directly by incubating integrin coated wells with known amounts of ^{52}Mn -MION-cRGD. Untargeted ^{52}Mn -MION was used as a negative control to assess the non-specific nanoparticle binding and the method is described below:

- (1) 42 wells were coated with $\alpha_v\beta_3$ integrin as previously described.
- (2) Wells were incubated with seven concentrations of cRGD conjugated and untargeted ^{52}Mn -MIONs ranging from 120 $\mu\text{g}/\text{mL}$ to 0 $\mu\text{g}/\text{mL}$ in triplicate.
- (3) Wells were washed three times with PBS.
- (4) Wells were cut from the plate, placed into test tubes, the gamma emission was counted and plotted versus the known incubation activity.

The results of the solid phase binding assay, shown in Figure 53, indicated that the ^{52}Mn -MION-cRGD had greater binding than the untargeted ^{52}Mn -MION. The uncertainty of the values was evaluated by the standard deviation of the triplicate measurement. The greater uptake of the cRGD targeted MIONs indicates the binding of the ^{52}Mn -MION-cRGD with the $\alpha_v\beta_3$ integrin.

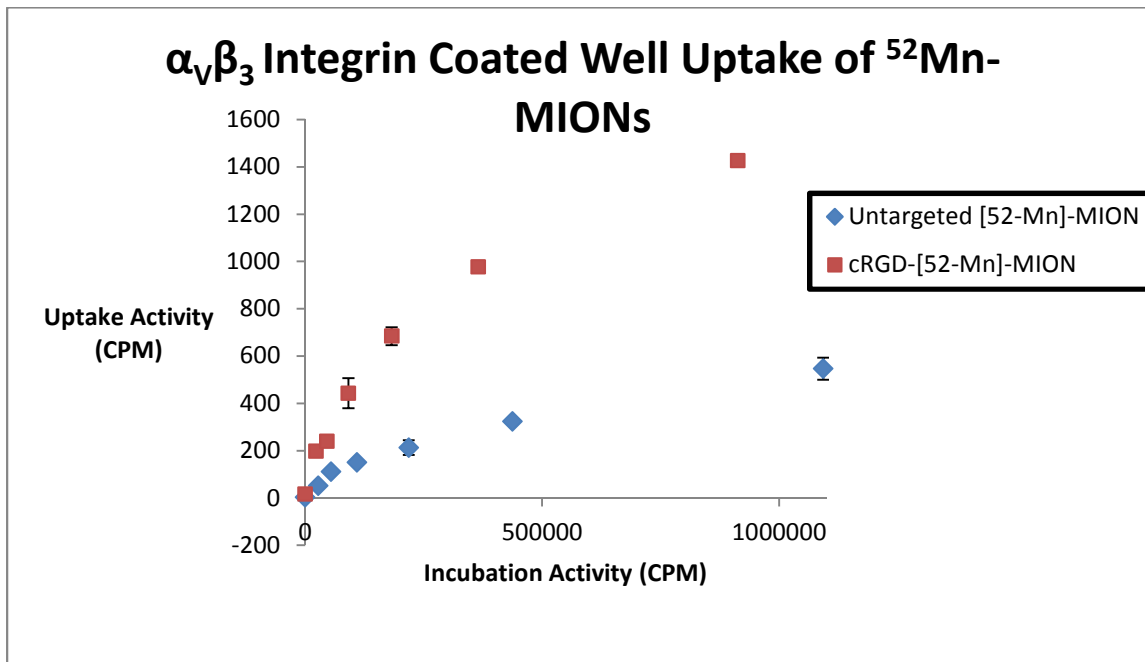


Figure 53: Solid phase binding assay of conjugated and untargeted ^{52}Mn -MIONs with wells coated with $\alpha_v\beta_3$. The greater uptake of the cRGD targeted MIONs indicates the binding of the ^{52}Mn -MION-cRGD with the $\alpha_v\beta_3$ integrin.

5.2.4. PET Results

[⁵²Mn]-MION-cRGDs were utilized to image nude mice bearing U87MG xenograft tumors. The tumors were implanted as described in Section 5.2.2, and grown for 10 days. The tumors were 110 ± 40 mg in mass at the time of the imaging study, based on caliper measurements. Tumor bearing mice were split into three groups, based on the surface coating of [⁵²Mn]-MIONs that were administered via tail-vein injection and in one group based on the blocking cRGD dose used. Three mice were injected with untargeted [⁵²Mn]-MION (162±7 µCi, 110±5 mg of Fe), as an untargeted control. Three mice were injected with [⁵²Mn]-MION-cRGD (125±4 µCi, 86±3 mg of Fe), for targeted imaging. And finally two mice were injected with [⁵²Mn]-MION-cRGD (115±3 µCi, 79±2 mg of Fe) and a blocking dose of 1.3 mg of free cRGD. During the bioconjugation reaction, 100 µg of cRGD is used for an entire synthesis, therefore the blocking dose should be at least 50-100 times the cRGD concentration present on the injected [⁵²Mn]-MION-cRGDs. During the study, one mouse from the second cohort and one mouse from the third cohort died from the extensive use of anesthetic needed for the multiple imaging sessions. Mice were MR imaged before injection. At 3 hours and 24 hours after MION injection, each mouse was MR and PET/CT imaged. Each mouse has a customized pallet with an outline of the mouse for increased reproducibility during image setup, as shown in Figure 54.



Figure 54: Each mouse in the imaging study had an individualized pallet that was used in both the MR and PET scanners. An outline of the mouse was drawn to increase positioning reproducibility, but because of the different shaped nose cones of the scanners, positioning was not entirely reproduced.

After the imaging study, PET, CT, and MRI images were initially rigidly co-registered for analysis. Regions of interest (ROIs) were contoured over the tumor, liver, kidneys, and brain of each mouse, and the %ID/g from the PET scans was calculated as described below:

- (1) PET images were reconstructed using the OSEM3D-MAP iterative algorithm. By utilizing the phantom measurements described in Section 5.1, the scanner was calibrated following the scanner manufacturers protocol, and the voxel values were given in units of nCi/cm^3 .
- (2) ROIs were drawn over the tumor, liver, kidney, and brain of each mouse. The average signal (S_{ROI}) in nCi/cm^3 of each ROI was calculated.
- (3) The injected dose (ID) in μCi that was measured at the time of injection was decay corrected to the start of the scan to give the decay corrected injected dose (ID_{decay}).
- (4) The %ID/g was calculated using equation 11. The assumption was made that 1 cm^3 of soft tissue had a mass of 1 g.

$$\frac{\%ID}{g} = 100 * \frac{S_{ROI} * \frac{1 \mu Ci}{1000 nCi}}{ID_{decay}}$$

Note that the tumor, liver, brain contours were made with only the CT image, while the kidneys were contoured with both CT and MR image input. The image quantification of %ID/g of the tumors from all cohorts is shown in Figure 55. Values are average %ID/g of all voxels within the ROI averaged across multiple mice.

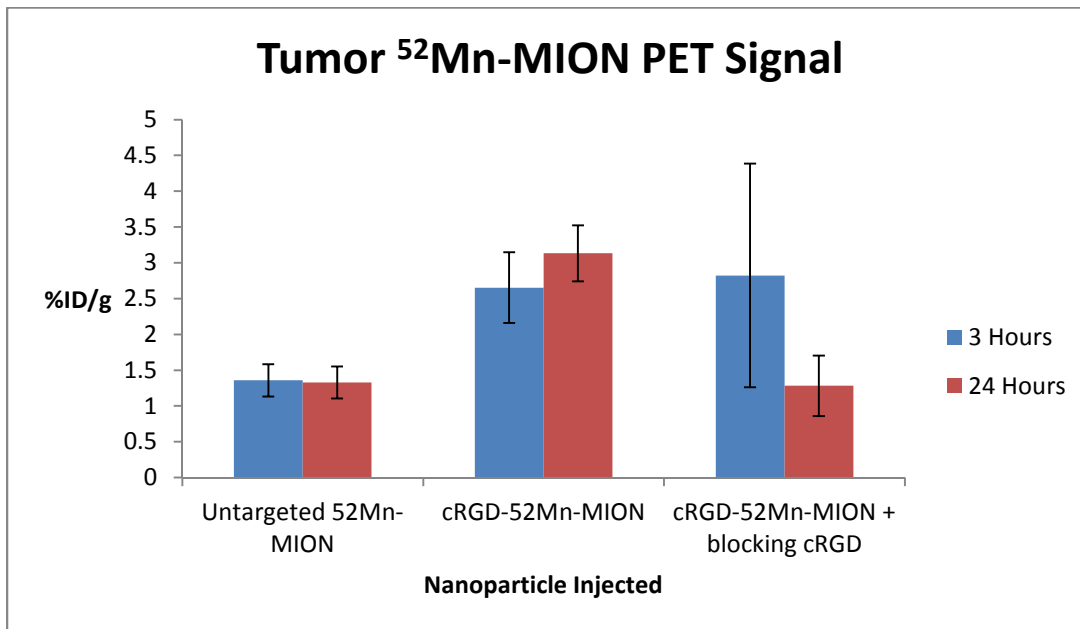


Figure 55: The %ID/g of ⁵²Mn-MION, quantified through ROI analysis of PET images. Contours were drawn based on co-registered CT and MR images. U87MG xenograph tumor bearing mice were tail-vein injected with untargeted [⁵²Mn]-MION (162±7 μCi, 110±5 mg of Fe), [⁵²Mn]-MION-cRGD (125±4 μCi, 86±3 mg of Fe), or [⁵²Mn]-MION-cRGD (115±3 μCi, 79±2 mg of Fe) and a blocking dose of 1.3 mg of free cRGD, and PET and MRI scanned at different time points.

Higher PET signal is measured for cRGD targeted MIONs compared to the untargeted MIONs at both 3 hours and 24 hours. This indicates that MION uptake in the tumor is increased through nanoparticle cRGD targeting. The blocked ⁵²Mn-MION-cRGD tumor uptake is similar to the unblocked at 3 hours, but decreases at 24 hours. This indicates only a partial blocking effect,

which is difficult to explain, considering the large blocking dose. The increased clearance of ^{52}Mn -MION-cRGD when administered with a blocking dose of free cRGD indicates some specific nanoparticle binding.

Uncertainty values are from the standard deviation of %ID/g. The %ID/g values of all four tissues from each cohort are shown in Figure 56, Figure 57, and Figure 58. %ID/g values are also shown in Table 13. For all ^{52}Mn -MION injections, regardless of targeting, the greatest uptake is in the liver. This is likely due to the uptake of nanoparticles by Kupffer cells and other macrophages in the liver as part of the reticuloendothelial system. The low uptake in the brain indicates that the nanoparticles are unable to cross the blood-brain barrier. Finally, the moderate uptake in the kidneys may indicate that some of the radionuclide is undergoing renal clearance.

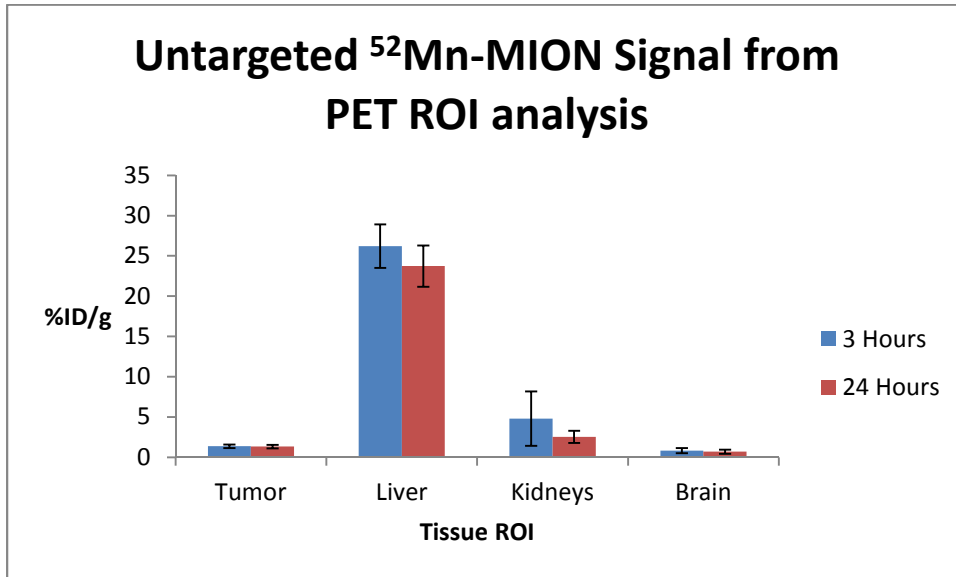


Figure 56: %ID/g of various tissues from ROI analysis of PET image data. Mice were injected with untargeted ^{52}Mn -MIONs ($162 \pm 7 \mu\text{Ci}$, $110 \pm 5 \text{ mg}$ of Fe) and show high uptake in the liver at both time points. Tumor and brain accumulation is low, while kidney uptake is moderate.

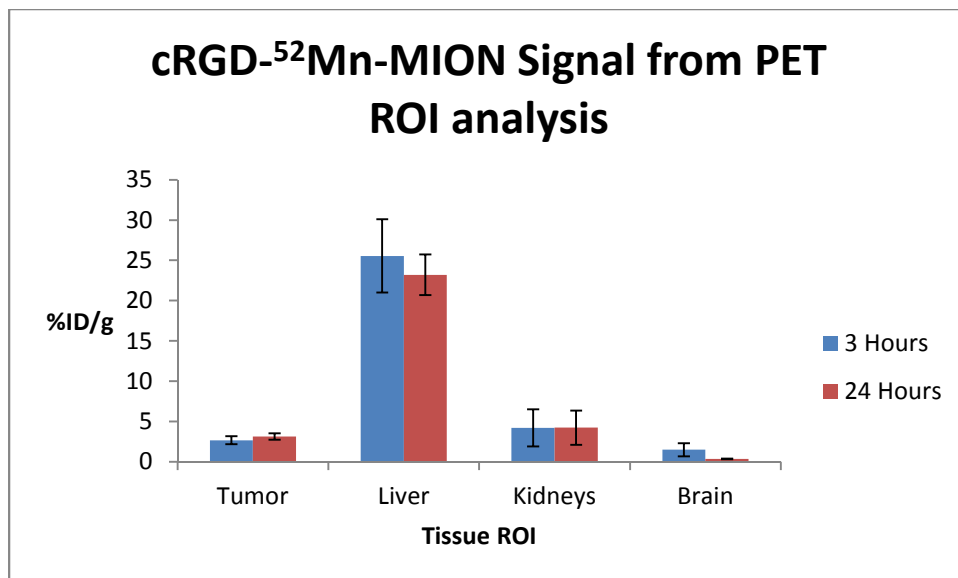


Figure 57: %ID/g of various tissues from ROI analysis of PET image data. Mice were injected with ⁵²Mn-MION-cRGDs (125±4 μCi, 86±3 mg of Fe) and show high uptake in the liver at both time points. Brain accumulation is low, while kidney uptake is moderate. Tumor uptake is increased compared to the untargeted nanoparticles.

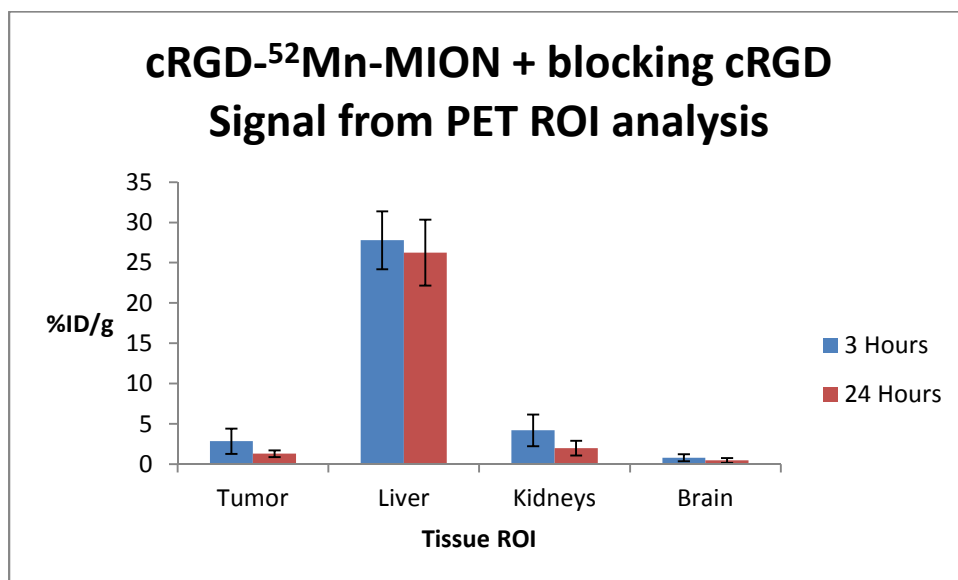


Figure 58: %ID/g of various tissues from ROI analysis of PET image data. Mice were injected with ⁵²Mn-MION-cRGDs (115±3 μCi, 79±2 mg of Fe) and a blocking dose of 1.3 mg of free cRGD and show high uptake in the liver at both time points. Brain accumulation is low, while kidney uptake is moderate. Tumor uptake is initially high, but decreases at the 24 hour time.

Table 13: The %ID/g values of various tissues as measured with ROI analysis of PET data for ⁵²Mn-MION injected tumor bearing mice.

Nanoparticle Injection	Tissue	3 Hour Uptake (%ID/g)	24 Hour Uptake (%ID/g)
Untargeted ⁵² Mn-MION	Tumor	1.4±0.2	1.3±0.2
	Liver	26±3	24±3
	Kidneys	5±3	3±1
	Brain	0.8±0.3	0.7±0.3
⁵² Mn-MION-cRGD	Tumor	2.7±0.5	3.1±0.4
	Liver	26±5	23±3
	Kidneys	4±2	4±2
	Brain	1.5±0.8	0.34±0.08
⁵² Mn-MION-cRGD + blocking cRGD	Tumor	2.8±1.6	1.3±0.4
	Liver	28±4	26±4
	Kidneys	4±2	2±1
	Brain	0.8±0.4	0.4±0.3

The PET/CT imaging data collected is presented below, in Figure 59 through Figure 64, as selected sagittal and coronal slices of the mice, chosen to show the tumor, liver, and brain.

Thresholding, windowing, and leveling are consistent through all images.

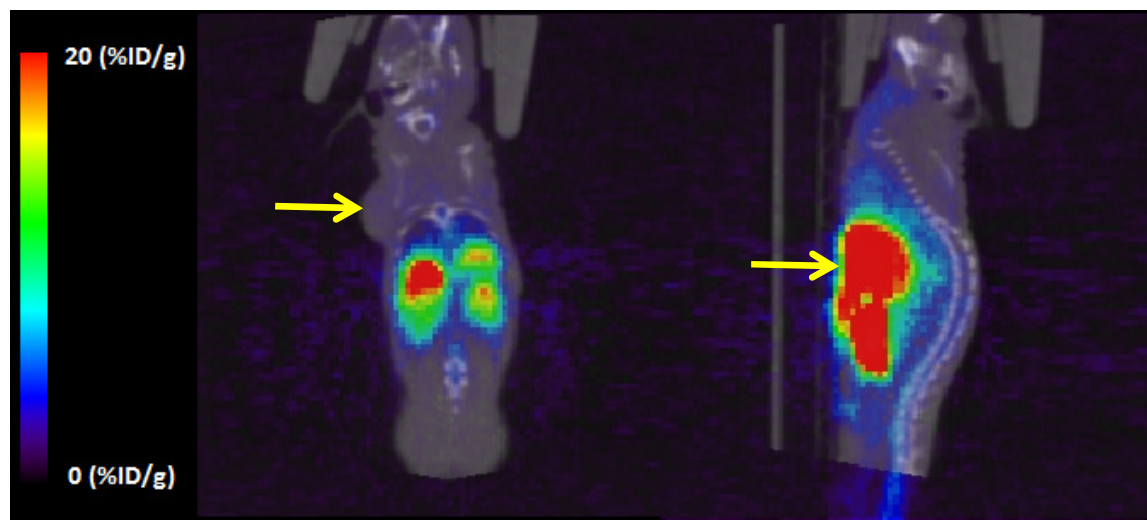


Figure 59: Selected PET/CT images of U87MG tumor bearing mouse tail vein injected with untargeted ⁵²Mn-MION (162±7 μCi, 110±5 mg of Fe) 3 hours after injection. The left coronal image shows the right shoulder tumor (arrow). The right sagittal view shows high signal from the liver (arrow).

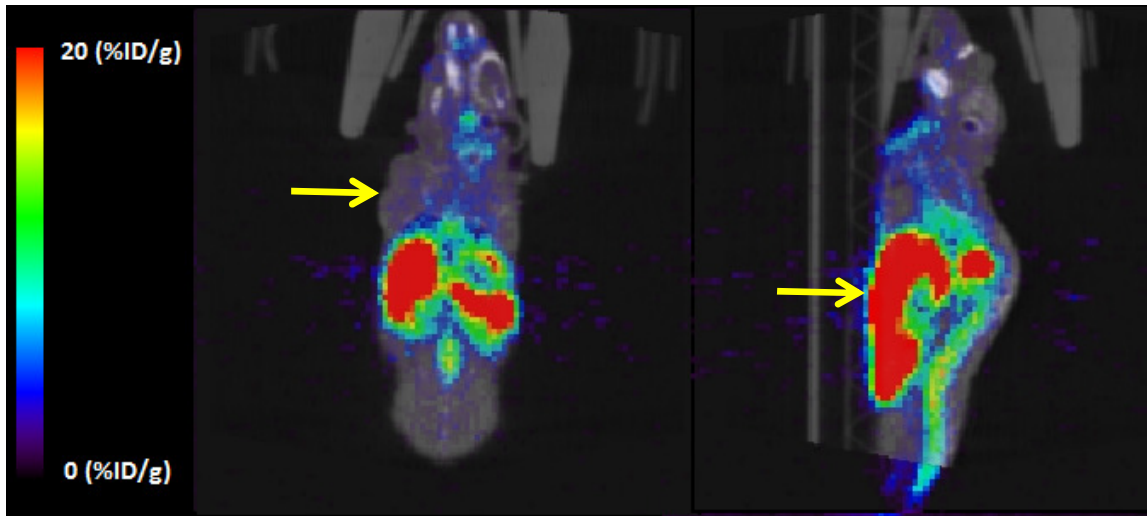


Figure 60: Selected PET/CT images of U87MG tumor bearing mouse tail vein injected with untargeted ^{52}Mn -MION ($162\pm 7 \mu\text{Ci}$, $110\pm 5 \text{ mg}$ of Fe) 24 hours after injection. The left coronal image shows the right shoulder tumor (arrow). The right sagittal view shows high signal from the liver (arrow).

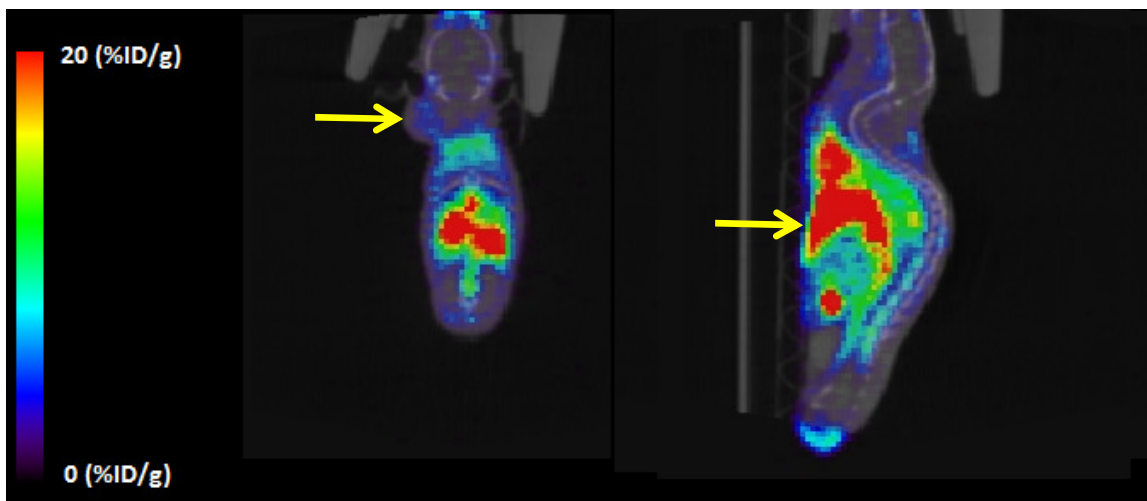


Figure 61: Selected PET/CT images of U87MG tumor bearing mouse tail vein injected with cRGD targeted ^{52}Mn -MION ($125\pm 4 \mu\text{Ci}$, $86\pm 3 \text{ mg}$ of Fe) 3 hours after injection. The left coronal image shows the right shoulder tumor (arrow). The right sagittal view shows high signal from the liver (arrow).

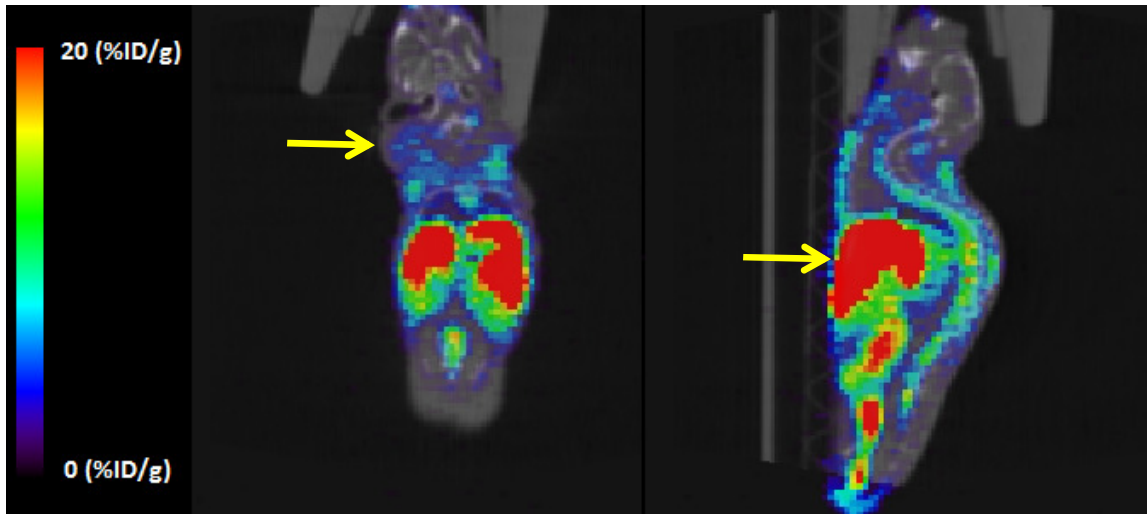


Figure 62: Selected PET/CT images of U87MG tumor bearing mouse tail vein injected with cRGD targeted ^{52}Mn -MION ($125\pm 4 \mu\text{Ci}$, $86\pm 3 \text{ mg}$ of Fe) 24 hours after injection. The left coronal image shows the right shoulder tumor (arrow). The right sagittal view shows high signal from the liver (arrow).

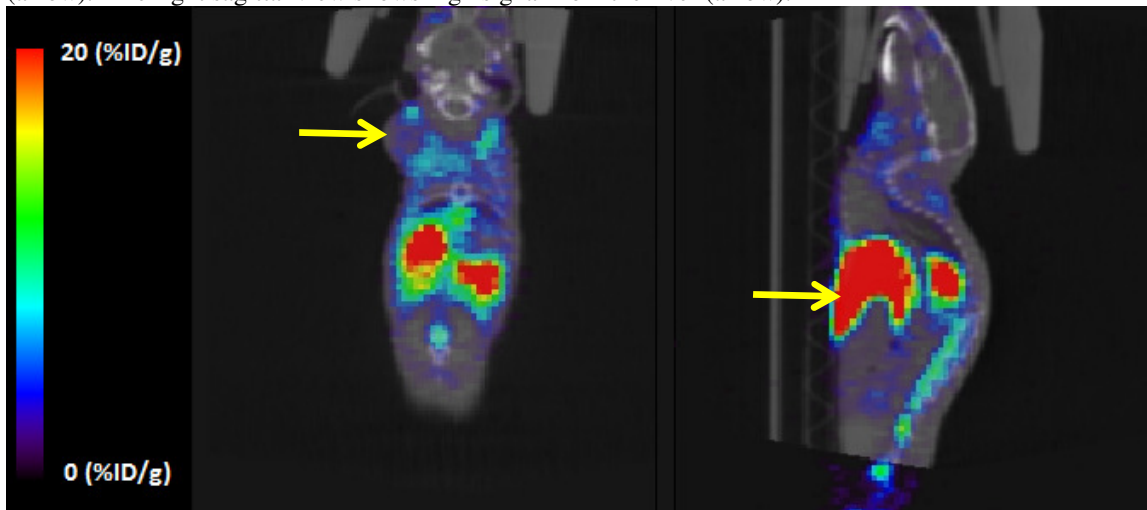


Figure 63: Selected PET/CT images of U87MG tumor bearing mouse tail vein injected with cRGD targeted ^{52}Mn -MION ($115\pm 3 \mu\text{Ci}$, $79\pm 2 \text{ mg}$ of Fe) 3 hours after injection. The left coronal image shows the right shoulder tumor (arrow). The right sagittal view shows high signal from the liver (arrow).

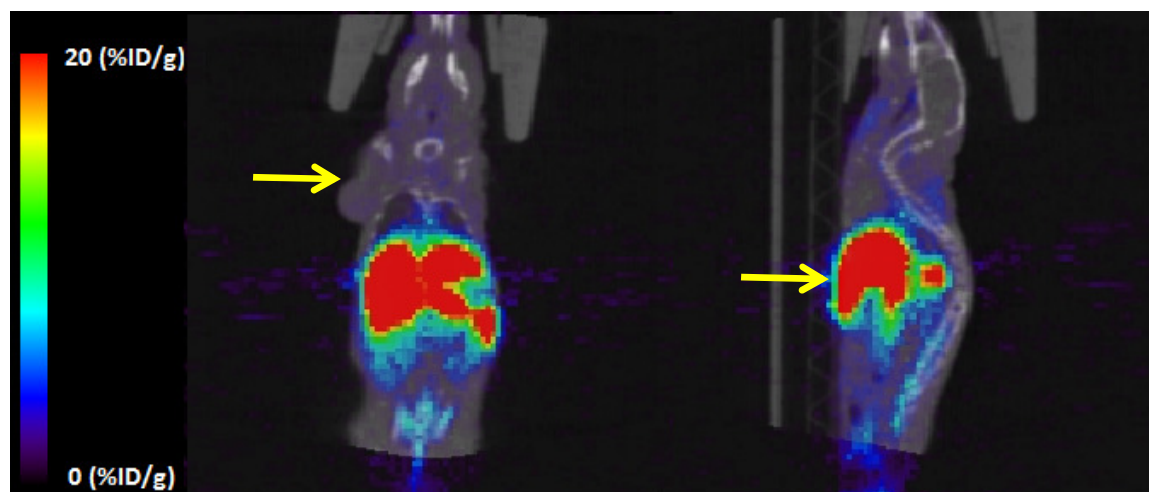


Figure 64: Selected PET/CT images of U87MG tumor bearing mouse tail vein injected with cRGD targeted ^{52}Mn -MION ($115 \pm 3 \mu\text{Ci}$, $79 \pm 2 \text{ mg of Fe}$) 24 hours after injection. The left coronal image shows the right shoulder tumor (arrow). The right sagittal view shows high signal from the liver (arrow).

As a non-MION control, $^{52}\text{MnCl}_2$ was injected into a non-tumor bearing mouse ($73 \mu\text{Ci}$) and PET imaged 24 hours after injection. The resulting PET images, shown in Figure 65, show considerable liver uptake, similar to the ^{52}Mn -MIONs, but also large kidney signal, unlike the ^{52}Mn -MIONs. After the imaging, the mouse was sacrificed, and the %ID/g of each tissue was measured through gamma emission, as described in Section 4.1. The results of this biodistribution study are shown in Figure 66, and parallel the PET data, with large uptake in the kidneys and liver. The differences in the PET data from $^{52}\text{MnCl}_2$ injected mouse and the ^{52}Mn -MION injected mice, indicate that the nanoparticle construct is affecting the distribution and uptake of ^{52}Mn *in vivo*. Also, the difference in kidney signal between the $^{52}\text{MnCl}_2$ injected mouse and the ^{52}Mn -MION indicate that the ^{52}Mn is staying with the ^{52}Mn -MION after injection.

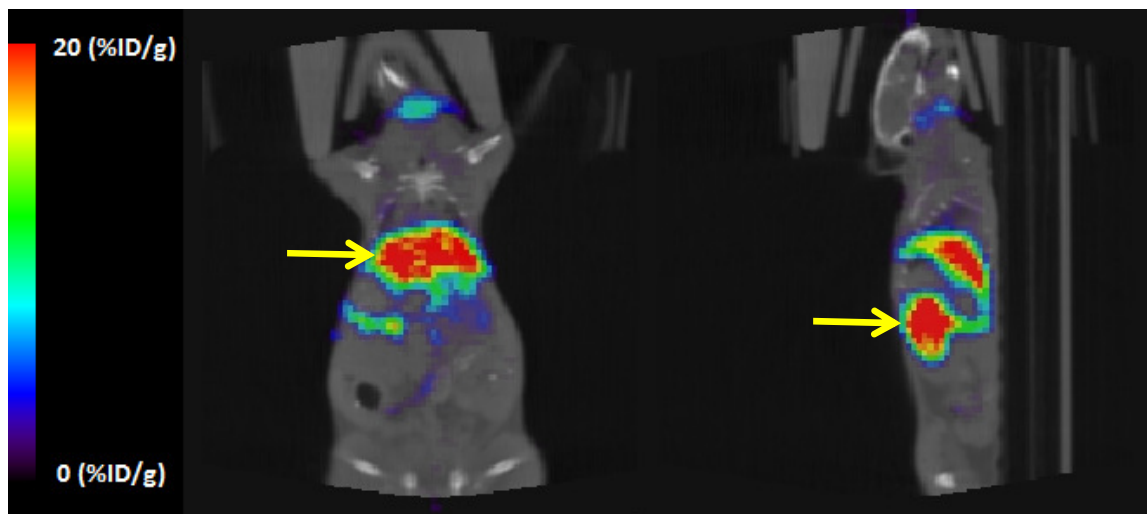


Figure 65: PET/CT image of $^{52}\text{MnCl}_2$ (73 μCi) injected mouse. The left coronal view shows high liver (arrow) signal, while the right sagittal view also shows considerable kidney signal.

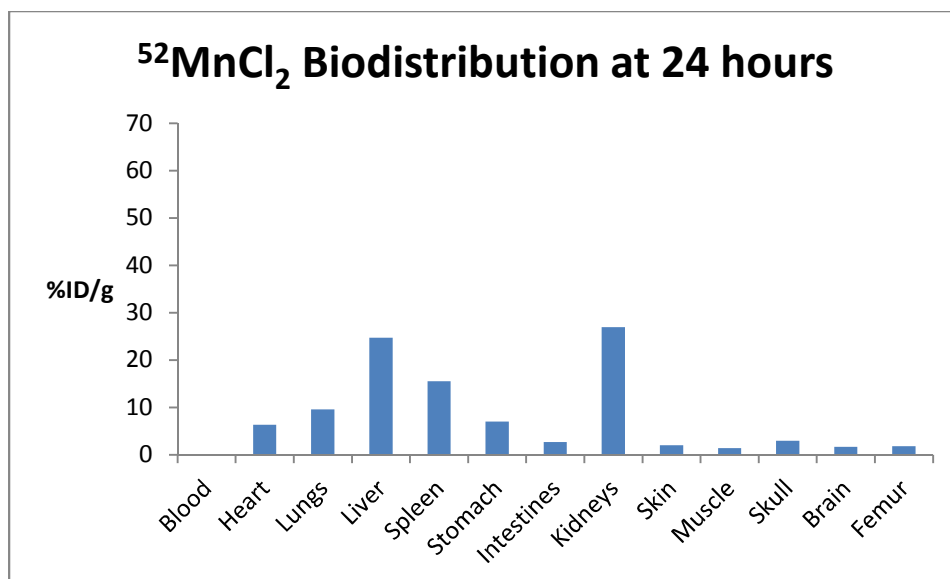


Figure 66: Biodistribution of a $^{52}\text{MnCl}_2$ injected mouse 24 hours post-injection. A nude mouse was tail-vein injected with 73 μCi of $^{52}\text{MnCl}_2$ and sacrificed after 24 hours. The tissues were collected and weighed and the %ID/g was calculated for various tissue. The high uptake in the liver and kidneys parallels the PET data, shown in Figure 65.

5.2.5. MRI Results

In the ^{52}Mn -MION-cRGD imaging study, MR images were collected along with the PET data, as described in Section 5.2.4. Mice were also imaged before injection. The MR imaging protocol used was the same FISP sequence that was described and utilized in Section 4.2. Selected

coronal images below show the tumor of each injected mouse before, 3 hours after, and 24 hours after injection.

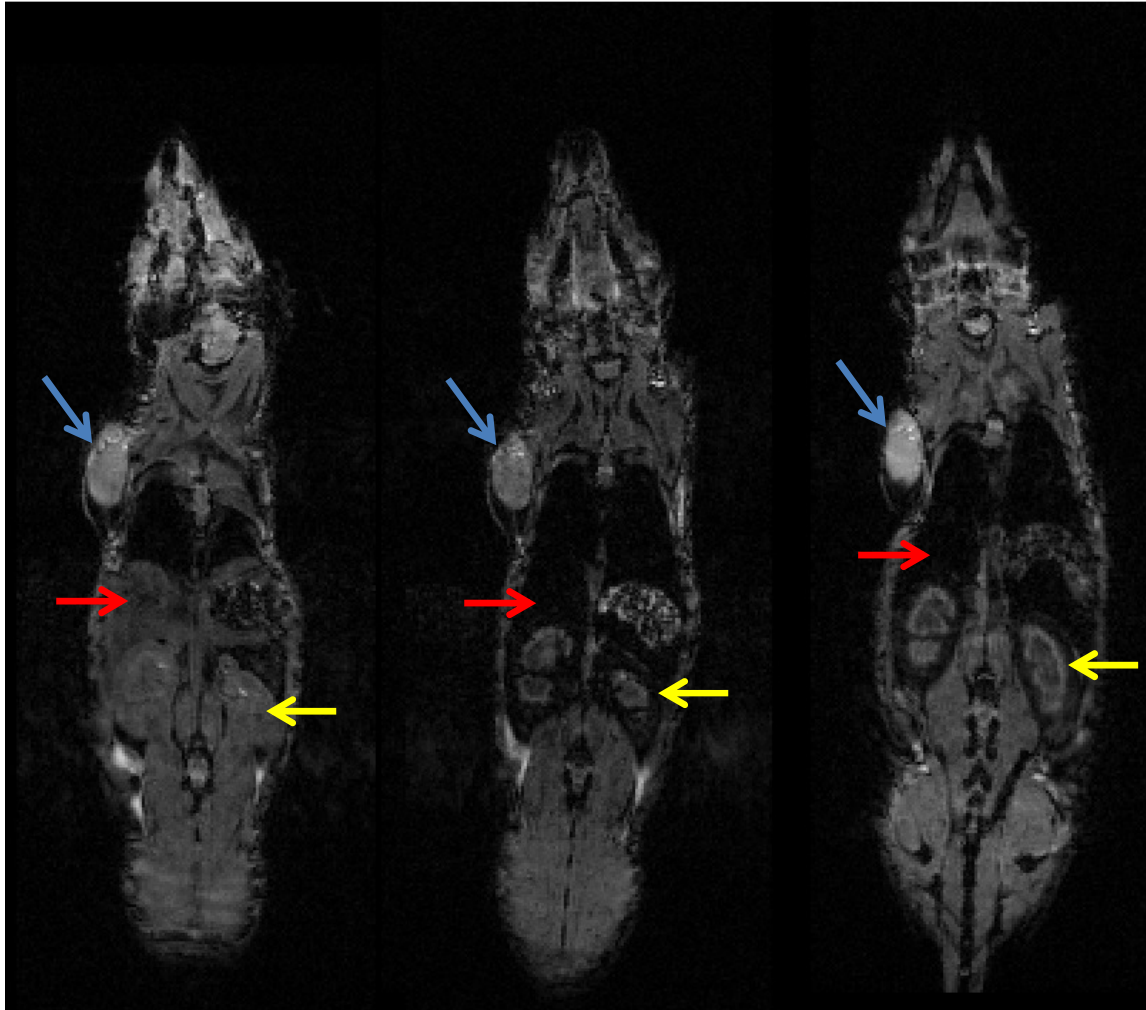


Figure 67: Select images of untargeted ⁵²Mn-MION injected ($162\pm 7 \mu\text{Ci}$, $110\pm 5 \text{ mg}$ of Fe) mouse before (left), 3 hours after (middle), and 24 hours after (right) injection. The mouse was imaged with a Fast Imaging with Steady State Precession (FISP) sequence with a repeat time (TR) of 9.4 ms and echo time (TE) of 4.7 ms and number of scans averaged (NSA) of 4. A flip angle (FA) of 35° was used to achieve T2*/T1 weighted images. The blue arrows indicate the tumor, the red arrows indicate the liver, and the yellow arrows indicate the kidneys.

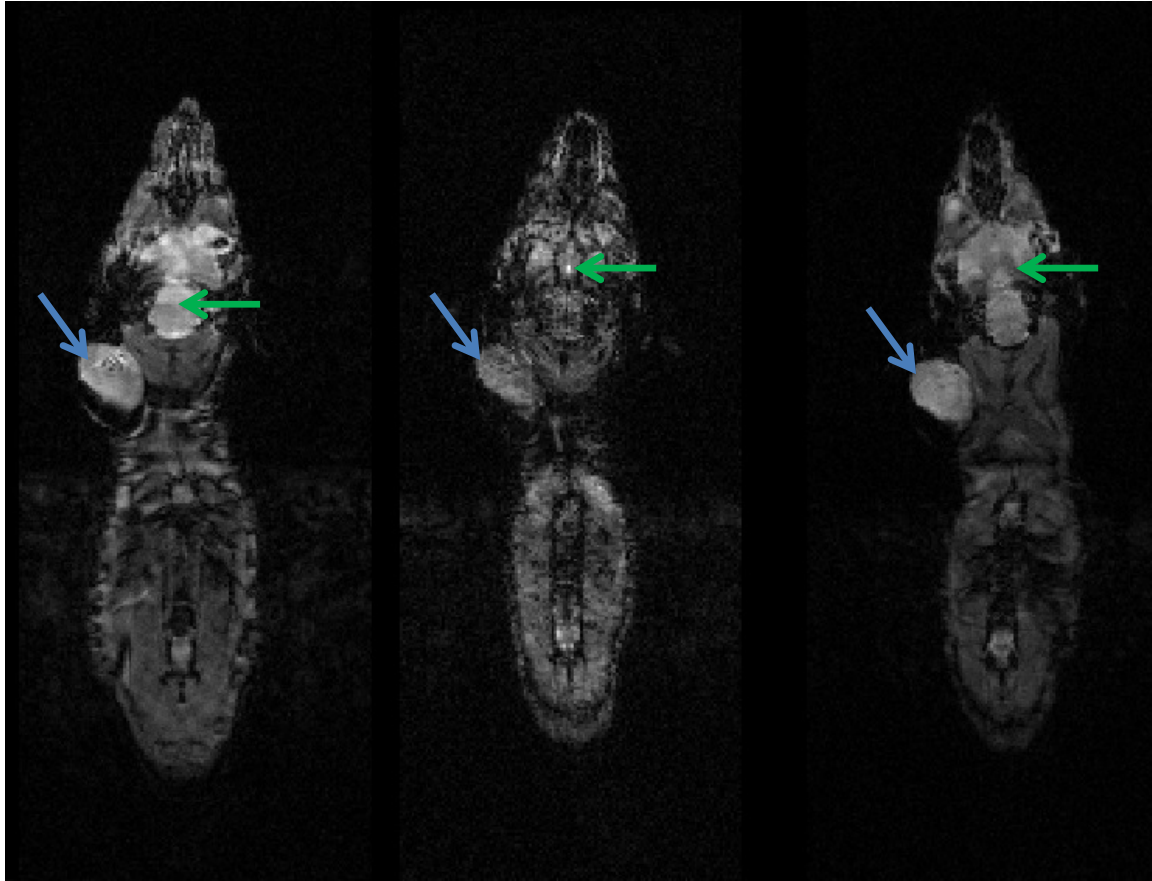


Figure 68: Select images of cRGD targeted ^{52}Mn -MION injected ($125 \pm 4 \mu\text{Ci}$, $86 \pm 3 \text{ mg of Fe}$) mouse before (left), 3 hours after (middle), and 24 hours after (right) injection. The mouse was imaged with a Fast Imaging with Steady State Precession (FISP) sequence with a repeat time (TR) of 9.4 ms and echo time (TE) of 4.7 ms and number of scans averaged (NSA) of 4. A flip angle (FA) of 35° was used to achieve T2*/T1 weighted images. The blue arrows indicate the tumor, the green arrows indicate the brain. The liver and kidneys are not visible in this image.

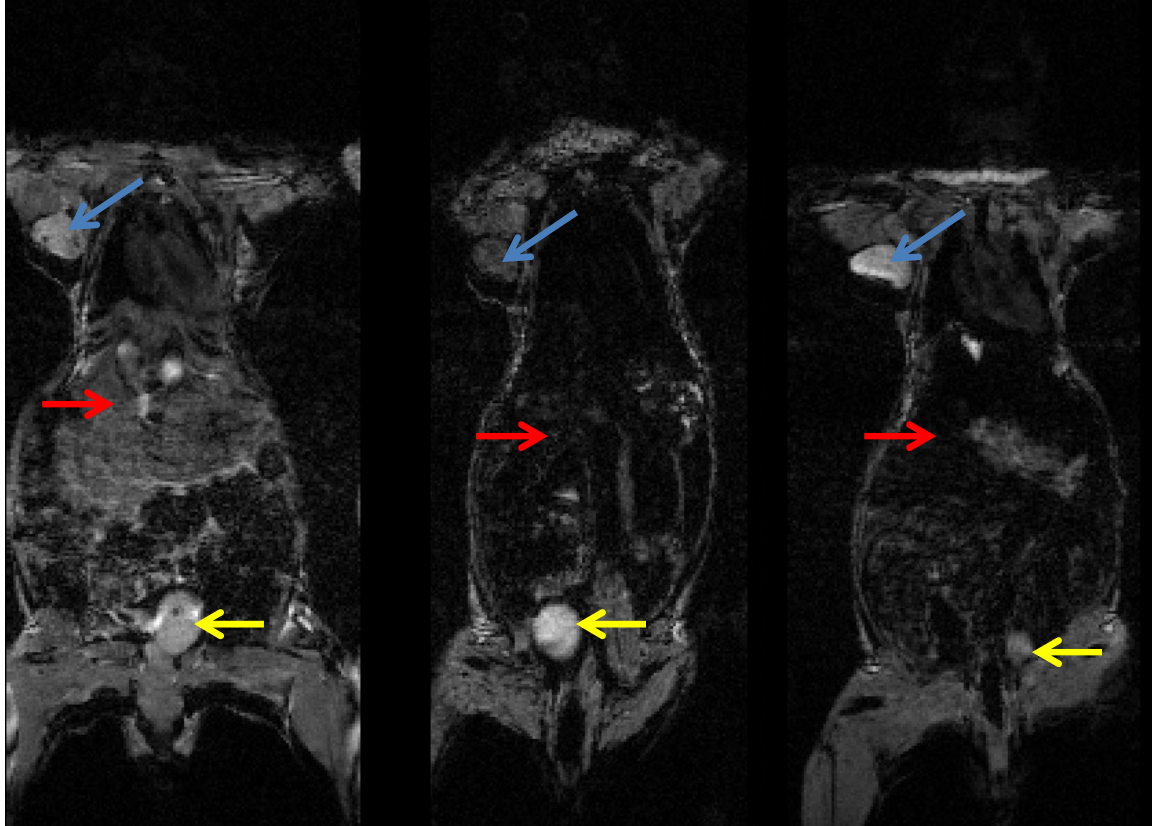


Figure 69: Select images of cRGD targeted ^{52}Mn -MION and blocking free cRGD injected ($115\pm 3 \mu\text{Ci}$, $79\pm 2 \text{ mg}$ of Fe) mouse before (left), 3 hours after (middle), and 24 hours after (right) injection. The mouse was imaged with a Fast Imaging with Steady State Precession (FISP) sequence with a repeat time (TR) of 9.4 ms and echo time (TE) of 4.7 ms and number of scans averaged (NSA) of 4. A flip angle (FA) of 35° was used to achieve T2*/T1 weighted images. The blue arrows indicate the tumor, the red arrows indicate the liver, and the yellow arrows indicate the bladder. The kidneys are not visible in this image.

The % contrast is measured as the percent signal decrease of the ROI compared with the ROI of the same tissue imaged before injection. After image acquisition, the MR images were rigidly co-registered and ROIs were drawn on the tumor, liver, kidney, and brain tissues. The mean MR signal from each ROI was used to calculate the contrast induced by the MION injections in each tissue. The contrast measured in the tumors is shown in Figure 70. A significantly larger amount of contrast is only seen in the ^{52}Mn -MION-cRGD injected at 3 hours after injection, compared to the untargeted and cRGD blocking injections. The quantification of MR contrast of the other tissues is shown below as % contrast in Figure 71, Figure 72, and Figure 73.

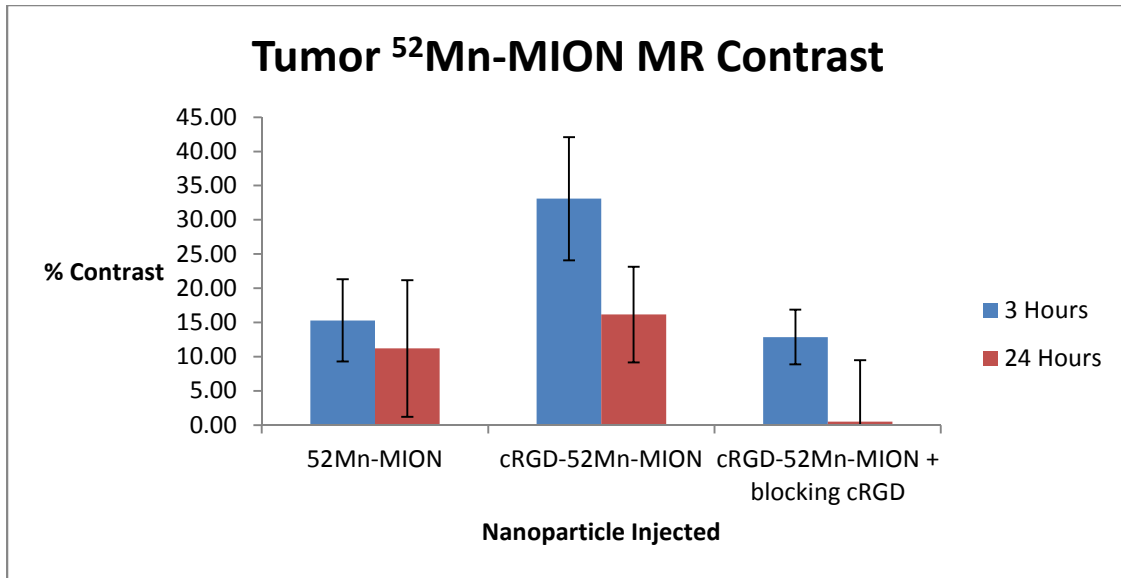


Figure 70: The % contrast induced in tumor tissue by ⁵²Mn-MION injection, quantified through ROI analysis of MR images. Contours were drawn based on co-registered the MR images. U87MG xenograph tumor bearing mice were tail-vein injected with untargeted [⁵²Mn]-MION (162±7 μCi, 110±5 mg of Fe), [⁵²Mn]-MION-cRGD (125±4 μCi, 86±3 mg of Fe), or [⁵²Mn]-MION-cRGD (115±3 μCi, 79±2 mg of Fe) and a blocking dose of 1.3 mg of free cRGD.

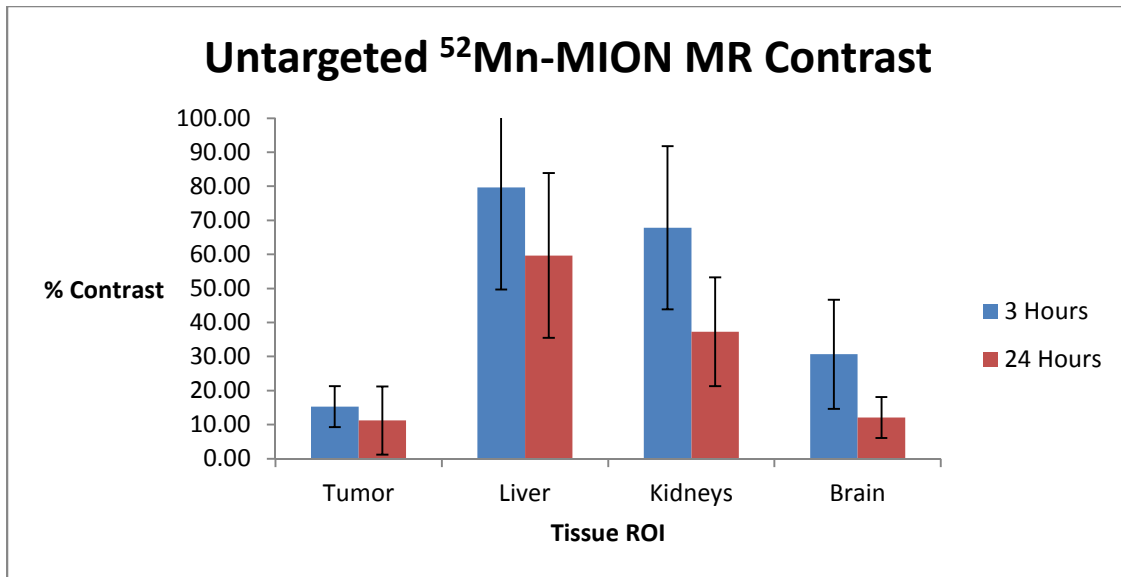


Figure 71: The % contrast induced by untargeted ⁵²Mn-MION injection (162±7 μCi, 110±5 mg of Fe) in specific tissues measured with ROI analysis. The % contrast is measured as the percent signal decrease of the ROI compared with the ROI of the same tissue imaged before injection.

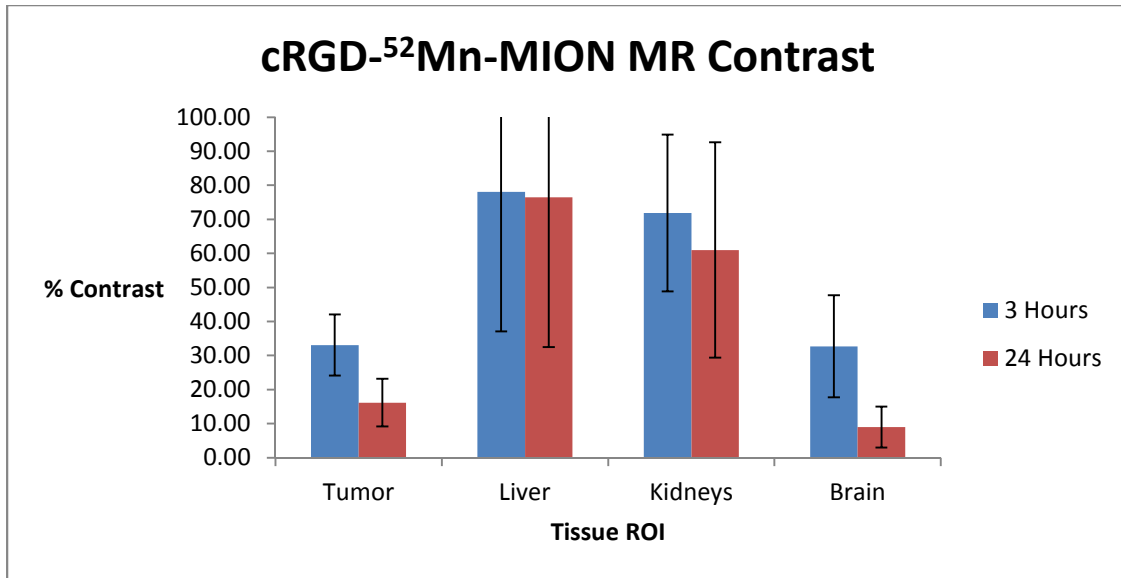


Figure 72: The % contrast induced by cRGD-⁵²Mn-MION injection ($125 \pm 4 \mu\text{Ci}$, $86 \pm 3 \text{ mg}$ of Fe) in specific tissues measured with ROI analysis. The % contrast is measured as the percent signal decrease of the ROI compared with the ROI of the same tissue imaged before injection.

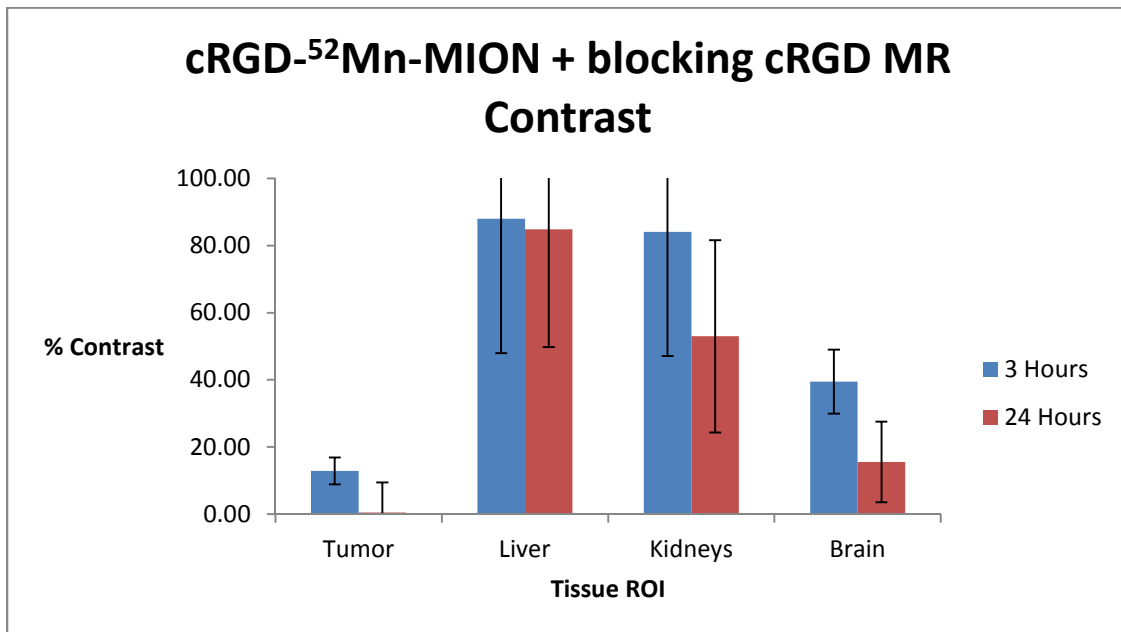


Figure 73: The % contrast induced by cRGD-⁵²Mn-MION ($115 \pm 3 \mu\text{Ci}$, $79 \pm 2 \text{ mg}$ of Fe) and blocking free cRGD injection in specific tissues measured with ROI analysis. The % contrast is measured as the percent signal decrease of the ROI compared with the ROI of the same tissue imaged before injection.

5.2.6. Co-registered Hybrid PET/MRI Results

Finally, PET/CT imaging results were rigidly co-registered with MR results, based on landmarks, specifically the skull, spine, and liver. The registration error was not evaluated, because the structures being co-registered were not ridged, and such analysis was not necessary for this study. Selected slices of the hybrid images are shown below in Figure 74, Figure 75, and Figure 76. PET signal matches with areas of MR contrast, especially in the liver. The right shoulder tumors show only small MR contrast and PET signal. The quantification of probe concentration from MR data was found not to be a robust method, as shown in Section 4.4.2, so side by side comparisons of PET signal based %ID/g and MR % contrast based %ID/g were not plotted.

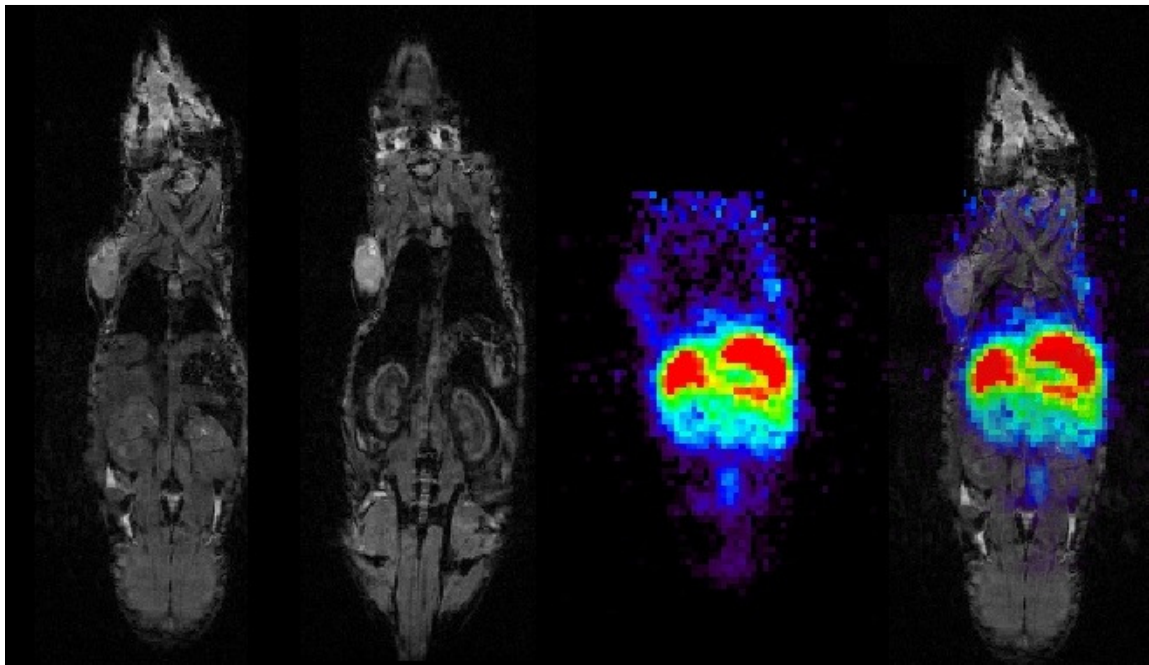


Figure 74: Coronal images of an untargeted ^{52}Mn -MION injected ($162 \pm 7 \mu\text{Ci}$, $110 \pm 5 \text{ mg}$ of Fe) mouse 24 hours after injection. The MR image of the mouse before injection is on the far left, while the MR image of the mouse 24 hours after injection is on the left middle. The PET scan of the mouse after 24 hours is on the middle right, while the co-registered pre-injection MR image with the PET image is on the far right.

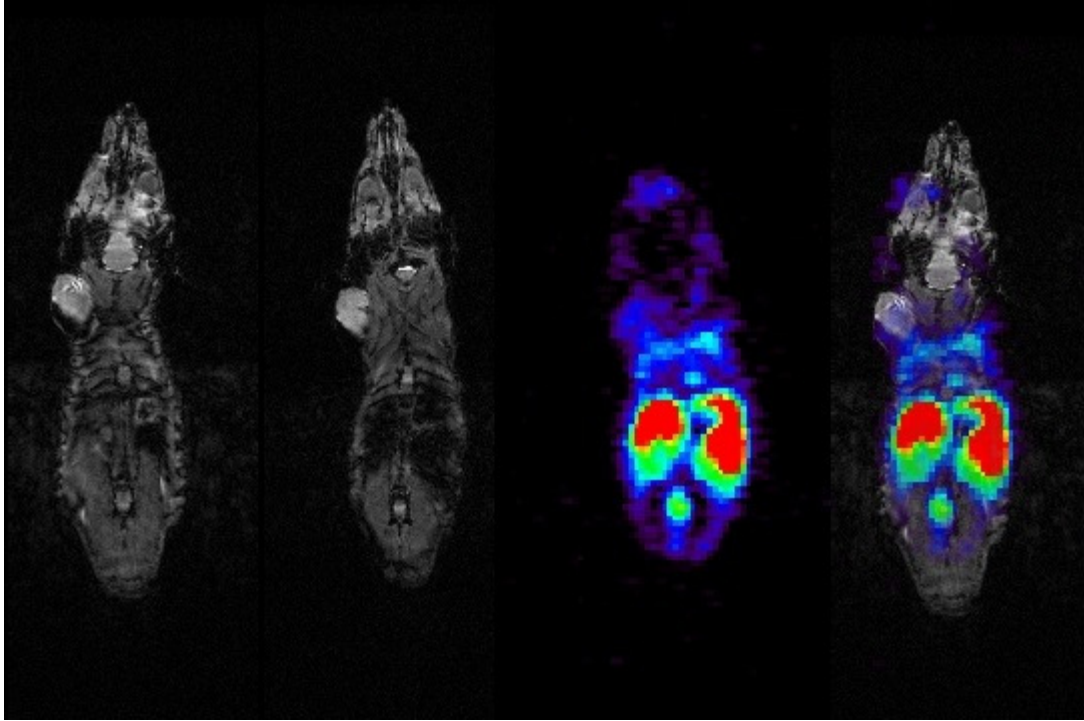


Figure 75: Coronal images of a ^{52}Mn -MION-cRGD ($125\pm 4 \mu\text{Ci}$, $86\pm 3 \text{ mg}$ of Fe) injected mouse 24 hours after injection. The MR image of the mouse before injection is on the far left, while the MR image of the mouse 24 hours after injection is on the left middle. The PET scan of the mouse after 24 hours is on the middle right, while the co-registered pre-injection MR image with the PET image is on the far right.

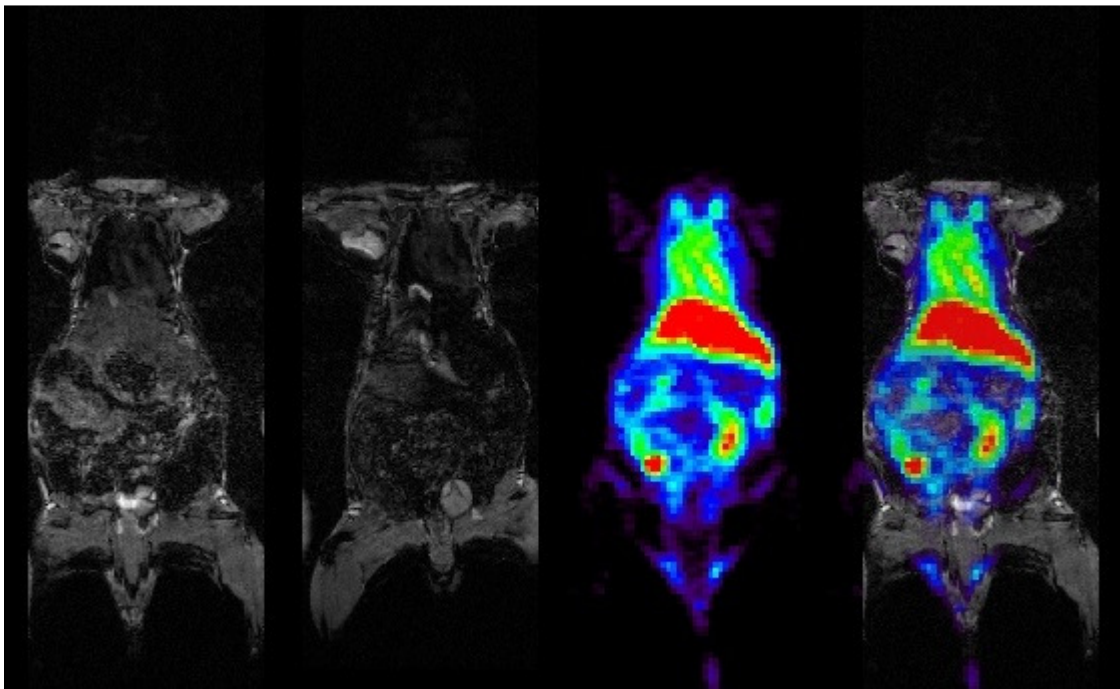


Figure 76: Coronal images of an ^{52}Mn -MION-cRGD ($115\pm 3 \mu\text{Ci}$, $79\pm 2 \text{ mg}$ of Fe) with blocking cRGD injected mouse 24 hours after injection. The MR image of the mouse before injection is on the far left, while the MR image

of the mouse 24 hours after injection is on the left middle. The PET scan of the mouse after 24 hours is on the middle right, while the co-registered pre-injection MR image with the PET image is on the far right.

Chapter 6

6. Summary and Conclusion

A synthetic method has been developed for the intrinsic incorporation of ^{59}Fe into SPION MRI contrast agents. These nanoparticles have been coated with a multidentate poly-ethylene-glycol ligand for water solubility and biocompatibility. The physical characteristics, including hydrodynamic size, inorganic core size, surface charge, and relaxivity have been measured. Additionally, the in vivo biodistribution of the untargeted SPIONs has been characterized with MRI and the gamma emission of ^{59}Fe -SPIONs.

After this was accomplished, ^{52}Mn was produced with a small hospital based cyclotron. It was chemically separated and purified, then incorporated into ^{52}Mn -MIONs. The gamma spectrum of ^{52}Mn was characterized. Additionally, the PET imaging characteristics of sensitivity, spatial resolution, and count-rate linearity were evaluated for ^{52}Mn in a small animal PET scanner.

Finally, the ^{52}Mn -MION surface ligands were modified with the addition of cRGD, an imaging peptide. The binding of cRGD and ^{52}Mn -MION-cRGD with $\alpha_v\beta_3$ integrin was confirmed with solid phase $\alpha_v\beta_3$ integrin assay. Then ^{52}Mn -MION-cRGD was utilized in a hybrid PET/MRI study with U87MG tumor xenograft bearing mice. Tumor PET signal was increased in ^{52}Mn -MION-cRGD injected mice, compared with untargeted ^{52}Mn -MION injected mice.

6.1. Radio-intrinsic superparamagnetic nanoparticles

The incorporation of ^{59}Fe into the SPION structure was accomplished with two strategies. The first included the ^{59}Fe in the initial reagents and utilized the radionuclide throughout the nanoparticle structure. The second approach added the radionuclide to already formed SPION cores, to form a shell that included the radioactive iron. This allowed for increased radionuclide yield and reduced starting reagents. Either approach resulted in nanoparticles with similar relaxivity as natural nanoparticles synthesized with similar strategies. This indicates that the incorporation of ^{59}Fe within SPION nano-crystal structures was accomplished without reducing their relaxivity, and thereby lessening their usefulness as hybrid imaging agents. Initially, a strategy similar to the ^{59}Fe core/shell incorporation was developed for ^{52}Mn incorporation. The resulting core/shell MION productions yielded nanoparticles with inconsistent radionuclide incorporation efficiency and MR characteristics. Therefore, an incorporation strategy similar to the first single step ^{59}Fe incorporation was developed. In this approach, ^{52}Mn was included in the initial reagents for the MION core and utilized throughout the nano-crystal. This resulted in consistent ^{52}Mn incorporation efficiency and MR contrast properties, as well as a nanoparticle agent appropriate for the subsequent hybrid PET/MR imaging studies.

6.2. Hybrid PET/MRI

The ^{52}Mn -MIONs were characterized in both PET and MRI scanners with a phantom study. This demonstrated the multi-modal signal originating from the hybrid nanoparticles. Then the ^{52}Mn -MIONs were utilized in vivo for a hybrid PET/MRI study imaging xenograft tumor bearing mice. PET and MRI data was collected and analyzed showing the multimodal use of the radio-intrinsic hybrid PET/MRI nanoparticle.

Chapter 7

7. Further Work

The successful development of cRGD targeted ^{52}Mn -MIONs lends itself to a number of future uses. cRGD is a targeting peptide shown to bind with the $\alpha_v\beta_3$ integrin, which is associated with angiogenesis. The angiogenesis is necessary for tumor development and progression and this probe is a candidate for studying angiogenesis in other cancer models. U87MG tumors were utilized in this project, but other cell lines that do not themselves express $\alpha_v\beta_3$ integrin can be used. In these imaging studies, the endothelial cells growing blood vessels to support the tumors would be targeted. Additionally, orthotopic tumor models can be utilized to more realistically recreate the tumor micro-environment found in the clinic.^{77,78} The ^{52}Mn -MION-cRGDs can also be used in imaging trails to validate anti-vascular therapies for cancer.⁷⁹ Changes in the probe uptake could be related to tumor response to the anti-vascular drugs.

7.1. Future direction for ^{52}Mn

Ionic $^{52}\text{Mn}^{2+}$ has a number of possible uses for follow up studies. As a result of the 5.591 day half-life of ^{52}Mn , it can be used to study the metabolism and pharmacokinetics of manganese in intact organisms. Previous work has shown that $^{52}\text{Mn}^{2+}$ is taken up by bones, similar to ^{18}F , which indicates that it could be used in bone imaging application that last weeks, as opposed to ^{18}F which is only used for shorter studies.⁸⁰ Additionally, the high energy gamma emission of ^{52}Mn may provide cascade background in PET imaging applications. Further work could correct

for this by gathering data on events detected by the PET scanner at energies above the normal PET window and subtracting this background.

7.2. Future direction for [^{52}Mn]-MION

The [^{52}Mn]-MION imaging agent has considerable possibilities for future development. An imaging study using a hybrid PET/MRI scanner would allow for better co-registration of PET and MR data and a possible statistical analysis on a pixel by pixel basis of the correlation between MR contrast and PET signal. In this work, cRGD was utilized for targeting, but the surface coating is appropriate for modification with a wide variety of potential targeting molecules. J591, an anti-prostate specific membrane antigen (PSMA) antibody, could be conjugated to target and image PSMA expression in prostates and prostate cancers.⁸¹ Another option is the use of Herceptin, an anti-her2/neu monoclonal antibody, which has been used to target and image breast cancer cell lines.⁸² The MIONs and SPIONs developed in this project showed considerable uptake in the liver. This reduced their effectiveness as targeted imaging agents, as the probes were not available to bind with the targets expressed on tumor cells, if they were sequestered in the liver. While this project attempted to reduce this problem with different coating strategies, further work could explore the development of other organic ligands to reduce the liver uptake and increase the nanoparticles bio-availability. Specifically, a zwitterionic coating could be investigated to increase blood circulation.

As mentioned in Section 3.5, the size range of the nanoparticles synthesized in this method is not totally reproducible. This variability is not so great that it prohibits *in vivo* application of these nanoparticles, because the size variation (2-15 nm) falls within the range of nanoparticles that can circulate within intact vasculature. As shown in this work the [^{52}Mn]-MION can be imaged

with both PET and MRI. PET has excellent probe sensitivity and quantification, but has only moderate spatial resolution. The spatial resolution of MRI is stronger, but MR quantification of SPIONs and MIONs is difficult. A hybrid reconstruction could be developed from PET/MRI scans of the [^{52}Mn]-MION in the future, which utilized the spatial information from the MR contrast and the probe quantification from the PET signal to create a more detailed probe map than is available from each modality separately. Finally, the ^{52}Mn -MION platform can be utilized to evaluate MIONs and SPIONs in a research capacity. The initial pharmacokinetics, degradation, and final endpoint of the MION components can be characterized *in vivo* with the PET signal as part of the validation of different non-radioactive MIONs that are developed for clinical application.

Appendix

Research publications from this work

Sun M, Sundaresan G, Jose P, Yang L, **Hoffman D**, Corwin F, Lamichhane N, and Zweit J. “Intrinsically Radiolabeled Indium-111 Quantum Dots with Multidentate Zwitterionic Surface Coating for Single Photon Emission Computed Tomography (SPECT) and Fluorescence Imaging” *ACS Nano*, under review.

Hoffman D, Yang L, Sun M, Sundaresan G, McDonagh P, Corwin F, Wang L, Thadigiri C, and Zweit J. “Intrinsically radio-labeled [^{59}Fe]-SPIONs for multi-modal detection” *Am J Nucl Med Mol Imaging*, in preparation.

M Sun, **D Hoffman**, G Sundaresan, L Yang, N Lamichhane, J Zweit: “Synthesis and characterization of intrinsically radio-labeled quantum dots for bimodal detection” *Am J Nucl Med Mol Imaging* 2012; 2(2): 122-135.

Hoffman D, Sundaresan G, Sun M, Lamichhane N, Chiao D, and Zweit J. “Biodistribution studies of radio-quantum dots in tumor bearing mice” *Journal of Nuclear Medicine*. ⁵²: pp235, 2011.

Lamichhane N, Sundaresan G, Yang L, **Hoffman D**, Chiao D, Perez JM, and Zweit J. “In vivo evaluation of [^{141}Ce]-nanoparticles in nude mice” *Journal of Nuclear Medicine*. ⁵²: pp1582. 2011.

Conferences and Presentations

Hoffman D, Yang L, Sun M, McDonagh P, Corwin F, Sundaresan G, Wang L, Thadigiri C, Zweit J. “Superparamagnetic Nanoparticles for Hybrid PET/MR Imaging” Medical Physics Department BS session, Virginia Commonwealth University, Richmond, Virginia, October 2013.

Hoffman D, Yang L, Sun M, McDonagh P, Corwin F, Sundaresan G, Wang L, Thadigiri C, Zweit J. “Hybrid Superparamagnetic Nanoparticles for Bimodal Detection and Hybrid Imaging” Poster Presentation at World Molecular Imaging Congress, Savannah, Georgia, September 2013.

Hoffman D, Yang L, Sun M, McDonagh P, Corwin F, Sundaresan G, Wang L, Thadigiri C, Zweit J. “Hybrid Positron Emission Tomography/Magnetic Resonance Imaging Nanoparticle Probe Development” Poster Presentation at AACR-SNMMI Conference, San Diego, California, March 2013.

Hoffman D, Yang L, Sun M, Corwin F, Sundaresan G, Zweit J. “Hybrid PET/MRI Nanoparticle Probe Development” Oral Presentation at North American Imaging Users Meeting, Baltimore, Maryland, December 2012.

Hoffman D, Yang L, Sun M, McDonagh P, Corwin F, Sundaresan G, Zweit J. “Hybrid Superparamagnetic Iron Oxide Nanoparticle Development for Multi-modal Molecular Imaging” Medical Physics Department BS session, Virginia Commonwealth University, Richmond, Virginia, October 2012.

Hoffman D, Sundaresan G, Sun M, Lamichhane N, Chiao D, Zweit J. “The Effect of Surface Coating on the Biodistribution of Radio-Quantum Dots” Medical Physics Department BS session, Virginia Commonwealth University, Richmond, Virginia, December 2011.

Hoffman D, Sundaresan G, Sun M, Lamichhane N, Chiao D, Zweit J. “Biodistribution studies of radio-Quantum Dots in tumor bearing mice” Oral presentation at the Society of Nuclear Medicine and Molecular Imaging annual meeting, San Antonio, Texas, June 2011.

Hoffman D, Sundaresan G, Sun M, Lamichhane N, Chiao D, Zweit J. “Radio-Quantum Dots for Multi-Modal Molecular Imaging” Oral presentation at the American Association of Physicist in Medicine Mid-Atlantic Chapter Annual Conference, Charlottesville, Virginia, September 2010.

References

¹ Minghao Sun et al., “Synthesis and Characterization of Intrinsically Radiolabeled Quantum Dots for Bimodal Detection,” *American Journal of Nuclear Medicine and Molecular Imaging* 2, no. 2 (2012): 122–135.

² Ahmedin Jemal et al., “Global Cancer Statistics,” *CA: A Cancer Journal for Clinicians* 61, no. 2 (April 2011): 69–90, doi:10.3322/caac.20107.

- ³ Douglas Hanahan and Robert A. Weinberg, "Hallmarks of Cancer: The Next Generation," *Cell* 144, no. 5 (March 4, 2011): 646–674, doi:10.1016/j.cell.2011.02.013.
- ⁴ K. McLarty and R. M. Reilly, "Molecular Imaging as a Tool for Personalized and Targeted Anticancer Therapy," *Clinical Pharmacology & Therapeutics* 81, no. 3 (2007): 420–424, doi:10.1038/sj.clpt.6100096.
- ⁵ Markus Rudin and Ralph Weissleder, "Molecular Imaging in Drug Discovery and Development," *Nature Reviews Drug Discovery* 2, no. 2 (February 2003): 123–131, doi:10.1038/nrd1007.
- ⁶ Jinming Yu et al., "New Strategy for Monitoring Targeted Therapy: Molecular Imaging," *International Journal of Nanomedicine* (September 2013): 3703, doi:10.2147/IJN.S51264.
- ⁷ Sanjiv Sam Gambhir, "Molecular Imaging of Cancer with Positron Emission Tomography," *Nature Reviews Cancer* 2, no. 9 (September 2002): 683–693, doi:10.1038/nrc882.
- ⁸ M A Pysz, S S Gambhir, and J K Willmann, "Molecular Imaging: Current Status and Emerging Strategies," *Clinical Radiology* 65, no. 7 (July 2010): 500–516, doi:10.1016/j.crad.2010.03.011.
- ⁹ Karen A Kurdziel et al., "Human Dosimetry and Preliminary Tumor Distribution of 18F-Fluoropaclitaxel in Healthy Volunteers and Newly Diagnosed Breast Cancer Patients Using PET/CT," *Journal of Nuclear Medicine: Official Publication, Society of Nuclear Medicine* 52, no. 9 (September 2011): 1339–1345, doi:10.2967/jnumed.111.091587.
- ¹⁰ H.M. Hudson and R.S. Larkin, "Accelerated Image Reconstruction Using Ordered Subsets of Projection Data," *IEEE Transactions on Medical Imaging* 13, no. 4 (1994): 601–609, doi:10.1109/42.363108.
- ¹¹ Paul McQuade et al., "Positron-Emitting radionuclides Produced on Biomedical Cyclotrons," *Current Medicinal Chemistry* 12, no. 7 (April 1, 2005): 807–818, doi:10.2174/0929867053507397.
- ¹² Fujibayashi Y et al., "A New Zinc-62/copper-62 Generator as a Copper-62 Source for PET Radiopharmaceuticals," *Journal of Nuclear Medicine : Official Publication, Society of Nuclear Medicine* 30, no. 11 (November 1989): 1838–1842.
- ¹³ G. E. Meinken et al., "Production of High Specific Activity ^{68}Ge at Brookhaven National Laboratory," *Journal of Radioanalytical and Nuclear Chemistry* 263, no. 2 (January 1, 2005): 553–557, doi:10.1007/s10967-005-0091-4.
- ¹⁴ Y. Yano et al., "Evaluation and Application of Alumina-Based Rb-82 Generators Charged with High Levels of Sr-82/85," *J. Nucl. Med.; (United States)* 20:9 (September 1, 1979), <http://www.osti.gov/scitech/biblio/5711211>.
- ¹⁵ Michael J. Welch and Carol S. Redvanly, eds., "Handbook of Radiopharmaceuticals," in *Handbook of Radiopharmaceuticals* (John Wiley & Sons, Ltd, 2005), i–xiv, <http://onlinelibrary.wiley.com.proxy.library.vcu.edu/doi/10.1002/0470846380.fmatter/summary>.
- ¹⁶ Caterina F. Ramogida and Chris Orvig, "Tumour Targeting with Radiometals for Diagnosis and Therapy," *Chemical Communications* 49, no. 42 (April 30, 2013): 4720–4739, doi:10.1039/C3CC41554F.
- ¹⁷ Susanta Lahiri, Dalia Nayak, and Gunther Korschinek, "Separation of No-Carrier-Added 52Mn from Bulk Chromium: A Simulation Study for Accelerator Mass Spectrometry Measurement of 53Mn," *Analytical Chemistry* 78, no. 21 (November 1, 2006): 7517–7521, doi:10.1021/ac0607459.
- ¹⁸ J Zweit, S Downey, and H Sharma, "A Method for the Production of Iron-52 with a Very Low Iron-55 Contamination," *International Journal of Radiation Applications and Instrumentation. Part A, Applied Radiation and radionuclides* 39, no. 12 (1988): 1197–1201.
- ¹⁹ H. Sharma et al., "Production of Cobalt-55, a Short-Lived, Positron Emitting Radiolabel for Bleomycin," *International Journal of Radiation Applications and Instrumentation. Part A. Applied Radiation and radionuclides* 37, no. 2 (1986): 105–109, doi:10.1016/0883-2889(86)90055-9.
- ²⁰ M Sadeghi et al., "(86)Y Production via (86)Sr(p,n) for PET Imaging at a Cyclotron," *Applied Radiation and Nuclides: Including Data, Instrumentation and Methods for Use in Agriculture, Industry and Medicine* 67, no. 7–8 (August 2009): 1392–1396, doi:10.1016/j.apradiso.2009.02.038.
- ²¹ Jason P. Holland, Yiauchung Sheh, and Jason S. Lewis, "Standardized Methods for the Production of High Specific-Activity Zirconium-89," *Nuclear Medicine and Biology* 36, no. 7 (October 2009): 729–739, doi:10.1016/j.nucmedbio.2009.05.007.
- ²² "MRI From Picture to Proton: 2nd Ed.," *American Journal of Neuroradiology* 29, no. 6 (June 1, 2008): e50–e50, doi:10.3174/ajnr.A0980.
- ²³ PJ Beatty, "Reconstruction Methods for Fast Magnetic Resonance Imaging." (PhD thesis, Stanford University, 2006).

- ²⁴ Simon R. Cherry, "Multimodality Imaging: Beyond PET/CT and SPECT/CT," *Seminars in Nuclear Medicine* 39, no. 5 (September 2009): 348–353, doi:10.1053/j.semnuclmed.2009.03.001.
- ²⁵ Orazio Schillaci, "Hybrid SPECT/CT: A New Era for SPECT Imaging?," *European Journal of Nuclear Medicine and Molecular Imaging* 32, no. 5 (April 1, 2005): 521–524, doi:10.1007/s00259-005-1760-9.
- ²⁶ Angelique Ale et al., "Imaging Performance of a Hybrid X-Ray Computed Tomography-Fluorescence Molecular Tomography System Using Priors," *Medical Physics* 37, no. 5 (May 2010): 1976–1986.
- ²⁷ M. Niedre and V. Ntziachristos, "Elucidating Structure and Function <emphsis emphasistype='italic'>In Vivo</emphsis> With Hybrid Fluorescence and Magnetic Resonance Imaging," *Proceedings of the IEEE* 96, no. 3 (March 2008): 382–396, doi:10.1109/JPROC.2007.913498.
- ²⁸ J. Peter et al., "Development and Initial Results of a Dual-Modality SPECT/optical Small Animal Imager," in *2005 IEEE Nuclear Science Symposium Conference Record*, vol. 4, 2005, 4 pp., doi:10.1109/NSSMIC.2005.1596718.
- ²⁹ R. Fahrig et al., "Design, Performance, and Applications of a Hybrid X-Ray/MR System for Interventional Guidance," *Proceedings of the IEEE* 96, no. 3 (March 2008): 468–480, doi:10.1109/JPROC.2007.913506.
- ³⁰ Lihong V. Wang, "Prospects of Photoacoustic Tomography," *Medical Physics* 35, no. 12 (2008): 5758–5767, doi:10.1118/1.3013698.
- ³¹ David W Townsend et al., "PET/CT Today and Tomorrow," *Journal of Nuclear Medicine: Official Publication, Society of Nuclear Medicine* 45 Suppl 1 (January 2004): 4S–14S.
- ³² Osama Mawlawi and David W Townsend, "Multimodality Imaging: An Update on PET/CT Technology," *European Journal of Nuclear Medicine and Molecular Imaging* 36 Suppl 1 (March 2009): S15–29, doi:10.1007/s00259-008-1016-6.
- ³³ Paul Workman et al., "Minimally Invasive Pharmacokinetic and Pharmacodynamic Technologies in Hypothesis-Testing Clinical Trials of Innovative Therapies," *Journal of the National Cancer Institute* 98, no. 9 (May 3, 2006): 580–598, doi:10.1093/jnci/djj162.
- ³⁴ C S Brock et al., "Early Evaluation of Tumour Metabolic Response Using [18F]fluorodeoxyglucose and Positron Emission Tomography: A Pilot Study Following the Phase II Chemotherapy Schedule for Temozolomide in Recurrent High-Grade Gliomas," *British Journal of Cancer* 82, no. 3 (February 2000): 608–615, doi:10.1054/bjoc.1999.0971.
- ³⁵ Ciprian Catana et al., "Simultaneous Acquisition of Multislice PET and MR Images: Initial Results with a MR-Compatible PET Scanner," *Journal of Nuclear Medicine: Official Publication, Society of Nuclear Medicine* 47, no. 12 (December 2006): 1968–1976.
- ³⁶ Bernd J Pichler et al., "PET/MRI: Paving the Way for the next Generation of Clinical Multimodality Imaging Applications," *Journal of Nuclear Medicine: Official Publication, Society of Nuclear Medicine* 51, no. 3 (March 2010): 333–336, doi:10.2967/jnumed.109.061853.
- ³⁷ Habib Zaidi, Osama Mawlawi, and Colin G. Orton, "Simultaneous PET/MR Will Replace PET/CT as the Molecular Multimodality Imaging Platform of Choice," *Medical Physics* 34, no. 5 (2007): 1525, doi:10.1118/1.2732493.
- ³⁸ B E Hammer, N L Christensen, and B G Heil, "Use of a Magnetic Field to Increase the Spatial Resolution of Positron Emission Tomography," *Medical Physics* 21, no. 12 (December 1994): 1917–1920.
- ³⁹ Heinz-Peter W Schlemmer et al., "Simultaneous MR/PET Imaging of the Human Brain: Feasibility Study," *Radiology* 248, no. 3 (September 2008): 1028–1035, doi:10.1148/radiol.2483071927.
- ⁴⁰ Sophie Laurent et al., "Magnetic Iron Oxide Nanoparticles: Synthesis, Stabilization, Vectorization, Physicochemical Characterizations, and Biological Applications," *Chemical Reviews* 108, no. 6 (June 2008): 2064–2110, doi:10.1021/cr068445e.
- ⁴¹ Jae-Hyun Lee et al., "Artificially Engineered Magnetic Nanoparticles for Ultra-Sensitive Molecular Imaging," *Nature Medicine* 13, no. 1 (2006): 95–99, doi:10.1038/nm1467.
- ⁴² Nohyun Lee and Taeghwan Hyeon, "Designed Synthesis of Uniformly Sized Iron Oxide Nanoparticles for Efficient Magnetic Resonance Imaging Contrast Agents," *Chemical Society Reviews* 41, no. 7 (March 12, 2012): 2575–2589, doi:10.1039/C1CS15248C.
- ⁴³ Jason S Weinstein et al., "Superparamagnetic Iron Oxide Nanoparticles: Diagnostic Magnetic Resonance Imaging and Potential Therapeutic Applications in Neurooncology and Central Nervous System Inflammatory Pathologies, a Review," *Journal of Cerebral Blood Flow and Metabolism: Official Journal of the International Society of Cerebral Blood Flow and Metabolism* 30, no. 1 (January 2010): 15–35, doi:10.1038/jcbfm.2009.192.

- ⁴⁴ Bozena Novotna et al., “Oxidative Damage to Biological Macromolecules in Human Bone Marrow Mesenchymal Stromal Cells Labeled with Various Types of Iron Oxide Nanoparticles,” *Toxicology Letters* 210, no. 1 (April 5, 2012): 53–63, doi:10.1016/j.toxlet.2012.01.008.
- ⁴⁵ Sheng Tong et al., “Coating Optimization of Superparamagnetic Iron Oxide Nanoparticles for High T2 Relaxivity,” *Nano Letters* 10, no. 11 (November 10, 2010): 4607–4613, doi:10.1021/nl102623x.
- ⁴⁶ Jeff W M Bulte and Dara L Kraitchman, “Iron Oxide MR Contrast Agents for Molecular and Cellular Imaging,” *NMR in Biomedicine* 17, no. 7 (November 2004): 484–499, doi:10.1002/nbm.924.
- ⁴⁷ Xavier Montet et al., “Nanoparticle Imaging of Integrins on Tumor Cells,” *Neoplasia (New York, N.Y.)* 8, no. 3 (March 2006): 214–222.
- ⁴⁸ Barbara Freund et al., “A Simple and Widely Applicable Method to ⁵⁹Fe-Radiolabel Monodisperse Superparamagnetic Iron Oxide Nanoparticles for In Vivo Quantification Studies,” *ACS Nano* 6, no. 8 (August 28, 2012): 7318–7325, doi:10.1021/nn3024267.
- ⁴⁹ Ha-Young Lee et al., “PET/MRI Dual-Modality Tumor Imaging Using Arginine-Glycine-Aspartic (RGD)–Conjugated Radiolabeled Iron Oxide Nanoparticles,” *Journal of Nuclear Medicine* 49, no. 8 (August 1, 2008): 1371–1379, doi:10.2967/jnumed.108.051243.
- ⁵⁰ Xiaoqiang Yang et al., “cRGD-Functionalized, DOX-Conjugated, and ⁶⁴Cu-Labeled Superparamagnetic Iron Oxide Nanoparticles for Targeted Anticancer Drug Delivery and PET/MR Imaging,” *Biomaterials* 32, no. 17 (June 2011): 4151–4160, doi:10.1016/j.biomaterials.2011.02.006.
- ⁵¹ Sivasai Balivada et al., “A/C Magnetic Hyperthermia of Melanoma Mediated by iron(0)/iron Oxide Core/shell Magnetic Nanoparticles: A Mouse Study,” *BMC Cancer* 10, no. 1 (2010): 119, doi:10.1186/1471-2407-10-119.
- ⁵² Chao Huang et al., “Polymeric Nanoparticles with Encapsulated Superparamagnetic Iron Oxide and Conjugated Cisplatin for Potential Bladder Cancer Therapy,” *Biomacromolecules* 13, no. 8 (August 13, 2012): 2513–2520, doi:10.1021/bm300739w.
- ⁵³ Monty Liong et al., “Multifunctional Inorganic Nanoparticles for Imaging, Targeting, and Drug Delivery,” *ACS Nano* 2, no. 5 (May 1, 2008): 889–896, doi:10.1021/nm800072t.
- ⁵⁴ Poornima Budime Santhosh and Nataša Poklar Ulrih, “Multifunctional Superparamagnetic Iron Oxide Nanoparticles: Promising Tools in Cancer Theranostics,” *Cancer Letters* 336, no. 1 (August 9, 2013): 8–17, doi:10.1016/j.canlet.2013.04.032.
- ⁵⁵ J Lodhia et al., “Development and Use of Iron Oxide Nanoparticles (Part 1): Synthesis of Iron Oxide Nanoparticles for MRI,” *Biomedical Imaging and Intervention Journal* 6, no. 2 (June 2010): e12, doi:10.2349/biij.6.2.e12.
- ⁵⁶ Mona Gupta Ajay Kumar Gupta, “Synthesis and Surface Engineering of Iron Oxide Nanoparticles for Biomedical Applications,” *Biomaterials* 26, no. 18 (2005): 3995–4021, doi:10.1016/j.biomaterials.2004.10.012.
- ⁵⁷ Andreas F Thünemann et al., “Maghemite Nanoparticles Protectively Coated with Poly(ethylene Imine) and Poly(ethylene Oxide)-Block-Poly(glutamic Acid),” *Langmuir: The ACS Journal of Surfaces and Colloids* 22, no. 5 (February 28, 2006): 2351–2357, doi:10.1021/la052990d.
- ⁵⁸ Pedro Tartaj and Carlos J. Serna, “Microemulsion-Assisted Synthesis of Tunable Superparamagnetic Composites,” *Chemistry of Materials* 14, no. 10 (October 1, 2002): 4396–4402, doi:10.1021/cm021214d.
- ⁵⁹ Shouheng Sun and Hao Zeng, “Size-Controlled Synthesis of Magnetite Nanoparticles,” *Journal of the American Chemical Society* 124, no. 28 (July 1, 2002): 8204–8205, doi:10.1021/ja026501x.
- ⁶⁰ T Hyeon et al., “Synthesis of Highly Crystalline and Monodisperse Maghemite Nanocrystallites without a Size-Selection Process,” *Journal of the American Chemical Society* 123, no. 51 (December 26, 2001): 12798–12801.
- ⁶¹ K Suzuki, “[Production of ⁵²Fe by the ⁵⁵Mn(p,n)⁵²Fe reaction and milking of ⁵²mMn from ⁵²Fe],” *Radionuclides* 34, no. 10 (October 1985): 537–542.
- ⁶² Hong Yang et al., “Water-Soluble Superparamagnetic Manganese Ferrite Nanoparticles for Magnetic Resonance Imaging,” *Biomaterials* 31, no. 13 (May 2010): 3667–3673, doi:10.1016/j.biomaterials.2010.01.055.
- ⁶³ H. H. Andersen et al., “Stopping Power of the Elements Z=20 Through Z=30 for 5-12-MeV Protons and Deuterons,” *Physical Review* 175, no. 2 (November 10, 1968): 389–395, doi:10.1103/PhysRev.175.389.
- ⁶⁴ H. I. West, R. G. Lanier, and M. G. Mustafa, “⁵²Cr(p,n)⁵²Mn^{g},m and ⁵²Cr(d,2n)⁵²Mn^{g},m Excitation Functions,” *Physical Review C* 35, no. 6 (June 1, 1987): 2067–2076, doi:10.1103/PhysRevC.35.2067.
- ⁶⁵ Lahiri, Nayak, and Korschinek, “Separation of No-Carrier-Added ⁵²Mn from Bulk Chromium.” West, Lanier, and Mustafa, “⁵²Cr(p,n)⁵²Mn^{g},m and ⁵²Cr(d,2n)⁵²Mn^{g},m Excitation Functions.”

-
- ⁶⁶ Yang et al., “cRGD-Functionalized, DOX-Conjugated, and ⁶⁴Cu-Labeled Superparamagnetic Iron Oxide Nanoparticles for Targeted Anticancer Drug Delivery and PET/MR Imaging.”
- ⁶⁷ Goldie Kaul and Mansoor Amiji, “Biodistribution and Targeting Potential of Poly(ethylene Glycol)-Modified Gelatin Nanoparticles in Subcutaneous Murine Tumor Model,” *Journal of Drug Targeting* 12, no. 9–10 (December 2004): 585–591, doi:10.1080/10611860400013451.
- ⁶⁸ S. Pieper et al., “The NA-MIC Kit: ITK, VTK, Pipelines, Grids and 3D Slicer as an Open Platform for the Medical Image Computing Community,” in *3rd IEEE International Symposium on Biomedical Imaging: Nano to Macro, 2006*, 2006, 698–701, doi:10.1109/ISBI.2006.1625012.
- ⁶⁹ Andreas Markus Loening and Sanjiv Sam Gambhir, “AMIDE: A Free Software Tool for Multimodality Medical Image Analysis,” *Molecular Imaging* 2, no. 3 (July 2003): 131–137.
- ⁷⁰ Eric P. Visser et al., “Spatial Resolution and Sensitivity of the Inveon Small-Animal PET Scanner,” *Journal of Nuclear Medicine* 50, no. 1 (January 1, 2009): 139–147, doi:10.2967/jnumed.108.055152.
- ⁷¹ Jonathan A. Disselhorst et al., “Image-Quality Assessment for Several Positron Emitters Using the NEMA NU 4-2008 Standards in the Siemens Inveon Small-Animal PET Scanner,” *Journal of Nuclear Medicine* 51, no. 4 (April 1, 2010): 610–617, doi:10.2967/jnumed.109.068858.
- ⁷² Geoffrey J. Topping et al., “Manganese-52 Positron Emission Tomography Tracer Characterization and Initial Results in Phantoms and in Vivo,” *Medical Physics* 40, no. 4 (2013): 042502, doi:10.1118/1.4793756.
- ⁷³ L Bello et al., “Alpha(v)beta3 and alpha(v)beta5 Integrin Expression in Glioma Periphery,” *Neurosurgery* 49, no. 2 (August 2001): 380–389; discussion 390.
- ⁷⁴ C L Gladson and D A Cheresch, “Glioblastoma Expression of Vitronectin and the Alpha v Beta 3 Integrin. Adhesion Mechanism for Transformed Glial Cells,” *The Journal of Clinical Investigation* 88, no. 6 (December 1991): 1924–1932, doi:10.1172/JCI115516.
- ⁷⁵ Andrew R. Hsu et al., “In Vivo Near-Infrared Fluorescence Imaging of Integrin $\alpha\beta3$ in an Orthotopic Glioblastoma Model,” *Molecular Imaging and Biology* 8, no. 6 (November 1, 2006): 315–323, doi:10.1007/s11307-006-0059-y.
- ⁷⁶ Lee et al., “PET/MRI Dual-Modality Tumor Imaging Using Arginine-Glycine-Aspartic (RGD)-Conjugated Radiolabeled Iron Oxide Nanoparticles.”
- ⁷⁷ Giulio Francia et al., “Mouse Models of Advanced Spontaneous Metastasis for Experimental Therapeutics,” *Nature Reviews Cancer* 11, no. 2 (February 2011): 135–141, doi:10.1038/nrc3001.
- ⁷⁸ Carla Manzotti, Riccardo A. Audisio, and Graziella Pratesi, “Importance of Orthotopic Implantation for Human Tumors as Model Systems: Relevance to Metastasis and Invasion,” *Clinical & Experimental Metastasis* 11, no. 1 (January 1, 1993): 5–14, doi:10.1007/BF00880061.
- ⁷⁹ Monica Loi et al., “The Use of the Orthotopic Model to Validate Antivascular Therapies for Cancer,” *The International Journal of Developmental Biology* 55, no. 4–5 (2011): 547–555, doi:10.1387/ijdb.103230ml.
- ⁸⁰ Topping et al., “Manganese-52 Positron Emission Tomography Tracer Characterization and Initial Results in Phantoms and in Vivo.”
- ⁸¹ Anil K Patri et al., “Synthesis and in Vitro Testing of J591 Antibody-Dendrimer Conjugates for Targeted Prostate Cancer Therapy,” *Bioconjugate Chemistry* 15, no. 6 (December 2004): 1174–1181, doi:10.1021/bc0499127.
- ⁸² Fereshteh Shamsipour et al., “Conjugation of Monoclonal Antibodies to Super Paramagnetic Iron Oxide Nanoparticles for Detection of her2/neu Antigen on Breast Cancer Cell Lines,” *Avicenna Journal of Medical Biotechnology* 1, no. 1 (April 2009): 27–31.